Solution-based analysis of individual perovskite quantum dots and coupled quantum dot dimers using nanoplasmonic tweezers

by

Hao Zhang

B.Sc., Tianjin University, 2020

A Thesis Submitted in Partial Fulfillment of the

Requirements for the Degree of

MASTER OF APPLIED SCIENCE

in the Department of Electrical and Computer Engineering

Solution-based analysis of individual perovskite quantum dots and coupled quantum dot dimers using nanoplasmonic tweezers

by

Hao Zhang

B.Sc., Tianjin University, 2020

Supervisory Committee

Dr. Reuven Gordon, Supervisor
(Department of Electrical and Computer Engineering)

Dr. Nikitas J. Dimopoulos, Departmental Member
(Department of Electrical and Computer Engineering)

ABSTRACT

Cesium lead halide perovskite quantum dots (PQDs) provide an extraordinary solution-based method to fabricate high-performance solar cells, luminescent light-emitting devices, highly coherent single-photon quantum sources, and studying quantum mechanisms for quantum computing technologies. In these applications, characterizing heterogeneity and observing coupling between dots is critical. In this thesis, we use double-nanohole (DNH) optical tweezers to realize single trapping for PQDs in solution. We can estimate the size of an individual dot by studying thermal fluctuations and correlate it to emission energy shifts from quantum confinement.

Based on single trapping experiment, we also use the same setup to capture a second dot by using the DNH tweezer and observe a systematic red-shift of 1.1 $\pm$ 0.6 meV in the emission wavelength upon multiple repeated measurements. Theoretical analysis shows that the experiment results are consistent with Förster resonant energy transfer (FRET), which has been proposed to obtain entanglement between colloidal quantum dots for quantum information applications. The value of the FRET is quite large when compared with the confined quantum dots and it is exciting for FRET to generate entanglement for quantum information processing applications (e.g. quantum logic gates).

In the thesis, we have proved that our method allows for in-situ sizing of individual PQDs for the first time, which is relevant for improving the growth process and does not require expensive techniques. It also enables future work to search and select two dots that are nominally identical. Optical trapping with DNHs fabricated using colloidal lithography can be used to control PQD growth in-situ and enables further studies of the coupling of quantum dots at a small distance with quantum information applications.

Contents

List of Tables

List of Figures

Glossary

Common Abbreviations

Abbreviation	Meaning
APD	**A**valanche **P**hoto**d**etector
BE	**B**eam **E**xpander
CCD	**C**harge-**c**oupled **D**evice
CW	**C**ontinuous **W**ave
DAQ	**D**ata **Ac**q**u**isition system
DNH	**D**ouble-**n**ano**h**ole
FDTD	**F**inite **D**ifference **T**ime **D**omain
FM	**F**lip **M**irror
HWP	**H**alf-**w**ave **P**late
LP	**L**inear **P**olarizer
LPF	**L**ong **P**ass **F**ilter
NA	**N**umerical **A**perture
$\boldsymbol{N_A}$	**A**vogadro Constant
NCs	**N**ano**c**rystal**s**
OBj	**Obj**ective lens
OD	**O**ptical **D**ensity filteR
PEC	**P**erfect **E**lectric **C**onductor
PL	**P**hoto**l**uminescence
PQD	**P**erovskite **Q**uantum **D**ot
QD	**Q**uantum **D**ot
RET	**R**esonant **E**nergy **T**ransfer
RMS	**R**oot **M**ean **S**quare
SD	**S**tandard **D**eviation
SEM	**S**canning **E**lectron **M**icroscope
SPF	**S**hort-**p**ass **f**ilter
SIBA	**S**elf-**i**nduced **B**ack-**a**ction
TEM	**T**ransmission **E**lectron **M**icroscopy

ACKNOWLEDGEMENTS

This journey would not have been possible without the support of many people. I would like to thank:

Prof. Reuven Gordon as my supervisor for supporting and offering me the opportunity to learn with the worldwide advanced nanoplasmonics research and for the invaluable guidance during my academic journey. You will always be my valuable model in academia.

Dr. Ghazal Hajisalem for helping me with my first setup. I still remember we worked together in front of the optical table until late night.

Mr. Michael Dobinson and Dr. Ryan Peck I would never forget the days we hang-out together. My first two friends in Canada!

Ms. Amrita Pati Our experience and trip of QC-CREATE and its workshop will be memorized!

Dr. Mirali Seyed Shariatdoust, Zohreh Sharifi, and Elham Babaei for their help in the lab, not only in research but also the daily life.

Behnam Khosravi, Samuel Mathew, and Brett Henderson I want to say thank you for the help in the lab.

I will never forget the valuable time we spent together in Nanoplasmonics Research Lab during the pandemic.

I want to thank **Prof. Rogério de Sousa**, **Prof. Makhsud Saidaminov**, **Prof. Stephen Hughes**, **Dr. Yuanjie Pang** and **Dr. Juanjuan Ren** for their kind help in my program. Many wishes to everyone who helped me at the beautiful UVIC campus.

I also want to thank the **NSERC CREATE in Quantum Computing program** and the fabrication facilities of **CAMTEC**. My best wishes to the University of Victoria and the University of British Columbia.

I would like to thank my parents and **my family** for their endless love, encouragement and supporting. I wish to thank my beloved **girlfriend**, for the amazing journey we travelled together. So lucky I can be loved by everyone.

DEDICATION

To my grandfather, Mi Zhang

Chapter 1

Introduction

Quantum dots (QDs), whose general sizes are around 2-20 nm, are known as the extraordinary material for the next generation of optoelectronic applications [1, 2, 3]. Quantum dots are semiconductor nanostructures that bind excitons in three spatial directions [1], sometimes called "artificial atom". To be more specific, QDs have different shapes: cuboid, cylindrical, pyramidal, conical, and lens shaped [4]. With the quantum-size effects, their optical properties are enhanced by adopting flexible bulk counterparts and versatile surface chemistry engineering. Cesium lead halide perovskite quantum dots (PQDs) has been the most promising solution-based optical materials because of their outstanding photonic performance [1, 5, 2, 6]. The $CsPbX_3$ nano cube and its synthesis, crystallography, and the direct bandgap have been reported more than 60 years ago [2, 3]. In recent years, with the great breakthroughs in studying PQDs, many applications have been developed (e.g., single-photon emitters [7], improved solar cells [1, 8, 9, 10]). PQDs of 4-15 nm with a cubic structure have been reported to exhibit not only compositional bandgap engineering but also an exciton Bohr diameter of up to 12 nm, which shows the size-tunability of the bandgap energies that cover all the visible spectral wavelength (410 – 700 nm) with narrow emission line-widths, short radiative lifetimes and high quantum yields [2].

With the fast development in quantum computing, many researchers are working on different potential areas for making a qubit for quantum systems (eg, superconducting circuit [11, 12, 13], ion trap [14, 15], quantum dot system (spin bit, charge bit) [16, 17, 18, 19, 20]). Tuning the coupling relationship between two quantum dots can realize different quantum logic gates [20] and let them to talk (shown in Figure 1.1). Here, in this thesis, a novel method for sizing a single PQD and studying the coupling between two individual dots are proposed and described in detail. We first develop

a simple method to estimate the size of the PQDs NCs in a heterogeneous solution. We then demonstrate that there is always a systemic red-shift between two coupled PQDs by using an optical tweezer. We consider several physical principles and we confirm the Förster resonate energy transfer is the dominant coupling mechanism between the two PQDs.

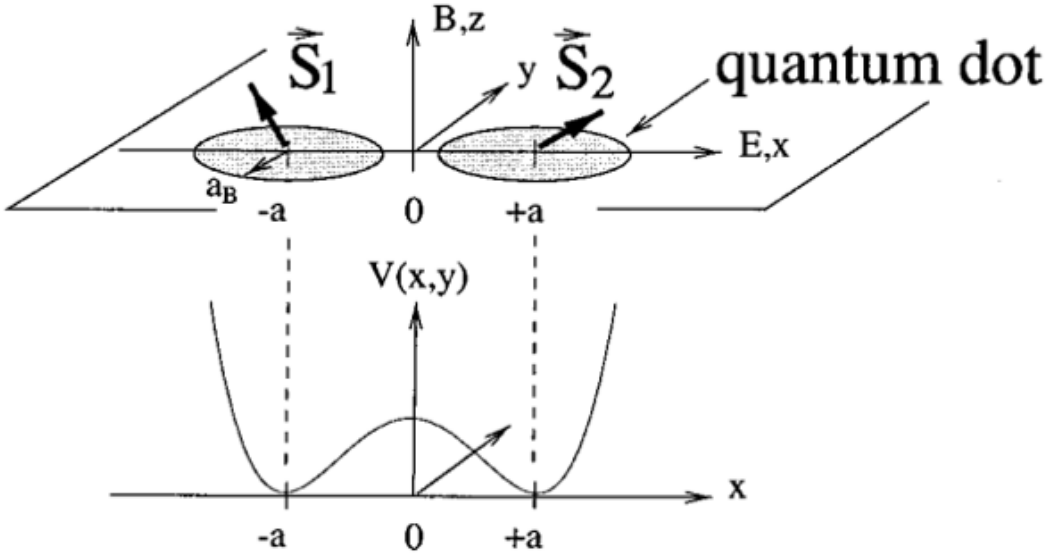

Figure 1.1: Two coupled quantum dots with one valence electron per dot. Each electron is confined to the XY plane. The spins of the electrons in dots 1 and 2 are denoted by S1 and S2. The magnetic field B is perpendicular to the plane, i.e., along the z axis, and the electric field E is in plane and along the x axis. The exchange coupling J between the spins is a function of B, E, and the inter-dot distance 2a [20]. Copyright © 1999 American Physical Society

1.1 Motivation for this thesis

1.1.1 Sizing single PQDs by using optical tweezer

Quantum confinement refers to the spatial confinement of electron-hole pairs (excitons) in one or more dimensions, where the electron energy levels are discrete. This is due to the limitation of the electron wave function on the physical size of particles. Based on the quantum confinement, the emission wavelengths from PQDs can be tuned by changing their size [21, 22, 23]. One problem raised from this property: it is hard to fabricate PQDs with controlled size and high ensemble uniformity.

It has been a major hindrance to photovoltaic and energy-harvesting applications. The structural heterogeneity of quantum dots greatly affects the overall properties of current semiconductor materials. Irregular size distribution in solution-based PQDs leads to the reduced output voltage and charge-carrier transport in solar cells [8]. Past works show that the output voltage has a strong relationship with the PQDs' bandgap [9, 24]. The technology that can precisely control quantum confinement with identical sizes of PQDs has been proposed and studied these years by many groups [21, 22, 23, 25, 26, 27]. For example, it would be great to have the scheme to select dots of a specific output voltage for high-performance solar and emitting applications [28, 8, 9, 24]. Or selecting two dots of the same wavelength so that they emit indistinguishable photons for quantum applications [29, 30].

Whereas, characterizing the physical size of PQDs from samples with external high-resolution equipment (e.g. transmission electron microscope) is the prerequisite to solving this problem. Existing measurement methods do spectroscopy on a surface [31, 32], which may be a factor that affects the sample due to the unclear stability of their chemical characteristics (heat, moisture, oxidation) [33]. The degradation of PQDs also limits the accessibility and feasibility of their applications. The key to solving the problem is to select and process or to do automated purification in their bulk solution. One approach would be practical is to use optical tweezers coupled to nanopores as has been done before [34, 35], or an optical tweezer on the end of a fiber that allows for translocation as has been demonstrated by Gordon's group [36, 37], which are compact to integrate and easy to operate. Producing and measuring the dots with uniform and controllable size has been a goal to improve the performance of device applications.

1.1.2 Coupling between PQDs dimer assembly by using optical tweezer

All-inorganic halide perovskite nanocrystals have efficient single-photon emission and long coherence time [38], which makes them a hot spot in the application of quantum information. Their strong coupling also allows non-classical emission, such as superfluorescence. In order to better understand this coupling, it is meaningful to study the coupling between two such emitters, which can be used to create entangled states.

Multiple physical mechanisms can be responsible for quantum dot coupling in solution. For quantum dots that are nominally symmetric and do not allow for electron

tunneling, Förster resonant energy transfer (FRET) has been considered to achieve coupling between dots, providing a possible avenue toward quantum information processing [39]. In the past, resonant energy transfer (RET) has been studied for PQDs of different sizes, where the longer wavelength emission peak is enhanced due to one-directional energy transfer [40]. The bi-directional coupling that arises from just two PQDs that are nominally the same size has not been investigated so far.

1.2 Organization of this Thesis

This thesis first presents the extraordinary electronic properties and promising application future of PQDs. Then the experimental methods adopted in this work are described and the results are presented and fully discussed.

Chapter 2 covers the basic background of PQDs and the theoretical background of traditional optical tweezers. Then we introduce nanoplasmonics tweezers with the double nanohole (DNH) apertures we used in this work. It also reviews the progress made using this technique in different studies.

Chapter 3 shows the details for running the experiments, which include the synthesis method for PQDs solutions, DNH optical tweezer fabrications, making solution-based PQDs samples with DNH tweezers, and experiment trapping setup.

Chapter 4 presents the results obtained for sizing a single PQD and measuring the coupling between two individual PQD when double trapping happened. It also discusses the results, along with theoretical calculations and numerical simulation.

Chapter 5 concludes this work with some discussion of future work.

1.3 Author's contribution

H. Zhang, P. Moazzezi, J. Ren, B. Henderson, C. Cordoba, V. Yeddu, A. Blackburn, M. Saidaminov, I. Paci, S. Huge & R. Gordon. ***Coupling Perovskite Quantum Dot Pairs in Solution using Nanoplasmonic Assembly***.

H.Z. fabricated the DNHs, performed the trapping experiments, analyzed the data and did the FDTD simulation. P.M. and V.Y. made the PQD

samples. M.I.S. advised on PQD synthesis and characterization. C.C. and A.B. were responsible for TEM imaging. B.H. and I.P. contributed to simulation of bandgap and emission energy as a function of single PQD size. J.R. and S.H. contributed to the theory and simulations of coupled quantum dots. R.G. advised on the experiments and analysis. All authors contributed to writing the manuscript.

This work will also be divided into two different parts and will be presented at the ***16th International Conference on Near-Field Optics, Nanophotonics and Related Techniques***.

H. Zhang, P. Moazzezi, J. Ren, B. Henderson, C. Cordoba, V. Yeddu, A. Blackburn, M. Saidaminov, I. Paci, S. Huge & R. Gordon. ***Sizing single quantum dots insolvent using nano-tweezers*** (Abstract, accepted)

Abstract: Cesium lead halide perovskite quantum dots (PQDs) promising solution-based optical materials because of their outstanding photonic performance. With the great breakthroughs in studying PQDs, many applications have been developed. Based on the quantum confinement, the emission wavelengths from PQDs vary with size. Producing and measuring the dots with uniform and controllable size has been a goal to improve the performance in device applications. Several groups have refined the fabrication processes to obtain good size uniformity; however, this usually involves transmission electron microscope analysis a posteriori, which is not convenient for characterization. Sizing PQDs insolvent would be a good approach when producing PQDs with uniform size, allowing for in-situ monitoring. In this paper, we present an approach to characterize in-situ the size of individual quantum dots and correlate this with their optical spectrum to see the impact of quantum confinement. We observe and analyze the heterogeneity of PQDs insolvent by using optical tweezers with DNH aperture. By using a simple calculation model of the Schrödinger equation, we calculate the bandgap as a function of particle size, which has a good agreement with our experiment result.

P. Moazzezi, **H. Zhang**, J. Ren, B. Henderson, C. Cordoba, V. Yeddu, A. Blackburn, M. Saidaminov, I. Paci, S. Huge & R. Gordon. ***Coupling between Perovskite Quantum Dots in a Plasmonic Optical Tweezers*** (Abstract, accepted)

Abstract: All inorganic halide Perovskite (CsPbBr3) nanocrystals (NCs) have efficient single photon emission and long coherence times which makes them of in-

terest for quantum information application. Their strong coupling also allows for non-classical emission, such as superfluorescence. To understand the coupling better, it is of interest to study the coupling between two such emitters, and this may be used to create entangled states. In this paper we measure the coupling between two Perovskite quantum dots (PQDs) by an optical tweezer trapping setup. We sequentially trap two dots in a single trap and measure the change in emission wavelength and intensity. We show the distribution of two-photon photoluminescence for single and double PQD trapping. Double PQD trapping is identified via jumps recorded on an avalanche photo diode. The emission intensity for double PQDs is more than double in comparison with single PQD trapping, and also there is systematic red-shift in the emission. The direct electronic coupling does not explain the observed shift, and so other mechanisms are required to explain these results.

Chapter 2

Background

This chapter will introduce the background of the PQDs and their extraordinary electronic properties in section 2.1.

Then we will review the overarching theory of the optical tweezers and nanoplasmonics tweezers in section 2.2.

Optical trapping and nanoplasmonic enhanced methods applied for quantum dots will be reviewed in section 2.3.

In section 2.4, the advanced method for sizing single nanoparticle with optical tweezer will be reviewed.

In section 2.5, we will review three potential physical coupling mechanisms between two quantum dots.

FDTD simulation method will be introduced in section 2.6.

These sections are the basis and explain the motivation for this thesis work in detail, which aims to use optical tweezers for studying PQDs and their coupling in solvent.

2.1 Perovskite Quantum Dots

Perovskite is a kind of mineral that was first discovered in the Ural Mountains by a German scientist called Gustav Rose. Later, Perovski first characterized the structure of this mineral. Since then, all compounds with ABX3 structure have been called perovskite [42]. Perovskite thin films usually contain a large density of charge traps at the grain boundaries. Since the single crystals have no grain boundaries, the perovskite single crystal-based devices will have better optoelectronic performances

[43]. Thus, perovskite has been studied in many areas, especially in fabricating novel quantum dots, as is shown in Figure 2.1.

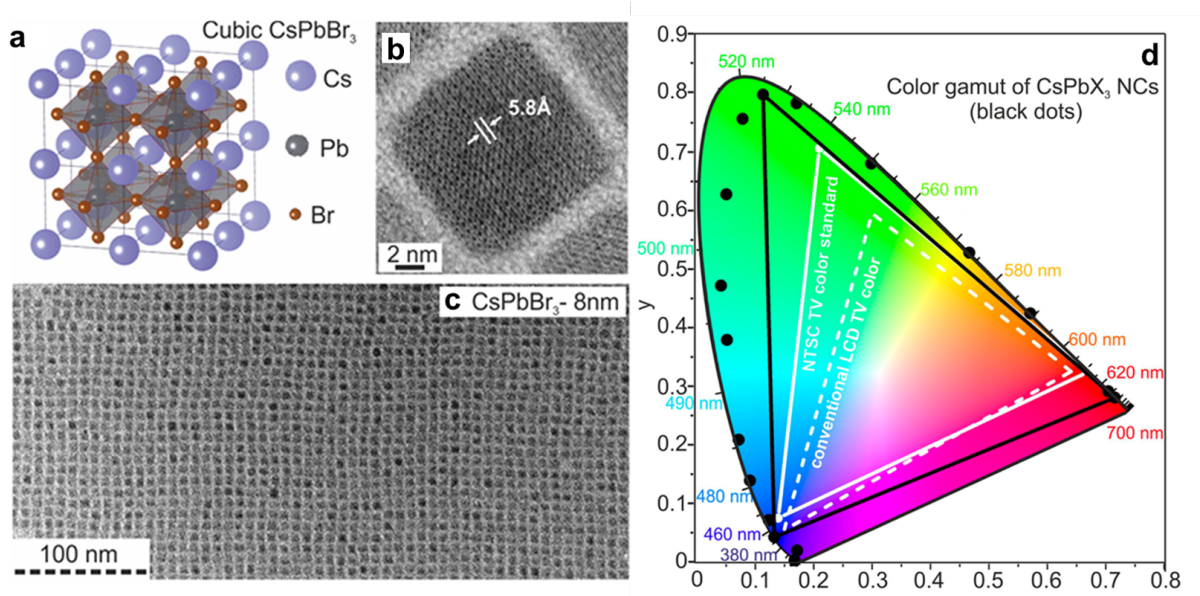

Figure 2.1: (a) Schematic of the cubic perovskite $CsPbBr_3$ lattice. (b-c) Typical transmission electron microscopy (TEM) images of $CsPbBr_3$ NCs. (d) Emission from CsPbX3 NCs (black data points) plotted on CEI chromaticity coordinates and compared to most common color standards. Adapted from Ref [2]. Reprinted with Copyright © 2015 American Chemical Society.

All-inorganic cesium lead halide perovskite quantum dots ($CsPbX_3$, X = Cl, Br, I) have become the hot-spot among all types of material candidates for the next photonic devices, such as the application of solar cells, light-emitting diodes, lasers, and displays. The optical properties of the popular different types of PQDs are summarized in Table 2.1. With the broad absorption spectrum and high photoluminescence (PL), up-to-90% quantum yield, and the narrow emission bandwidth [44, 45, 5, 2, 6]. Figure 2.1a-c shows its cube structure and TEM images. Emission from $CsPbX_3$ nanocubes can be comparable with the most common color standard, as is shown in the Figure 2.1d.

As is shown in Figure 2.2c, their optical absorption and emission wavelength can be fully tuned continually, which overlap all the visible range, by adjusting their composition.

Table 2.1: Different Types of PQDs [1]

PQD type	Lattice structure	PL peak [nm]	PLQY	Refs.
$CsPbX_3$	Cubic	410-700	50-90	[2]
$CsPbX_3$	Cubic	440-682	50-95	[46, 47, 48]
$CsPbBr_3$	Cubic	470-690	-	[49]
$CsSnX_3$	Cubic	470-930	<1	[50]
Cs_2SnI_6	Cubic	620	<1	[51]
$CsSn/PbX_3$	Cubic	496-520	37-71	[52]
$CsPb/MnX_3$	Orthorhombic	Dual emission 402/586	0-54	[53, 54]
$CsPb/MX_3$	Cubic	452-512	>50	[55]
$CsPb/BiX_3$	Cubic	512-517	8-55	[56]
$Au - CsPbX_3$	Cubic	472	60	[57]

2.1.1 Quantum Confinement

When the $CsPbX_3$ PQDs' size is larger than the de Broglie wavelength of the electron wave function, there is no quantum confinement effect [58, 2]. That means the band gap keeps the original energy level due to the continuous energy state. However, if the size is nearly equal to or smaller than the de Broglie wavelength of the electron wave function, the energy spectrum will become discrete. The band gap will have a dependency on the physical size of the nanoparticle. By decreasing the particle's size, electron-hole pares will get closer and the activation energy will increase, which will lead to the blue shift of the light emission. The quantum dots (including cube and sphere shapes) are limited to three-dimension.

To be more specific, the confinement can be divided into three regions [58, 59, 2]. The strong confinement region is defined as the radius of the quantum dots being less than the Bohr radius of the electron and hole. When the dot's size is greater than the radius, the weak confinement region is defined. Between the strong confinement and the weak confinement, there is an intermediate confinement regime, which stands for the size of the dot is larger than one of the charge carrier's size but smaller than the other's (usually the electron). If the sizes of the quantum dots are uniform, there will be only one emission peak. If the solution is the heterogeneous, multiple emission peaks might be observed as a continuous spectrum.

By using the effective mass theory [60, 2], the effective Bohr diameter of a Wannier-Mott exciton can be expressed by [2]:

$$\alpha_0 = \frac{2\hbar^2\epsilon^\infty}{m^* e^2} \tag{2.1}$$

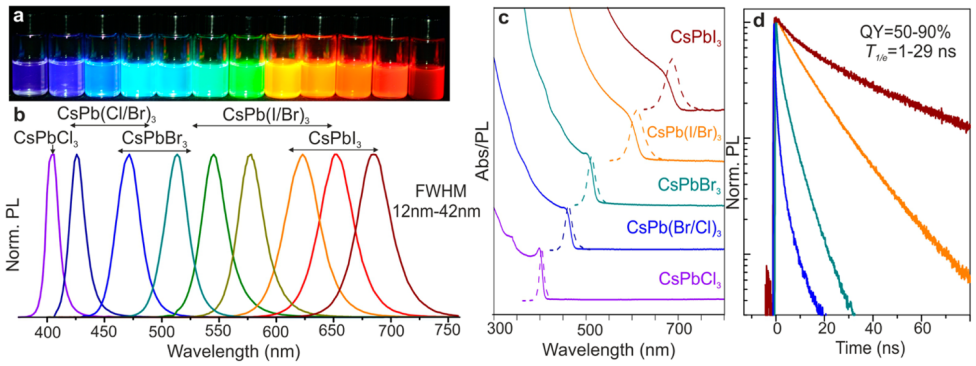

Figure 2.2: Colloidal perovskite $CsPbX_3$ NCs (X = Cl, Br, I) exhibit size− and composition−tunable bandgap energies covering the entire visible spectral region with narrow and bright emission: (a) colloidal solutions in toluene under UV lamp ($\lambda = 365\ nm$); (b) representative PL spectra ($\lambda_{exc} = 400\ nm$ for all but 350 nm for $CsPbCl_3$ samples); (c) typical optical absorption and PL spectra; (d) time−resolved PL decays for all samples except $CsPbCl_3$. Adapted from Ref [2]. Reprinted with Copyright © 2015 American Chemical Society.

where ϵ_∞ is the effective dielectric constant, and m^* is the reduced carrier mass. The binding energy between electrons and holes can be expressed as:

$$E_b = \frac{2\hbar^2}{m^* e^2} \tag{2.2}$$

where $\hbar$ is the Planck constant. Thus, the size dependence of the quantum confinement ($CsPbBr_3$) can be calculated by [2]:

$$\Delta E = \frac{\hbar^2 \pi^2}{2m^* r^2} \tag{2.3}$$

Table 2.2 summarizes the general properties of three different $CsPbX_3$ quantum dots with cubic shape [2].

Table 2.2: General Properties of $CsPbX_3$ PQDs [2]

	$E_g\ (eV)$	m_h^*	m_e^*	ϵ^∞	$E_b\ (meV)$	$a_0\ (nm)$
$CsPbCl_3$	2.82	0.17	0.20	4.07	75	5
$CsPbBr_3$	2.00	0.14	0.15	4.96	40	7
$CsPbI_3$	1.44	0.13	0.11	6.32	20	12

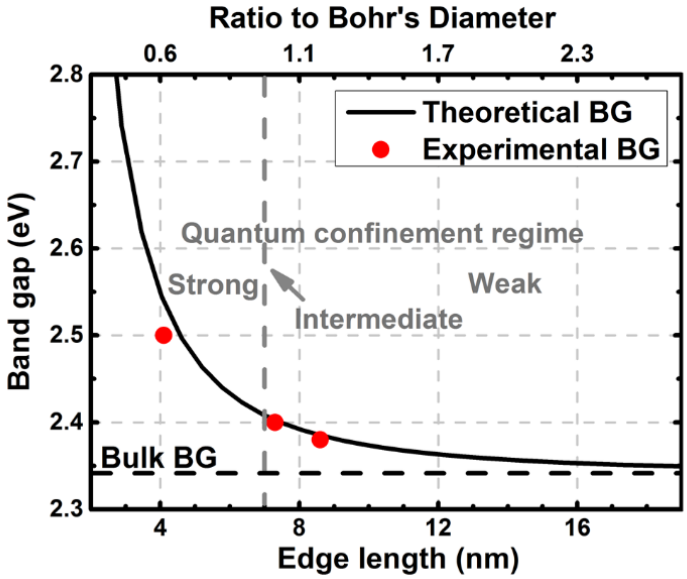

Figure 2.3: The size dependence of the bandgap energy with quantum confinement regimes noted in relation to the Bohr diameter (d_b =7 nm). Adapted from Ref [59]. Reprinted with Copyright © 2017 American Chemical Society.

2.2 Optical Trapping Fundamentals

2.2.1 Rayleigh Scattering and Optical Tweezer

Rayleigh scattering, which was named by John Strutt (3^{rd} Baron Rayleigh), is a general phenomenon that happens in our daily life. For example, in the atmosphere, Rayleigh's scattering of sunlight leads to diffuse sky radiation. That's why the sky is always blue. Rayleigh scattering occurs when incident light passes through tiny particles (such as the dust, which consists of small atoms or molecules) with a radius much smaller than the wavelength of light (electromagnetic radiation). Broadly speaking, Rayleigh scattering will occur when the incident light travels through transparent solids, liquids, and especially gas. With the Rayleigh scattering theory, the optical forces acting on small dielectric particles will be more effective. Optical tweezers, which can manipulate small particles, have been studied and developed for many applications (biology [61], medical [62], nano-engineering [35], chemistry [63] and quantum optics [64, 65]).

In 2018, Arthur Ashkin won the Nobel Prize for the first optical tweezer in the world. Since the first optical tweezer was designed in the 1970's [66, 67], optical trapping has become more widely adopted by many researchers. Optical force, which is generated by the incident laser beam to trap the objects, is critical for the optical tweezer. Intensity gradients in the converging beam capture the small particles and move them toward the focal point. An object can be trapped near the focal point in the XYZ dimensions since the gradient force is the dominant force. Focused incident of electromagnetic radiation with a Gaussian profile can generate two types of optical forces. As is shown in Figure 2.4, two different optical forces are playing an important role in the tweezer setup, which allows a small particle to get balanced and trapped. The scattering force is generated by the momentum transfer of photons through the small particle and the gradient force is resulting from the intensity gradient. Figure 2.4 demonstrates the radiation pressure acting on a small sphere particle in an incident beam, which results from the scattering and gradient forces on the sphere. Here, the diameter of the particle is bigger than the incident wavelength, and its refractive index is much bigger than the surrounding medium. If assuming there is a photon hit on the particle, it will carry a linear momentum of:

$$P = \frac{h\nu}{c} \tag{2.4}$$

where h is the Planck constant and ν is the frequency. c stands for the speed of light.

Omitting the surface reflections, we can assume all the light rays are refracted by the particle. If we assume two paths a and b upon scattering resulting force F_a and F_b on the sphere which ensures the conservation of momentum (as shown in Fig. 2.4). Notice that the particle is not at the focal point, which means ray a has a higher intensity than ray b, and the magnitude of force F_a is greater than F_b:$||F_a|| > ||F_b||$. After analyzing all the symmetrical pairs of rays exerting the particle, the system can be treated with two components: the scattering force (F_{scat}) and the gradient force (F_{grad}). The direction of F_{scat} keeps the same as the incident beam, while F_{grad} points transversely to the highest intensity area of the incident beam. As shown in Figure 2.4, the optical tweezer can be an oscillation system, which consists of a ball and a spring. Whether the gradient force pulls or pushes the sphere depends on the position relative to the focal point. When the particle is on the right top or bottom of the focal point, the gradient force on the x-axis and y-axis becomes zero: $F_{gradx} = F_{grady} = 0$. The force only acts on the particle along the z-axis. The backward axial gradient force F_{gradz} becomes dominant and counteracts F_{scat}. Usually, the stable trapping system consists of a strongly focusing laser beam with a high numerical aperture microscope objective.

Here we can quantitatively calculate the force acting on the small particle (approximate with a sphere) in the ray optics regime by using Fresnel reflection and transmission coefficients [68]

$$F_{scat} = \frac{nP}{c}\left\{1 + Rcos(2\theta) - \frac{T^2\left[cos(2\theta - 2r) + Rcos(2\theta)\right]}{1 + R^2 + 2Rcos(2r)}\right\} \tag{2.5}$$

$$F_{scat} = \frac{nP}{c}\left\{Rcos(2\theta) - \frac{T^2\left[cos(2\theta - 2r) + Rsin(2\theta)\right]}{1 + R^2 + 2Rcos(2r)}\right\} \tag{2.6}$$

where n is the refractive index of the medium, P is the laser beam's power, θ is the incident angle and r is the reflection angle. R and T stands for the Fresnel reflection and transmission coefficients at angle θ.

Now, we consider a small sphere and a system consist a collimated and monochromatic beam, which has been linearly polarized. If the sphere is small enough, the electric field around the sphere, as in the case of a Rayleigh scattering, is approximately uniform across its volume. That will make the sphere oscillate synchronously in the same direction as the incident field. This "dipole" radiates the electromagnetic energy and leads to scattering.

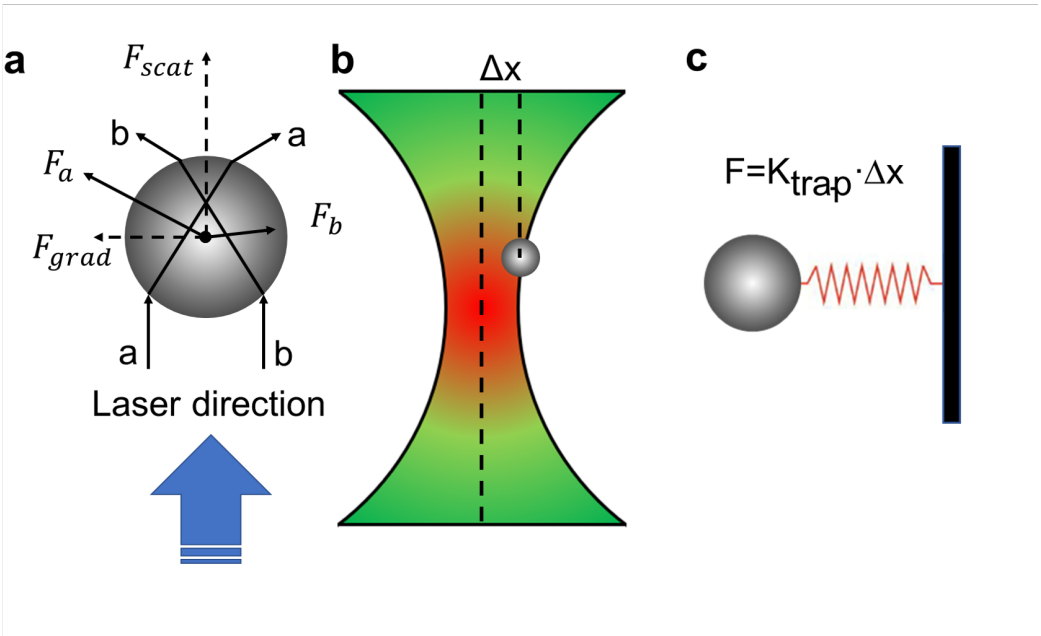

Figure 2.4: (a). Scattering and gradient force working on a small dielectric sphere, which is off−axis of a Gaussian beam. The gray ball is a small particle in the optical trapping system. The diameter of the sphere is bigger than the incident wavelength. (b). The black line on the left− and right−hand sides stand for the shape of the laser beam. Δx is the offset of the particle from the beam's center alone in the horizontal direction. The refraction of the beam light ray leads to the changes in the photon momentum and introduces the forces F_a and F_b. After the force cancellation, we can use two equivalent forces, F_{scat} and F_{grad} with a different direction, to illustrate this situation. (c). The simple equivalent oscillation resonator model using Hooke's law is shown on the right side.

$$\overrightarrow{p} = \alpha \overrightarrow{E} \tag{2.7}$$

where $\overrightarrow{p}$ is the equivalent dipole moment, $\overrightarrow{E}$ is the electric field and α is the polarizability of the particle:

$$\alpha = 4\pi r^3 (n_0)^2 \frac{(n_1/n_0)^2 - 1}{(n_1/n_0)^2 + 2} \tag{2.8}$$

n_0 is the refractive index of the medium around the particle. n_1 is the refractive index of the particle.

Since the intensity of the beam can be expressed by:

$$I = \frac{n_0 c}{2} |E|^2 \tag{2.9}$$

With equation 2.7 to 2.9, the scattering optical power can be calculated by the radiation of the dipole:

$$P_{scat} = \frac{16\pi^4 c}{3\lambda^4} |\overrightarrow{p}|^2 \tag{2.10}$$

where λ is the incident wavelength of the beam.

The flux pattern of electromagnetic radiation changes due to this scattered term, which introduces the scattering force [69, 70]:

$$F_{scat} = \frac{n_0}{c} P_{scat} \tag{2.11}$$

And from equation 2.10 to 2.11, we can find the scattering force within this tweezer system:

$$F_{scat} = \frac{128\pi^5 r^6 n_0}{3c\lambda^4} \left[\frac{(n_1/n_0)^2 - 1}{(n_1/n_0)^2 + 2} \right]^2 I_0 \tag{2.12}$$

where I_0 is the amplitude of the incident beam's intensity.

From equation 2.12, the relationship between F_{scat} and r and λ can be easily found: F_scat is proportional to $(r/\lambda)^4$. Also, F_{scat} has a linear relationship with the beam's intensity. As the particle's size becomes smaller than the wavelength, the scattering force sharply decreases.

Then the gradient force, which is the second optical force in this system, can be calculated by:

$$F = (p \cdot \nabla)E + \frac{dp}{c \cdot dt} \times B \tag{2.13}$$

With equation 2.7, we can get:

$$F = \alpha(E \cdot \nabla)E + \frac{\alpha \cdot \partial E}{c \cdot \partial t} \times B \tag{2.14}$$

Since

$$(E \cdot \nabla)E = \frac{1}{2}\nabla E^2 - E \times (\nabla \times E) \tag{2.15}$$

and

$$\nabla \times E = -\frac{\partial B}{c \cdot \partial t} \tag{2.16}$$

We can get:

$$F = \alpha(\frac{1}{2}(\nabla E^2) + \frac{\partial}{c \cdot \partial t}(\overrightarrow{E} \times \overrightarrow{B})) \tag{2.17}$$

where $\overrightarrow{E} \times \overrightarrow{B}$ equals the beam intensity I_0. Thus, the gradient force of the tweezer can be expressed as:

$$F_{grad} = \frac{1}{2}\alpha \nabla E^2 \tag{2.18}$$

Since α is related to the effective refractive index n_1/n_0, the dielectric sphere with a higher refractive index (assume n_0 is the constant) will generate a stronger gradient force that attracts the sphere towards the focal point. Besides, the polarizability is proportional to the third power of the particle's radius, as we can find in equation 2.8. So, the gradient force also has a third-power relationship with the radius, whereas the scattering force has a six-power relationship with the radius. As the particle get smaller, the gradient force becomes dominant in this system.

2.2.2 Bethe's Aperture Theory

Generally, when the light goes through an aperture, like a rectangular or a hole, on a metal slide, if the size of the aperture is much smaller than the incident wavelength, the light will be stopped in front of the aperture and thus cannot propagate. This physical mechanism can be derived from the boundary condition of the electromag-

netic field within the aperture. The light is diffracted at the edge of the aperture since the propagating wave cannot satisfy the boundary condition and the tangential electrical field on the boundary will become zero. Bethe first worked to solve the problem of the diffraction of electromagnetic waves by a small hole in an infinite conducting plane. His initial system is as shown in Figure 2.5.

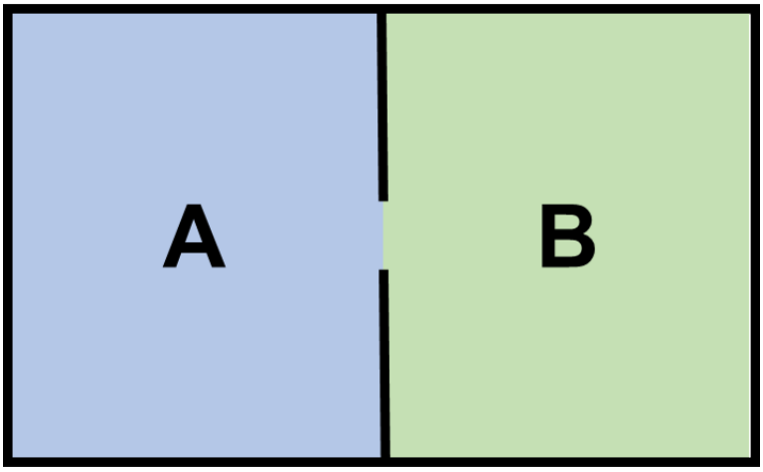

Figure 2.5: Bethe's problem in this aperture theory [71, 72]. The investigation of the transmission through a hole in a metal waveguide screen with two cavities.

In this thesis, we will introduce an easy way to reproduce Bethe's result: quasi-static approximation. If we assume there is an objective that is much smaller than the incident wavelength, the field will change much faster in space than in time. Under this situation, we can ignore the time dependence and calculate the field around the objective by only using electrostatics boundary matching conditions. If we think about a case that consists of a circular hole, whose diameter is much smaller than the incident wavelength, and an infinite perfect electric conductor (PEC) plane. The incident plane wave normally to the PEC plane, which means the electric (E) and magnetic (M) fields are parallel to the PEC plane. The light diffracted by the circular hole can be approximated estimated by a magnetic dipole. We can study the transmission of this condition by solving the boundary condition of the M potential at both sides of the PEC plane [73]. The transmitted power through the hole in free space can be expressed as:

$$T = \frac{1}{2}\frac{4Z_0\pi^3}{3\lambda^4}(\frac{8r^3}{3}H_0)^2 \propto \frac{r^6}{\lambda^4} \tag{2.19}$$

where Z_0 is the impedance of the free space and λ is the incident wavelength. r is the

radius of the circular hole and H_0 is the M field of the incident light. We can easily find from equation 2.19 that the transmission through a subwavelength aperture is proportional to $\frac{r^6}{\lambda^4}$. This mechanism can be illustrated by Figure 2.6

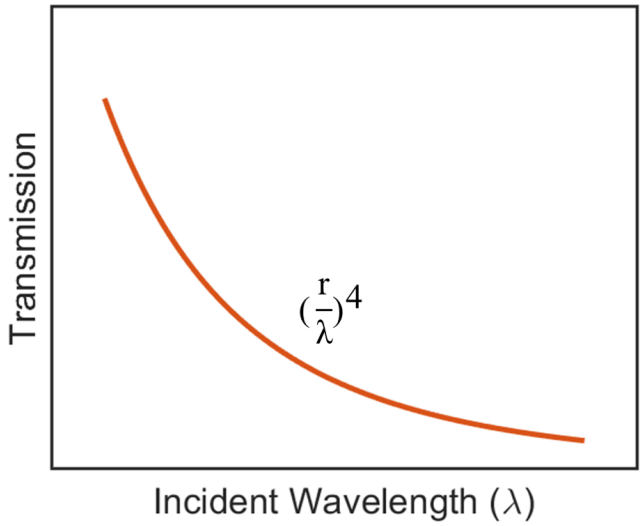

Figure 2.6: A schematic of the transmission of the light through a subwavelength aperture. The optical transmission is proportional to the inverse fourth power of wavelength.

2.2.3 Self-induced back-action Trapping with Nanoholes

Based on what we calculated in the last section. If the aperture is immersed with a surrounded dielectric medium with a refractive index n_0, the equivalent wavelength in the medium is $\lambda = \lambda_0/n_0$. So, the optical transmission with the same aperture can be expressed by:

$$T = \frac{1}{2}\frac{4Z_0\pi^3 n^4}{3\lambda^4}(\frac{8r^3}{3}H_0)^2 \tag{2.20}$$

A sharp increase in the refractive index can lead to a significant increase in the power of the transmission. A small particle loaded near the aperture will induce a great change to the electromagnetic field, which has a great back-action to the particle. Based on this, Gordon and Quidant et al. proposed a theory called self-induced back-action (SIBA) optical trapping using nanoholes [74]. This work shows that the nanoparticle itself has a strong influence on the local electric field near the trap and hence the nanoparticle plays an important role in the trapping mechanism.

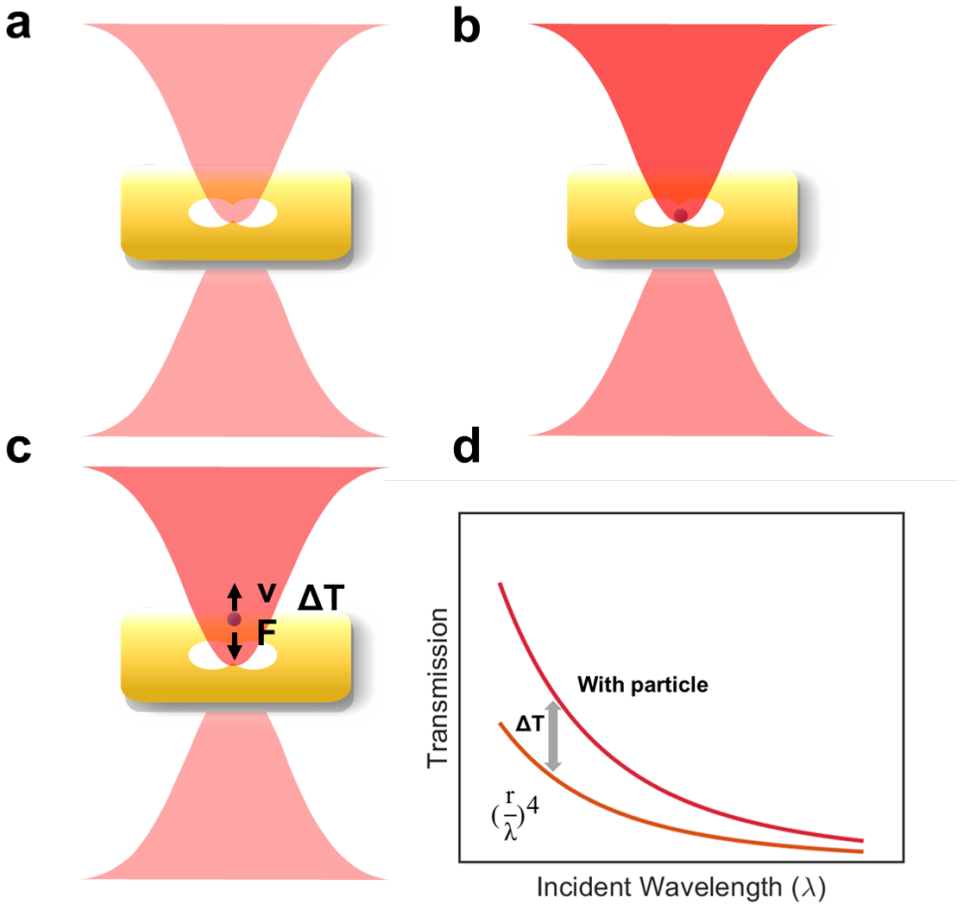

Figure 2.7: Optical transmission through a subwavelength nanohole (a) No particle near or in the aperture. (b) A trapped particle which enhanced the transmission by dielectric loading of the aperture. (c) Decrease in transmission (δT) when the particle lost trapping and (d) A shift in the transmission power that observed under the trapping and untrapping state.

The work that will be demonstrated in Chapter 4 is based on DNH apertures. The advantage of using a DNH aperture is its ability to localize a large field gradient within an extremely small region, which is smaller than the diffraction limit around the cusps [75]. Figure 2.8a shows the electric field distribution of the DNH aperture at 980 nm incident light [76]. It is clear to demonstrate that near the cusp the electric field is the largest. In this paper, the structure with 32 nm cusp separation has peaks at 720 and 940 nm [76]. The simulation is done by using finite difference time domain (FDTD) simulation.

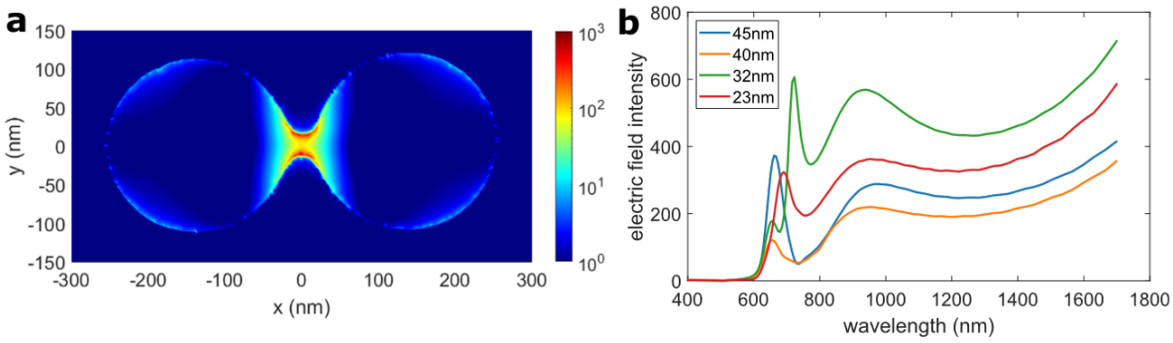

Figure 2.8: Simulated results by using FDTD. (a) Visualization of the electric field intensity inside of a DNH. (b) Electric field intensity for DNHs with different cusp separations. (Normalized to the incident intensity) Ref [76]. Copyright © 2021 Author(s). Published under license by AIP Publishing.

2.2.4 Other Plasmonic Optical Tweezers

With the rapid development of nanofabrication methods and techniques, it has improved the possibility to let researchers study plasmonics at the nanoscale, especially with optical tweezers [77]. Nano-apertures and nano-patterns were recently fully studied by many groups for plasmonic trappings, such as nanoholes [35], bowties [78], rings [79], rectangular holes [80], and co-axial nano apertures [81]. Currently, these methods can be separated into two different groups [82]: the embossed nano-patterns (Figure 2.9a-e), which can generate potentials around the patterns, and the hollow nano-apertures (Figure 2.9f-j), which can excite hotspots inside the aperture as is shown in Figure 2.9.

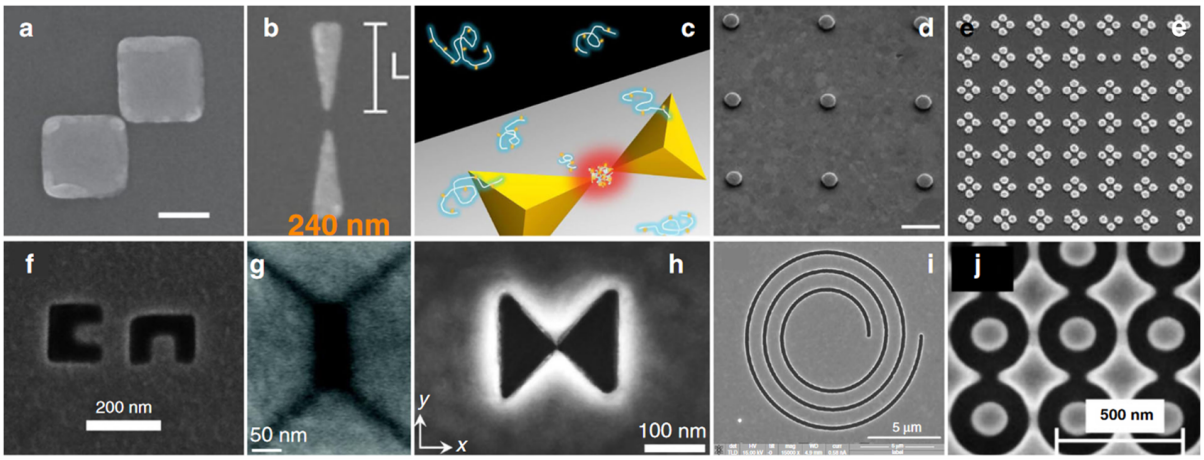

Figure 2.9: Different kinds of plasmonic nanostructures for optical trapping [82]. a. Reproduced from ref. [83], Copyright © 2013 American Chemical Society. b. Reproduced from ref. [84], Copyright © 2018 American Chemical Society. c. Reproduced from ref. [85], Copyright © 2012 American Chemical Society. d. Reproduced from ref. [86], Copyright © 2011 Macmillan Publishers Limited. e. Reproduced from ref. [87], Copyright © 2013 American Chemical Society. f. Reproduced from ref. [88], Copyright © 2014 American Chemical Society. g. Reproduced from ref. [80], Copyright © 2011 American Chemical Society. h. Reproduced from ref. [89], Copyright © Springer Nature the Authors 2018. i. Reproduced from ref. [79], Copyright © 2014 American Chemical Society. j. Reproduced from ref. [90], Copyright © IOP Publishing Ltd.

2.3 Sizing Single Nanoparticle with Optical Tweezer

DNH optical tweezer has a promising way to explore more information at the single molecule level. It was possible to estimate the size of each isolated trapped PQD by analyzing thermal motion-induced fluctuations. From Ref [91], it shows that the current technology can be sensitive to larger than 50 kDa proteins. However, the DNHs offer a chance to capture 6.5 kDa protein and study its properties (as is shown in Figure 2.10).

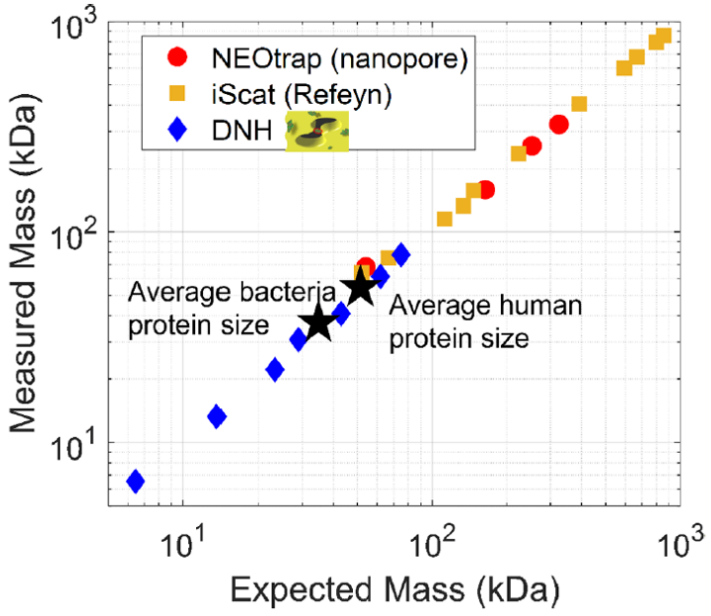

Figure 2.10: Various proteins measured by three different techniques. Reprinted with permission from [91] © 2022 American Chemical Society

By analyzing the autocorrelation of the time series signal, an exponential decay time (τ) can be found, which is a measure of the trapping stiffness used in the trapping [92, 93]. Here, we consider the force on the trapped particle by using Newton's second law of motion,

$$F = m\ddot{x} = -\kappa x - \gamma \dot{x} + F_L, \tag{2.21}$$

where γ is the Stokes' drag, κ is stiffness and F_l is the Langevin term that accounts for Brownian motion. If we assume $F = 0$ and ignore the noise term in Eq. (2.21), we can obtain τ:

$$\tau = \frac{\gamma}{\kappa} \tag{2.22}$$

Since $\kappa \propto \Omega$ and $\gamma \propto \frac{1}{r}$, where Ω is the volume and r is the radius of the nano-particle

(assume the nanoparticle is more like a sphere), then

$$\tau \propto \frac{1}{r^2} \rightarrow \tau \propto \frac{1}{\Omega^{\frac{2}{3}}}. \tag{2.23}$$

Using Eqs (2.22)-(2.23), we can find the relationship between τ and the volume is proportional to the $-\frac{2}{3}$ power. Also, we then find $F \propto \Omega \propto M$, where M is the mass of the particle. When the protein is trapped by our nanoplasmonic optical tweezer, we should also consider the serface effects [94, 95, 96]. Faxén's law can be used to calculate a corrected Strokes drag:

$$\gamma = \frac{6\pi\eta r_0}{[1 - \frac{9}{16}(\frac{r}{h}) + \frac{1}{8}(\frac{r}{h})^3 - \frac{45}{256}(\frac{r}{h})^4 - \frac{1}{16}(\frac{r}{h})^5]} \tag{2.24}$$

where η is the viscosity of the medium and h is the distance from the protein to the wall.

In Ref [96], Ying's team use this method (Figure 2.11) to calculated the trapping stiffness of single proteins with different sizes:

In Ref [94] the results of the protein study (Figure 2.12) demonstrate the positive linear dependence between the molecular mass of the standard protein and the fluctuations of its trapped signal. Then they tried to find the relationship between the molecular mass and the time constant of the trapping signal. Figure 2.12b shows the -2/3 power dependence of the autocorrelation relaxation time for the trapped proteins with the respect to their molecular weight. The standard deviation of the light scattering scales linearly with the size [94]. This has been applied to study heterogeneous solutions of proteins [95]. In our group's previous work on egg protein, we also use this technique to find the relationship between the standard deviation and the autocorrelation function time constant of ovotransferrin and ovalbumin trapping events, as shown in Figure 2.13. The linear curve is fit to the events in the graph and has a slope of -2/3 on a log-log plot.

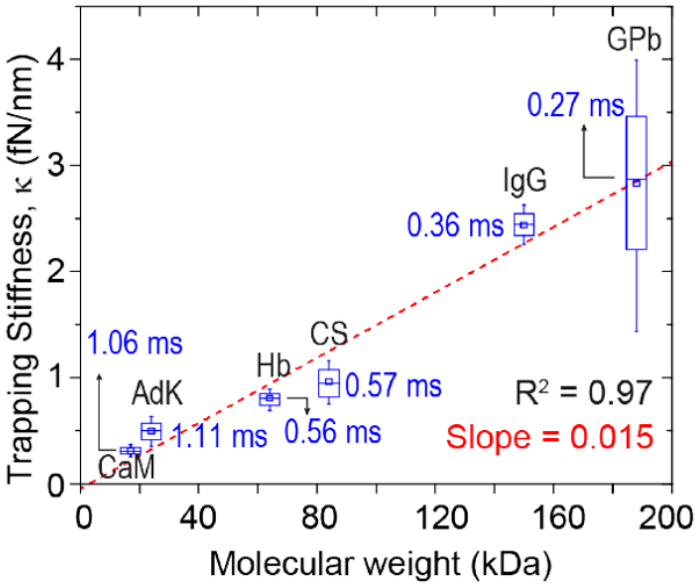

Figure 2.11: Box and whisker plots of trapping stiffness for proteins with different molecular weights, trapped at a laser power of 23 mW. The trapping stiffness was calculated using the time constants from the autocorrelation function of each protein, labeled next to each box. Median values of trapping stiffness were fit linearly (dashed red line). The boxes span the interquartile range, the middle lines are median values, and the open squares are mean values. Reprinted with permission from [96] © 2021 arXiv

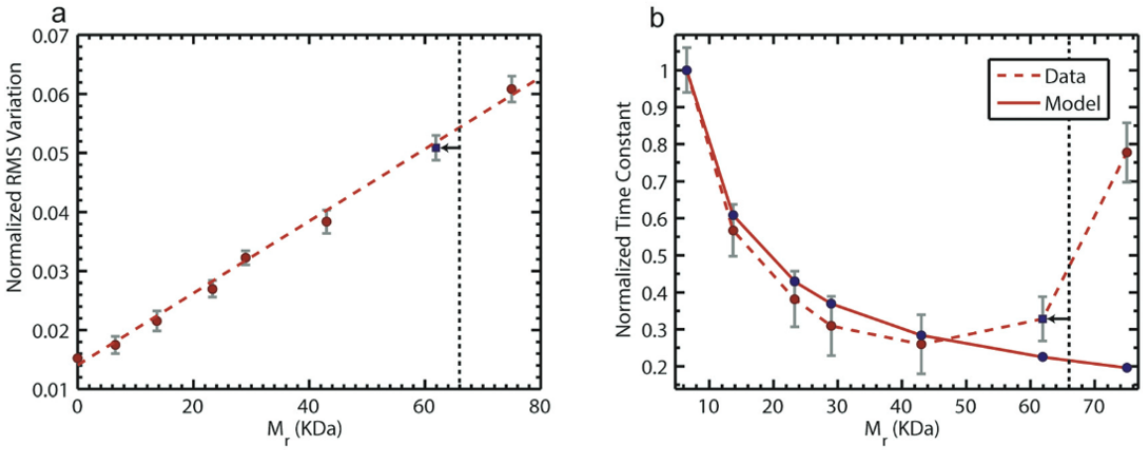

Figure 2.12: Root mean square (RMS) variation of trapped particles, autocorrelation of trapped particles. (a) RMS of the trapped particles with respect to their molecular weight. (b) Autocorrelation relaxation time for the trapped particles with respect to their molecular weight. Reprinted with permission from [94] © 2015, the Royal Society of Chemistry

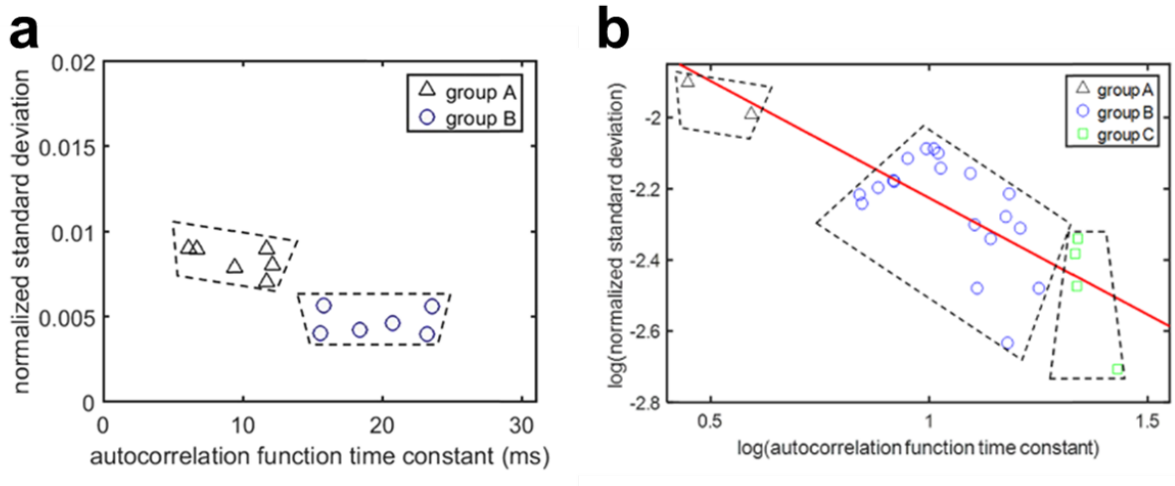

Figure 2.13: (a) SD and ACF time constant (τ) of ovotransferrin and ovalbumin trapping events. A mixed solution of ovotransferrin and ovalbumin (1:1 ratio by volume). (b) SD and ACF time constant (τ) of egg white trapping events. SD of trapped signals with respect to their τ. Trapping events in group A were classified as particles with a molecular weight higher than 49 kDa; trapping events in group B were classified as trapped particles with a molecular weight in the range of 36$\sim$49 kDa, and trapping events in group C were classified as trapped particles with a molecular weight lower than 39 kDa. Reprinted with permission from [95] © 2018, American Chemical Society

2.4 Nanophotonic-Enhanced Methodology with Quantum Dots

Various methods based on nano-plasmonics have been used to study colloidal quantum dots [97, 98, 7, 99, 100]. Quantum dots, which have a higher index of refraction, has been the most attractive candidates for optical trapping based on SIBA. As we reviewed in the last section, quantum dots can increase the trapping force. It is worth studying their electric properties at room temperature deeply since optical tweezers can generate a strong local electric field to exert on the dots. Oddershede et al. studied the two-photon quantum dots excitation by using optical trapping to capture individual dots [101, 77]. As shown in Figure 2.14, Bawendi et al. demonstrated a bowtie aperture for trapping individual silica-coated quantum dots and studied the light-matter interactions and multiphoton process in the single emitters [78]. Wenger et al. used nanoantennas to enhance the emission the photoluminescence [7].

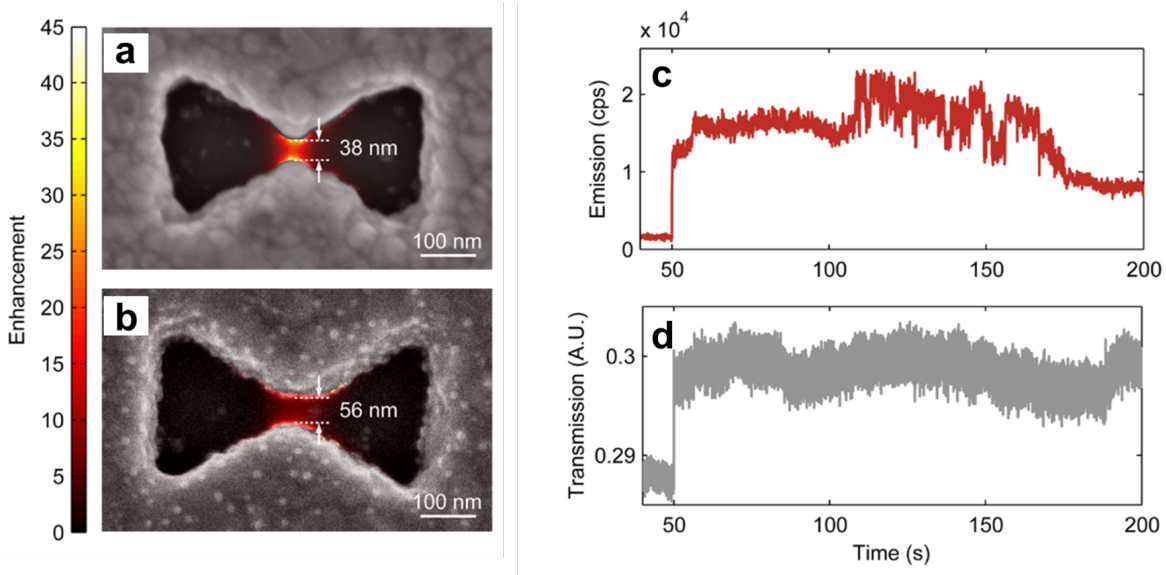

Figure 2.14: (a, b) Scanning electron microscope (SEM) images of the bowtie apertures used in the experiments, overlapped with field intensity enhancement profiles at 1064 nm. The confined gap mode is dominant when the polarization is across the gap. (c) Emission and (d) 1064 nm transmission channels show a stepwise increase in signal at 50 s, indicating individual scQD trapping. Adapted from [78]. Copyright © 2016 American Chemical Society.

For CsPbBr3, Cao et al. adopted gold nanorods to enhance the photoluminescence, as shown in Figure 2.15 [103]. Becker et al. shown in Figure 2.16, studied

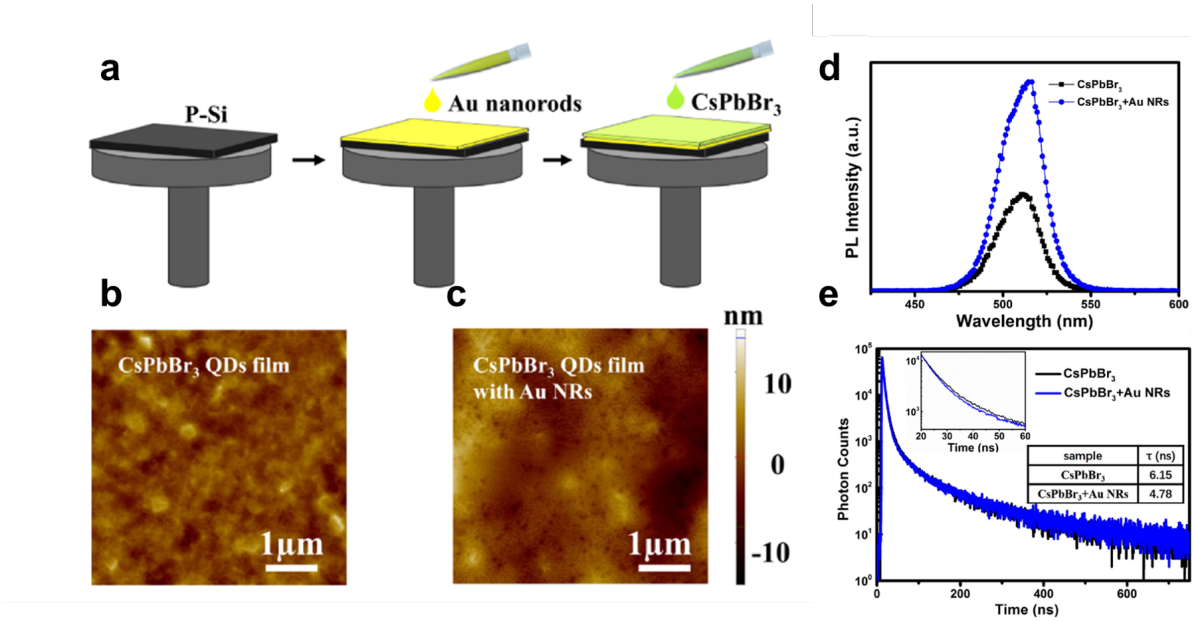

Figure 2.15: (a) Schematic illustration of fabricate the Au NRs/CsPbBr3 film. The AFM image of (b) CsPbBr3 QDs film and (c) CsPbBr3 QDs film with Au nanorods. (d) PL spectra of CsPbBr3 QDs film and Au NRs/CsPbBr3 QDs film under 375 nm. (e) Time-resolved photoluminescence spectra of Au NRs/CsPbBr3 QDs film under 405 nm excitation. The insets are corresponding lifetime and TRPL spectra at a short time scale for two samples, respectively. Adapted from [102].

the two-photon excitation of PQDs with silicon photonic crystal slab (nanohole array) [102]. However, they didn't study the individual level of PQDs. Characterizing single-particle-level of PQDs by using an optical tweezer is necessary explore. In this thesis, we will offer a possible chance to study individual particles of PQDs in solution and room temperature with DNH apertures.

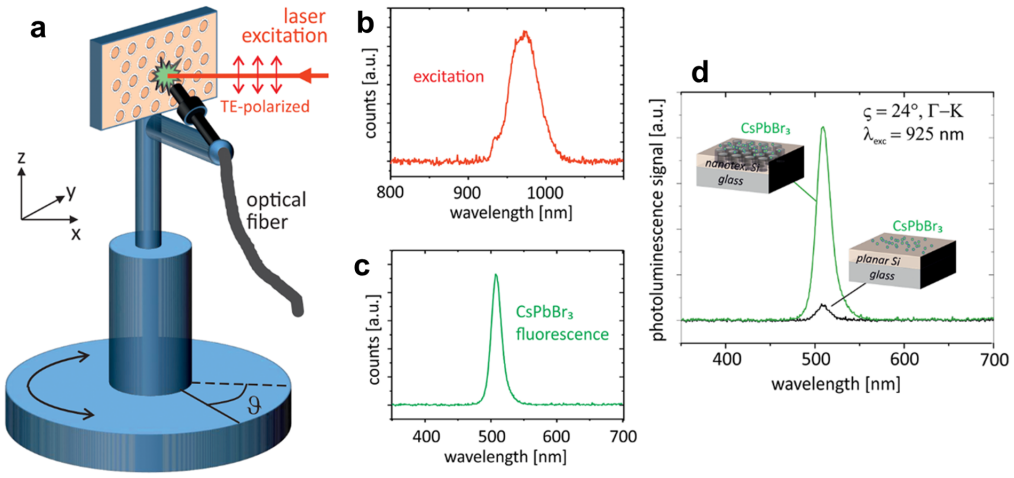

Figure 2.16: (a) Schematic of the pivoted sample holder, enabling excitation by two-photon absorption at tunable incident angle θ. During rotation, the optical fiber collecting the photoluminescence is fixed with respect to the measurement spot, always facing the sample surface at normal incidence in the XY−plane and $\theta = 45$ concerning the vertical direction. (b) The example excitation spectrum of the incident laser beam. (c) Example CsPbBr3 photoluminescence spectrum. Examples of photoluminescence spectra for excitation at $\lambda_{exc} = 925\ nm$ and an incident angle of $\theta = 24$ with the excitation beam hitting CsPbBr3 quantum dots located on either a nanotextured area (green curve) or a planar area (black curve) of the silicon layer. Adapted from [103]. Copyright © 2018 American Chemical Society

2.5 Energy Transfer Mechanism between Two Quantum Dots

To improve the optoelectronic properties of quantum dots, we cannot ignore the interaction between individual quantum dots, which are in the nanoscale and have small distances between each other. By investigating the interaction between the adjacent quantum dots, we could find a way to reveal the mystery of quantum mechanics. Energy transfer and coupling between two PQDs have been studied by several groups. Different ideas, such as resonant energy transfer, charge transfer, and electron hybridization have been proposed. In 2020, Shaw et al. presented a research that failed to get PQDs to transfer their photon energy to a silicon substrate [104]. Coupling between two quantum dots is possible to be applied in many areas, such as making high-efficient green-energy-harvesting solar cell [9]. Quantum computing also can benefit from this coupling because it can provide a framework to obtain maximum entanglement for quantum operations through the coherent bidirectional exchange of a near field photon [39, 40].

In this section, we will introduce some possible mechanisms related to the coupling between two nearby quantum dots.

2.5.1 Förster Resonant Energy Transfer (FRET)

How does dot have the ability to talk to another dot? Förster resonance energy transfer could explain this interesting possibility. FRET describes the process of the energy transfer from one excited molecule (e.g. the donor) to a second molecule (e.g. the receptor) through non-radiative dipole-dipole coupling [105, 106, 107, 108]. Generally, the quantum yield (probability) of the energy transfer can be calculated by [109]:

$$E = \frac{1}{1 + (r/R_0)^6} \tag{2.25}$$

where E is the quantum yield of the energy transfer. r is the separation of the donor and receptor and R_0 is the Förster distance of the pair. R_0 depends on the overlap integral of the emission spectrum (donor) and absorption spectrum (receptor) [109]. The R_0 can be calculated by [110, 111]:

$$R_0^6 = \frac{2.07}{128\pi^5 N_A}\frac{\kappa^2 Q_D}{n^4}\int F_D(\lambda)\epsilon_A(\lambda)\lambda^4 d\lambda \tag{2.26}$$

where κ^2 is the dipole orientation factor and Q_D is the fluorescence quantum yield of the donor without receptor. n is the medium refractive index and N_A is the Avogadro constant.

The quantum yield of the energy transfer is inversely proportional to the 6th power of the gap between the two nearby particles. A large change will happen with a small shift in their distance. In the near-field regime, the excited donor emits a virtual photon and is absorbed by the receptor instantly.

2.5.2 Dexter Electron Transfer

Dexter electron transfer was first proposed by Dexter in 1953 [112]. It only occurs at an extremely short distance since this process requires a wavefunction that overlaps between the donor and receptor. During this process, an excited electron transfers from the donor to the receptor very quickly (nanoseconds) [113]. The Dexter energy transfer rate has a relationship with the spectral overlap integral J:

$$K_E T \propto J_e xp[\frac{-2r}{L}] \tag{2.27}$$

where r is the distance between the donor and the receptor and L is the sum of the van der Waals radii.

2.5.3 Hybridization and Electronic Coupling

Electron coupling plays an important role in quantum mechanics. When two atoms get close enough or are even fused. These situations will let their orbitals overlap. The orbital energies will then split into two new states: bonding state and anti-bonding state, as is shown in Figure 2.17. This can greatly change the electronic and optical behavior of the materials. As the particles become closer, the wave functions start to delocalize and the electronic states of each particle start to hybridize, which will lead to a red-shift of the emission and absorption spectrums [114]. Banin et al. recently has developed a methodology to fabricate fused quantum dots and measure their red-shifts [114, 115, 116] . Creating fused CdSe/CdS core/shell colloidal quantum dots have demonstrated energy shifts through hybridization of around 5-12 meV at room temperature [114, 115, 116].

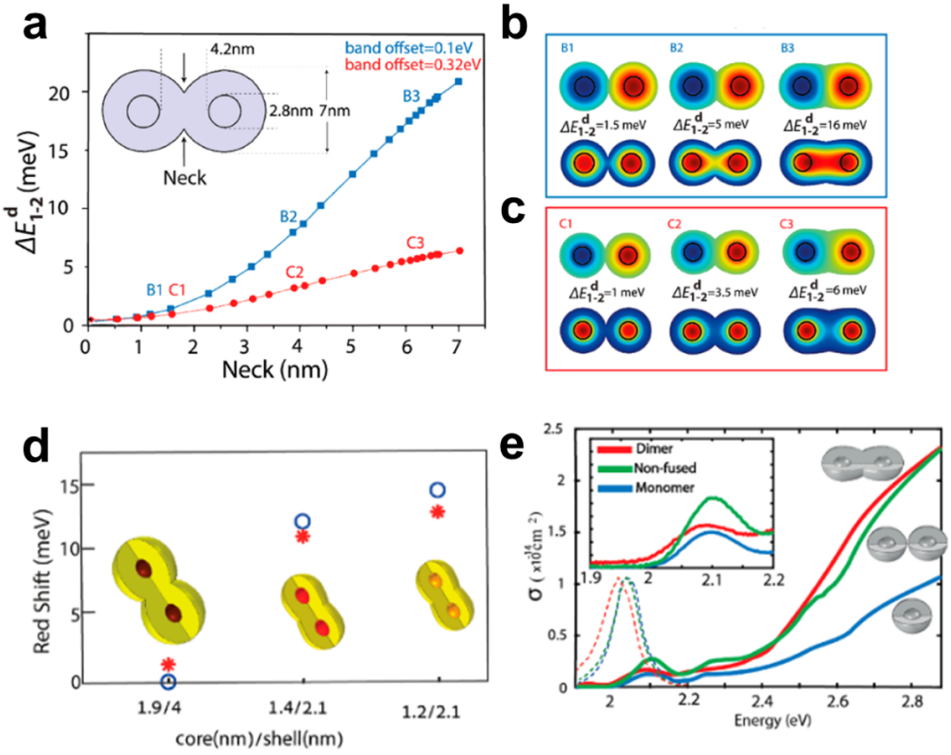

Figure 2.17: (a) Energy difference between the symmetric and antisymmetric states as a function of the neck diameter for the 0.1 eV (blue) and 0.32 eV (red) CB offset in 1.4/2.1 homodimer. (b,c) Wave functions of the symmetric (bottom) and antisymmetric (top) electronic states and the energy difference between them in three points: which refer to 1.5, 4, and 6.2 nm neck thickness, respectively, for the (b) 0.1 eV band offset (B1−B3) and (c) 0.32 eV band offset (C1−C3). Adapted from [115]. Copyright 2019 American Institute of Physics. (d) Calculated (red asterisk) and experimental (blue circles) band−edge red−shift of monomer−to−respective−homodimer structures for different CQD molecules. Adapted from [114, 115, 116], Copyright 2019 Springer Nature. (e) Absorption cross section (solid−lines) and normalized emission spectra (dashed−lines) for the monomer (blue), nonfused dimer (green), and fused dimer (red). Adapted from [115]. Copyright © 2019 American Institute of Physics.

2.6 Finite Difference Time Domain Method

With the development of semiconductor processes and technology, electronic equipment tends to be miniaturized and complex. The problems caused by electromagnetic environmental effects are becoming more and more important. K. Yee first proposed a new method for numerical calculation of electromagnetic field: finite difference time domain (FDTD) [117].

FDTD is a numerical algorithm directly based on the time-domain electromagnetic field differential equation [117]. FDTD is a discrete method of alternating sampling in space and time for the components of E and H of the electromagnetic field in space. The Maxwell curl equation is approximated, so the solution of the time-domain differential equation is transformed into the iterative solution of the difference equation. Figure 2.18 shows an illustration of the Yee cell [117, 118]. There are four magnetic field components around each electric field component; Accordingly, there are four electric field components around each magnetic field component. This spatial calculation method can realize the difference calculation (leap-frog integration method) of spatial coordinates and meet the integral form of the Maxwell equation (shown in Figure 2.19) [117, 118]. This can well simulate the process of electromagnetic field propagation. To achieve a reliable solution for the simulation, the cell's size should be smaller than at least 1/3 of the smallest geometry of the target structure. In this thesis, we use Lumerical FDTD 3D Electromagnetic Simulator (Lumerical FDTD ver. 2020 R2.3) to complete the simulation tasks.

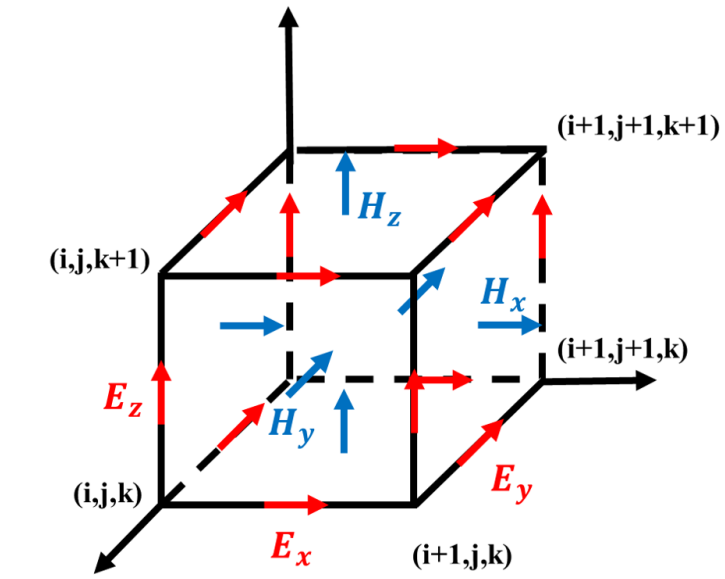

Figure 2.18: Positions of various field components. The E-components are in the middle of the edges and the H-components are in the center of the faces. Adapted from [117] Copyright © 1966 IEEE

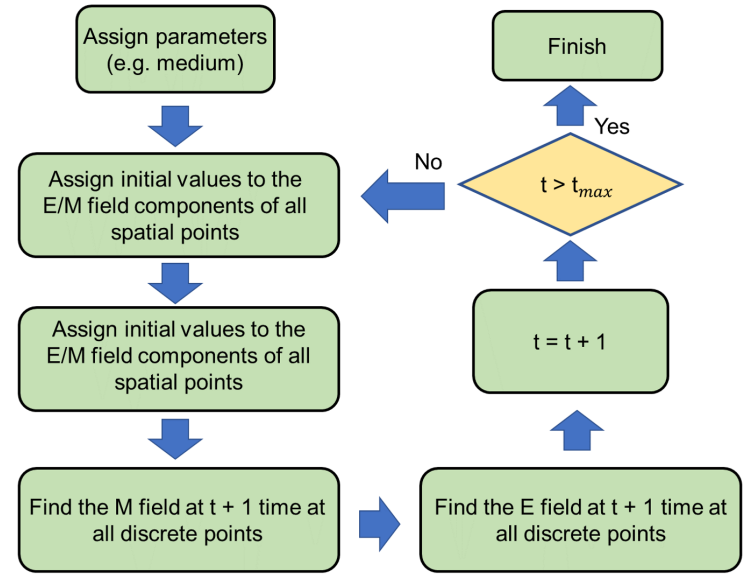

Figure 2.19: Yee algorithm for three dimensional Maxwell equation [117].

2.7 Summary

In this chapter, we first introduced PQDs and their extraordinary properties as the motivation of this thesis. The fundamental knowledge of optical tweezers and DNH apertures were presented as well. Using the trapping setup, we can break through the diffraction limit and explore the electronic properties of extremely small particles in the nanoscale. Several works related to nanophotonic enhancement with quantum dots have also been reviewed. Three important mechanisms for energy transfer between two quantum dots were introduced: Forster resonant energy transfer, Dexter electron transfer, and electronic coupling. Finally, the FDTD simulation method was reviewed.

Chapter 3

Experiment Methods

3.1 Introduction

This chapter will cover the basics of the methods used in the experiments. Firstly, we will introduce the chemistry synthesis method for PQD solution. Secondly, fabrication details of the DNHs gold sample and the trapping setup with DNH tweezers will be covered. Then, we will discuss the preparation procedures for the PQDs sample with DNH optical tweezers.

(Reproduced in part with permission from ACS Nano Letter [41]. Reprinted with the copyright 2022 American Chemical Society)

3.2 PQDs Synthesis and Preparation

Materials used for $CsPbBr_3$ PQDs synthesis Cesium bromide (99.9%), lead bromide (>98%), oleylamine (technical grade, 70%), oleic acid (technical grade, 90%), N,N-dimethylformamide (anhydrous, 99.8%) and toluene (anhydrous, 99.8%). All chemicals were purchased from Millipore-Sigma.

$CsPbBr_3$ PQDs Synthesis Method 4.25 mg of cesium bromide and 14.68 mg of lead bromide were dissolved in 1 mL of N, N-dimethylformamide. To this solution, 5 µL of oleylamine and 125 µL of oleic acid were added. This forms the PQD precursor solution. In another vial, 2.5 mL of toluene was stirred vigorously at 1500 rpm. 250 µL of PQD precursor solution was dropped quickly into toluene under stirring. The solution color immediately changed to green indicating the formation of $CsPbBr_3$ PQDs. This solution was filtered using a 0.2 µm polytetrafluoroethylene syringe filter.

The solution was then used for optical trapping experiments.

Figure 3.1 shows the transmission electron microscope (TEM) image of the as-fabricated PQDs and their size distribution. The shape of the PQDs sample is nearly a square (cube in 3 dimensions). However, there are also several rectangle shapes in the Figure 3.1a,d,g. The side-length distribution calculated by averaging over 150 PQDs is 11.8 ± 1.5 nm . We also measure the distribution of smallest edge sizes, since the PQDs are expected to align along their long sides when pushed together by optical forces, and so the separation is best represented by their small side size. We find the small side size to be 10.5 ± 1.1 nm.

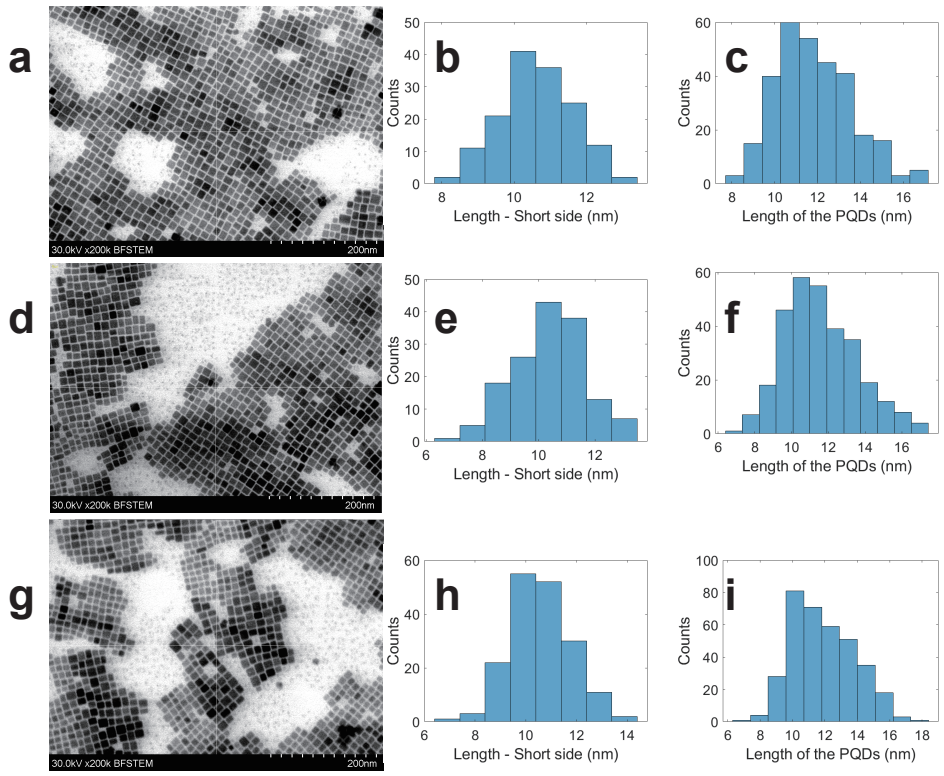

Figure 3.1: (a,d,g) TEM image of the $CsPbBr_3$ sample. (b,e,h) The short-side length distribution of more than 150 different PQDs. (c,f,i) The average length distribution of more than 300 different PQDs.

Figure 3.2 shows a nominal PQD ligand length of 1.4 nm. High resolution TEM was used to image the gap size accurately, but selected larger particles due to working at the periphery of the deposited region. For measuring particle size, regular TEM with large field of view images was used for representative statistics.

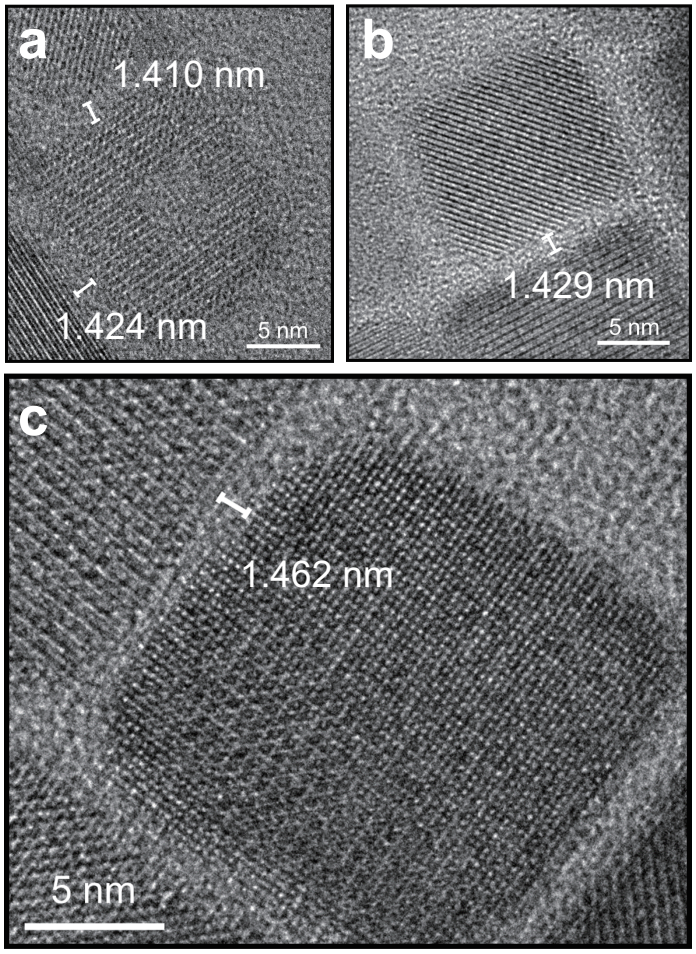

Figure 3.2: High resolution TEM images of $CsPbBr_3$ PQDs. The ligand length is around 1.4 nm.

3.3 DNH Gold Sample Fabrication

The DNH apertures were made by using colloidal lithography, as shown by our group in past works [119, 72]. First, we obtain standard glass microscope slides with 1 mm thickness. We use clean lens paper (Fisherbrand™ Lens Paper) to remove the dust on the slides, double-check the slides have no scratches. Secondly, these slides are cut to the appropriate size using a diamond scribe. The well-prepared slides are sonicated in an ethanol bath by using ultrasonic bath for 10 minutes to clean small dust particles. After that, the slides are dried with compressed nitrogen and cleaned using oxygen plasma for 15 minutes. These slides now can serve as the basic sample substrates for the next procedure.

Before fabricating DNHs, we can choose different diameters of polystyrene spheres, which controls the size of the DNHs [119]. Here, we use diluted 300 nm 0.01% w/v polystyrene spheres in ethanol. This concentration is found to be the most appropriate for colloidal lithography with optimal inter-dimer separation. Figure 3.3a-d shows the process workflow for fabricating DNH apertures with gold. The prepared diluted solution (usually 10 µL) is then drop-coated on the prepared microscope slides uniformly by using a micro-pipette. To isolate the external environment and possible dust contamination, new and clean containers are used to carry the coated slides until moving to the next step. During evaporation, the polystyrene spheres aggregate, as is shown in Figure 3.3a. After the solution evaporates, the polystyrene spheres are stuck to the surface of the microscope slides. The cluster of polystyrene spheres is a dimer that will form a DNH aperture. To adjust the dimensions of the dimers, the prepared samples were plasma etched for 135 seconds. For other sizes of cusp and aperture diameter with different nanoparticles/proteins, we can use Figure 3.4 to choose the etching time. Figure 3.5 shows the plasma cleaner from Harrick PDC plasma cleaner [120].

Once we finish the plasma etching, sputtering is done for the next procedure. Prepared samples for the trapping experiment mentioned in this thesis were sputtered using the Mantis QUBE system, as shown in Figure 3.6. The slides are attached to the sputtering metal plate using double-sided polyamide tape. Before the process is started on the computer, the gold block should be in their respective holders and the screws tightened.. Then, we follow these steps:

1. Start the initial process;

2. Deposit a 7 nm titanium adhesion layer (to make sure gold will stick on the

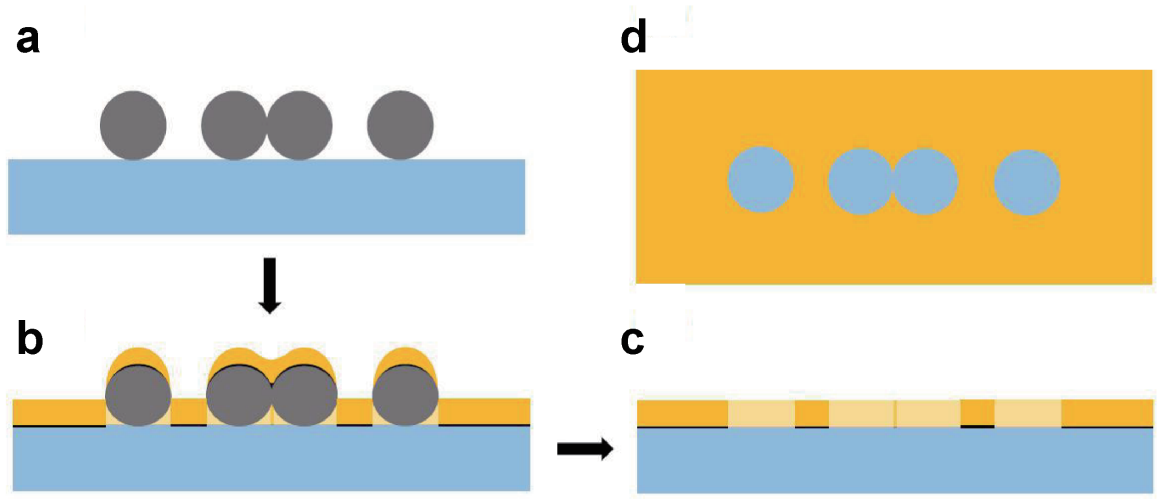

Figure 3.3: Workflow for fabricating double-nanohole apertures with polystyrene spheres [119]. (a) Drop-coated polystyrene spheres on the clean glass slides. (b) After sputtering the titanium layer and gold layer on the slides with spheres. (c) After sonication in the ethanol bath with the desired apertures. (d) Top view of the gold sample with single and double nanoholes. Copyright 2019, Optical Society of America.

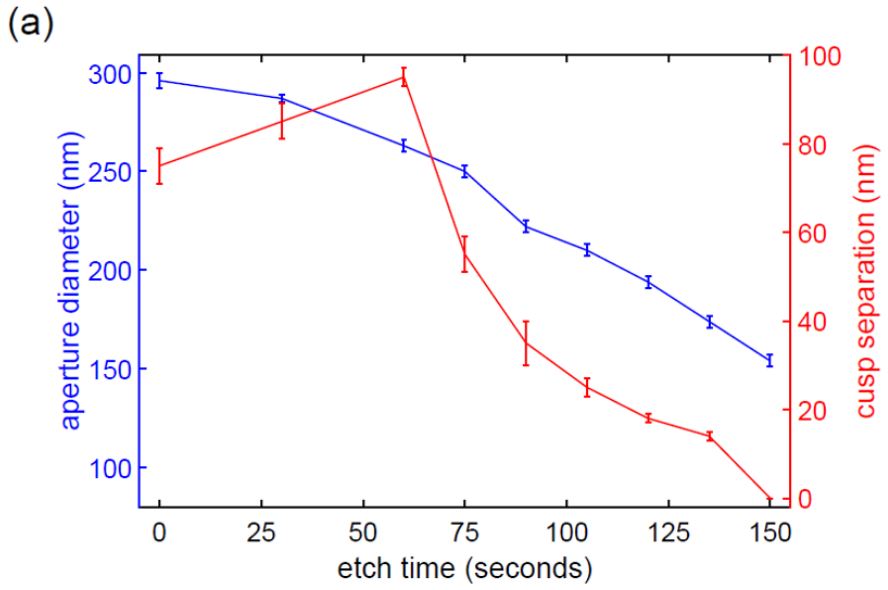

Figure 3.4: Different plasma etching time on the double nanohole dimensions with 300 nm polystyrene spheres [119]. Copyright 2019, Optical Society of America.

Figure 3.5: Harrick PDC plasma cleaner for the fabrication at CAMTEC [120].

sample in the next step);

3. Deposit a 70 nm gold layer

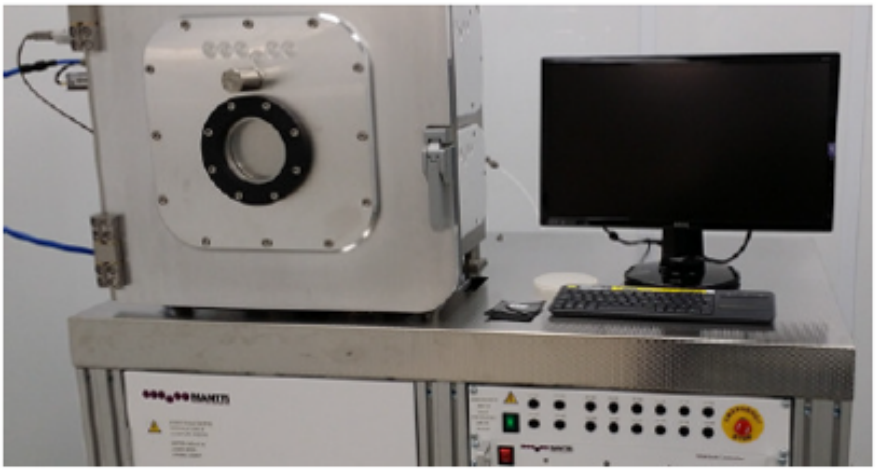

Figure 3.6: Sputter Mantis QUBE sputter deposition system at CAMTEC

After the program is complete, the samples are removed from the chamber and the base plate. The samples are sonicated in an ethanol bath for at least 10 minutes for removing the polystyrene spheres. Then, we finally achieve the desired sample we want, as is shown in Figure 3.3c and d.

The device we use to to locate the double-nanohole apertures and measure the cusp size of the sample, as shown in Figure 3.7, is the Hitachi S-4800 at the AMF, maintained by CAMTEC at the University of Victoria. By using scanning electron microscope images, we can measure the diameter of the nanoholes and the cusp of the DNHs, as is shown in Figure 3.8. The cusp size is the minimum distance (top to bottom) between overlapping areas of two circles. Before imaging, we usually scratch a fiducial mark in the middle of the sample. This step aims to help the operator find the good DNHs quickly under the CCD (charge-coupled device) camera in the trapping setup (as shown in the next section).

In this thesis, the author made a batch of gold samples. For the trapping experiment, the author used the sample with a 16 nm cusp size, which is similar to the length of the edges of the PQD cube.

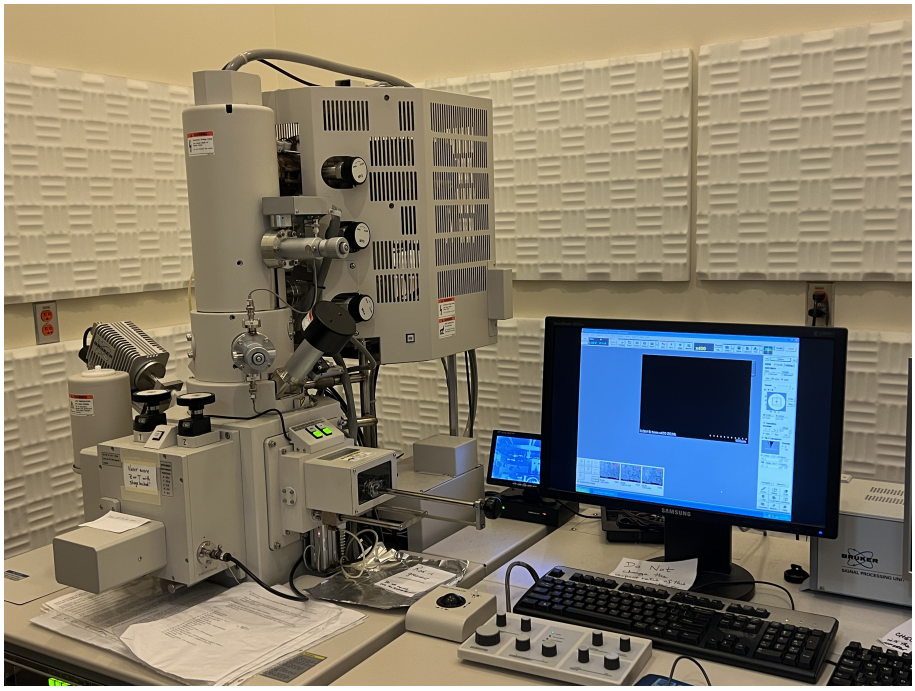

Figure 3.7: The scanning electron microscope setup.

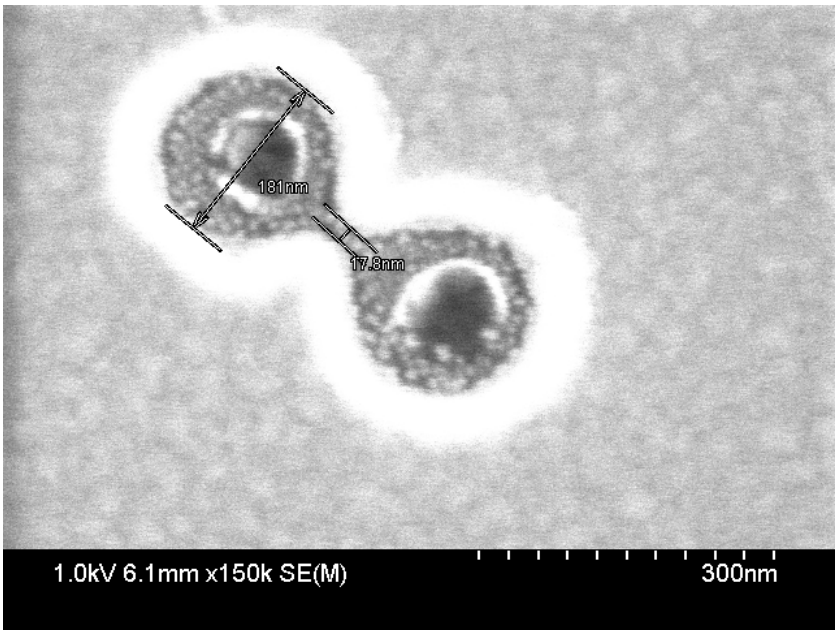

Figure 3.8: Scanning electron microscope image of a double nanohole aperture. The cusp and diameter sizes are 17.8 nm and 181 nm.

3.4 DNH with PQD Solution Sample Preparation

The original PQD solutions were made by Parinaz Moazzezi and Vishal Yeddu. The rest of the sample preparations mentioned below were finished by the author.

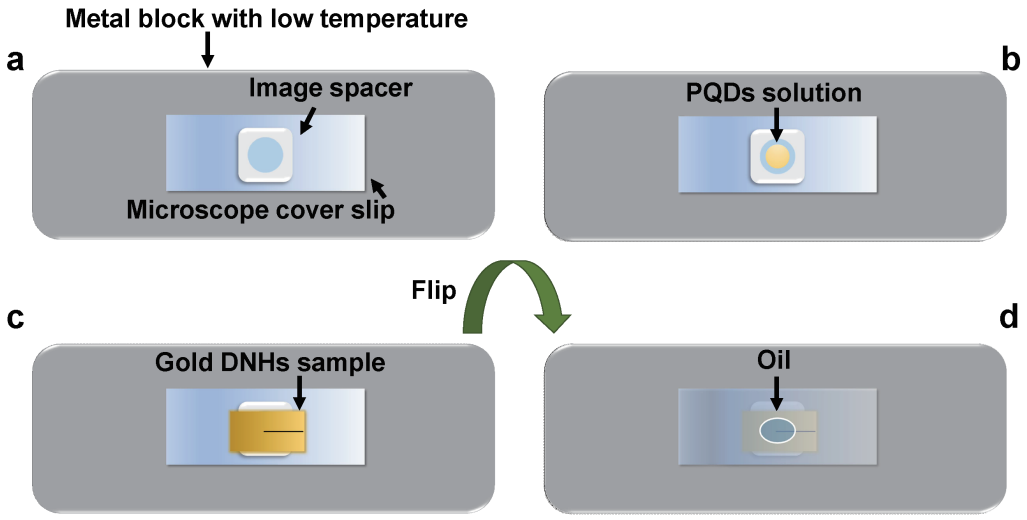

Figure 3.9: Procedure of sample preparation. (a) The cover glass on the low temperature metal block with a double-sided image spacer. (b) Drop 9 μL diluted PQD solution in the middle of the spacer. (c) Immediately cover the microwell with the gold DNH sample to isolate the solution. (d) Flip the cover slide and drop the oil in the middle of the spacer area.

All PQD solutions were diluted in toluene by 20 times. When preparing the diluted solution for trapping, the original solution as sealed carefully and sonicated for 3 minutes to ensure uniform distribution of the PQDs in the tube. A glass cover slide (Gold Seal, 24x60 mm, No. 0. 85-130 micron thick) is used for preparing the sample for the trapping experiment. As is shown in Figure 3.9a, we use a low-temperature (4 ℃) metal block with a flat surface as the plate to hold the cover slide since the toluene evaporates rapidly and the PQDs degrade in a short time with the external environment (temperature, humidity, oxygen, etc). Then, a double-sided adhesive microwell spacer (Grace Bio-Labs, GBL654002) is stuck in the middle of the slide to mount the gold sample. After that, as shown in Figure 3.9b, drop the diluted solution (8-9 μL) in the middle of the spacer. Before drying up the gold sample, which contains the DNHs, using nitrogen gas, it is necessary to be cleaned with hexane, acetone, isopropanol, and ethanol to remove the tiny dust and contamination.

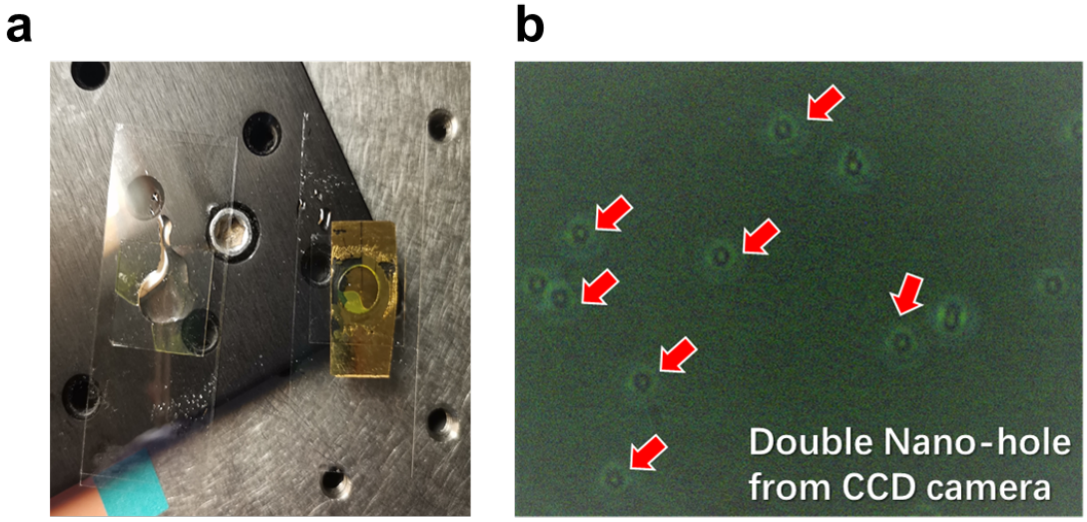

Figure 3.10: (a) The bulk solution sample. (b) The diluted solution with gold DNHs for the trapping experiment.

The gold sample adheres to the microwell spacer, shown in Figure 3.9c, sealing the solution and making sure the DNHs are immersed with the PQD solution. The last step is to drop the oil in the middle of the spacer on the other side of the slide, as shown in Figure 3.9d. The entire assembled sample can be mounted in the trapping setup between the two objectives.

Figure 3.10a shows the bulk-solution sample and the diluted sample with gold DNHs apertures. The oil is dropped in the middle of the spacer. Figure 3.10b shows the DNHs under the CCD camera (red arrows). Due to the limitation of the resolution of the camera, we can only see the holes (include single hole, double or multiple holes.) We use this method to align the laser to one of the apertures, and we confirm that the double nanohole by rotating the polarization and looking at the intensity, and then we just wait for a protein to be trapped [121].

3.5 DNH Optical Trapping Setup

The setup for the trapping measurement is as shown in Fig. 3.11. The setup consists of a 980 nm continuous-wave laser (JDS Uniphase SDLO-27-7552-160-LD). The 980 nm beam was used for both trapping and exciting the PQDs. A half-wave plate (HWP) and a polarizer are mounted in the trapping setup to align the laser beam. The optical work path is collimated, polarized, filtered, and expanded until focusing on the target DNHs with a 100 *times* oil immersion microscope objective, whose numerical aperture is 1.25.

The sample is placed on the three-axis (XYZ) sample stage with piezoelectric adjustment so that the operator can adjust the position easily and precisely. The setup collects the transmission light using a 10× microscope objective from the sample. The transmission light is collected and detected by an avalanche photo-detector (Thorlabs APD120A). A half-wave plate (HWP) and a linear polarizer (LP) are fixed to set and adjust the polarization of the beam. A 750 nm short-pass filter (Thorlabs FES0750) is placed in front of the spectrometer (Ocean Optics QE65000) to reduce the beam intensity from the 980 nm laser. A fiber connected to the spectrometer collects the emission light from the sample. The flip mirror is set to change the optical path to collect the image from the sample using the CCD (charge-coupled device) camera. The procedures to operate the setup:

1. Make sure to drop the oil in the middle of the cover slide (in front of the sample. The detailed procedure for making samples will be introduced in section 3.5)

2. Put the sample on the 3-D stage.

3. Turn on the laser (low power) to find and mark the position of the laser spot.

4. Align the position of the sample to find a good double nanohole aperture near the fiduciary markers using the X and Y axis knobs of the stage and CCD camera. The double nanohole under the CCD camera is as shown in Figure 3.11.

5. Adjust the distance between the objective and the sample by using the Z-axis knob until the sample arrives at the focal point. Then use the piezoelectric adjustment controller to control the position precisely until achieving the best alignment.

6. Turn on the laser and rotate the HWP. If it is a good DNH, the voltage in APD will have a large change.

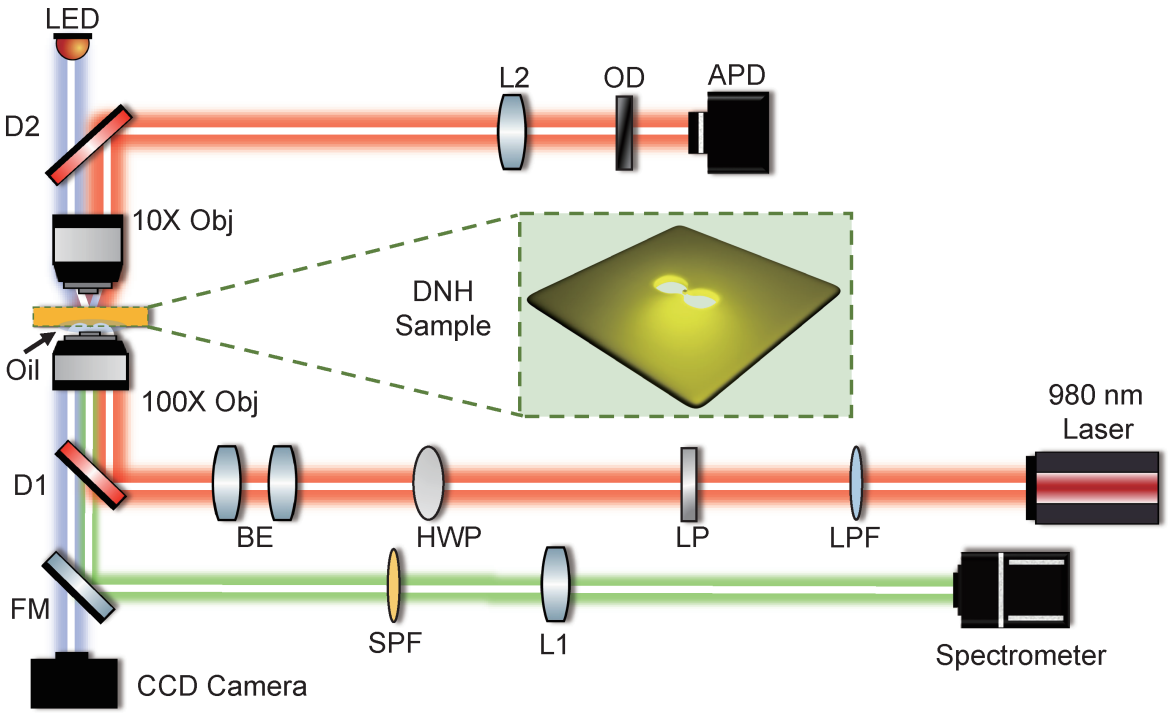

Figure 3.11: Schematic of the optical trapping setup with a 980 nm laser: long pass filter (LPF), linear polarizer (LP), half-wave plate (HWP), beam expander (BE), dichroic mirror (D), objective lens (Obj), lens (L), optical density filter (OD), avalanche photodetector (APD), flip mirror (FM), short-pass filter (SPF), charge-coupled device (CCD).

We use a 100 kHz sampling frequency for the data acquisition system (DAQ) to make sure that the transient trapping data is captured during the experiment. The data collected by the DAQ is easily disturbed by the noise. Nearby electrical lines, optical feedback into the laser source, and structural vibrations in the research building all contribute to the noise. The workflow for the trapping measurement is as shown in Figure 3.12. The APD voltage was displayed by using the Advantech DAQNavi Datalogger software. The emission spectra was displayed and analyzed by using OceanView spectra software.

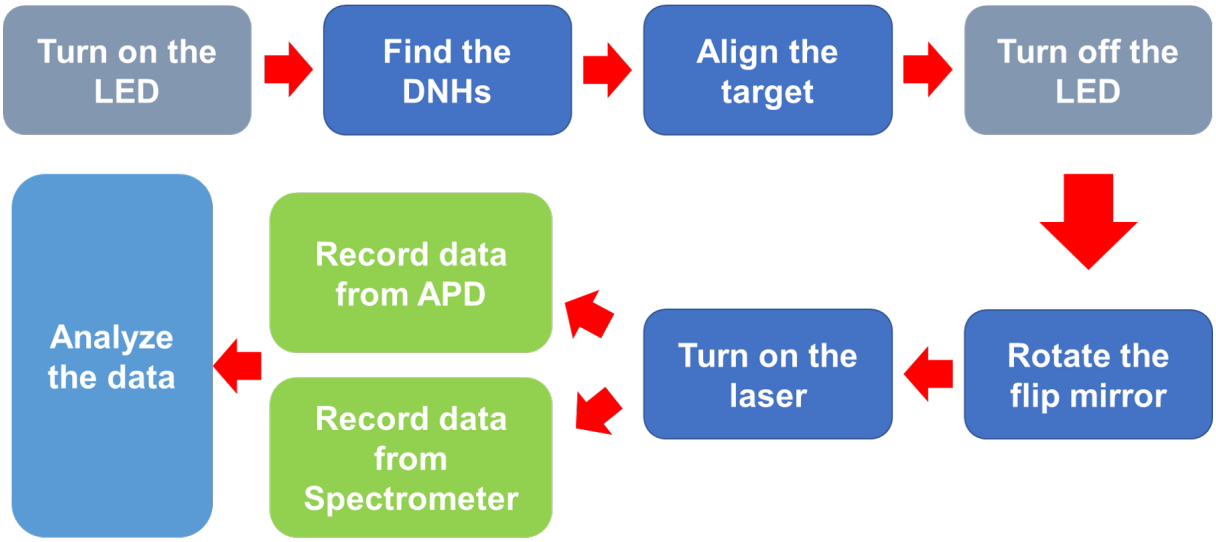

Figure 3.12: Workflow for the trapping experiment.

Chapter 4

Results and Discussion

Hao Zhang fabricated the DNHs, performed the trapping experiments, analyzed the data and did the FDTD simulation. Brett Henderson and Irina Paci contributed to simulation of bandgap and emission energy as a function of single PQD size (section 4.2.3 & 4.3.2). Juanjuan Ren and Stephen Hughes contributed to the theory and simulations of coupled quantum dots (section 4.4 and Appendix 2: *Theory and simulations of coupled quantum dots*). Reuven Gordon advised on the experiments and analysis.

4.1 Background

Perovskite quantum dots (PQDs) show intriguing properties for quantum technologies, such as bright and highly coherent single photon emission [38], and superfluorescence in ensembles of dots [122]. Coupled quantum dots have long been investigated for quantum computing [20, 17]. Many fabrication strategies have been proposed to couple different types of quantum dots, not only PQDs [123, 124, 114, 115, 116, 125]. Assembling quantum dots and studying their quantum coupling in solution would greatly simplify such studies. Furthermore, by assembling in solution, it is possible to study the individual dots prior to assembly, and then study the impact of coupling in the near-field, which is not possible with pre-assembled pairs.

Studying individual dots also allows for probing non-uniformity of the PQDs in solution. Uniformity has been recognized as an important parameter for high-

performance applications [23, 27, 22, 21, 26, 25].

For solar cells, monodisperse PQDs have shown higher conversion efficiencies and open circuit voltages [28]. PQDs are recognized as highly coherent single photon emitters [38]; however, for indistinguishable photons, nearly-identical emitters are desired and this requires a way to select among individual emitters in the ensemble [29, 30]. Past efforts have focused on ex-situ characterization (e.g., transmission electron microscopy – TEM) of already synthesized PQDs. Ideally, particle size would be monitored in solution in real time, allowing for in-situ tailoring of growth conditions while preventing degradation from exposure to the environment.

Here, we use double-nanohole (DNH) optical tweezers to characterize the dispersion of cesium lead bromide ($CsPbBr_3$) PQDs and their coupling in solution. Aperture based optical tweezers have been used to trap quantum dots [126], study their emission (also with two photon excitation) [78], and enhance their single photon emission characteristics [7]. We demonstrate that the DNH optical tweezer can be used to determine the sizes of individual PQDs and correlate size with the emission spectra shifts from quantum confinement. We also demonstrate that the DNH tweezer can capture two quantum dots (i.e., assemble them in real-time) and thereby measure the spectral shift that arises from their coupling. Therefore, this platform enables the spectral and size characterization of single and double dots, and most importantly, it achieves this feat in-situ without removing the dots from the solution or requiring electron microscopy that would damage them.

Multiple physical mechanisms can be responsible for quantum dot coupling in solution. For quantum dots that are nominally symmetric and do not allow for electron tunneling, Förster resonant energy transfer has been considered as a way to achieve coupling between dots, providing a possible avenue towards quantum information processing [39]. In the past, RET has been studied for PQDs of different sizes, where the longer wavelength emission peak is enhanced due to one-directional energy transfer [40]. The bi-directional coupling that arises from just two PQDs that are nominally the same size has not been investigated so far.

4.2 Heterogeneous Particle Sizing

As we introduced in Chapter 3, the target sample $CsPbBr_3$ PQDs were synthesized by the ligand-assisted reprecipitation technique [127]. The size distribution of the shorter edge was characterized by TEM and found to be typically 10.5 nm ± 0.5 nm, as shown in Chapter 3.2, Figure3.2a and b. However, due to the the synthesis experiment system error which we cannot avoid, the size of the PQDs cubes showed a variation of 0.5 nm between separate fabrication runs. We diluted the sample with toluene 20-fold, then placed the solution in a microwell formed by an imaging spacer (Grace Biolabs) on a slide #0 coverslip. A gold film containing DNHs on glass, fabricated using past approaches [119] as we mentioned in Chapter 3, was placed on top of the microwell to seal. We then placed the sample in an inverted microscope optical tweezer setup adapted from a modular kit (Thorlabs – OTKB), shown in Figure 3.11 which has been used previously to study lanthanide nanocrystals [76, 128]. The modified setup included a spectrometer for measuring the spectrum of PQD(s) in the DNH optical tweezer.

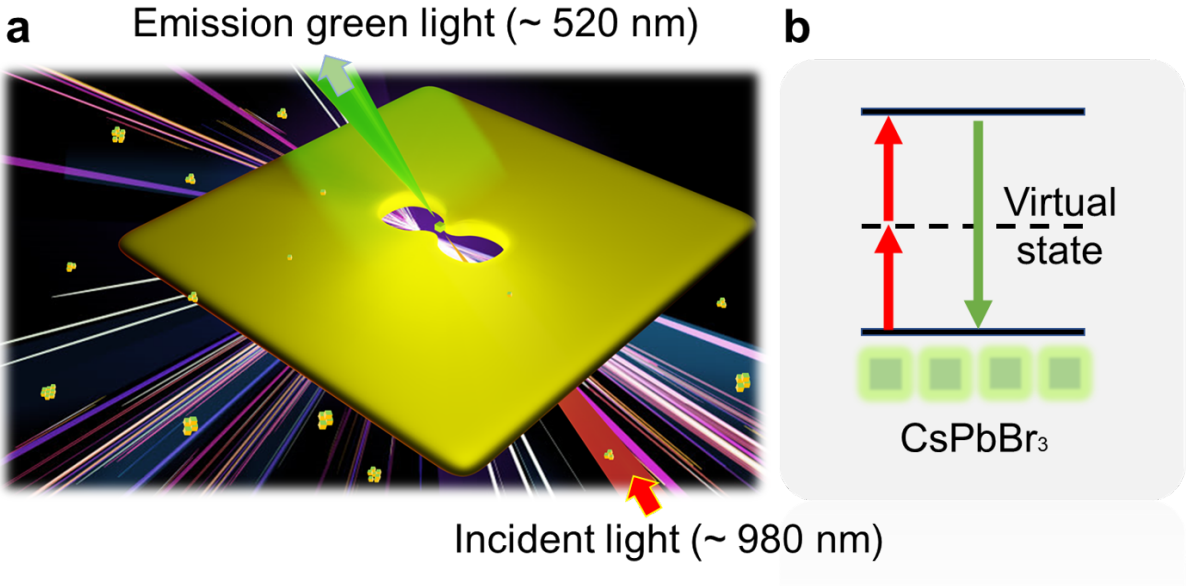

Figure 4.1: (a) The illumination graph of the experiment with double-nanohole aperture and 980 nm incident light. The cubes around the gold sample are the PQDs. The single PQD is in the middle of the aperture. (b) The schematic of two-photon excitation.

4.2.1 Two-photon Excitation

Since the laser wavelength was 980 nm (1.26 eV), and the emission wavelength was 520 nm (2.38 eV), as is shown in Figure 4.1a, the excitation of the PQD was obtained by a two-photon process, as shown in Figure 4.1b. Two-photon excitation of colloidal quantum dots has been observed previously in trapping setups [101, 78]. First, we use the bulk solution to measure the spectra and the power dependence. From the experiment, shown in Figure 4.2, the emission peak is around 520 nm with a narrow linewidth. The power dependence of the bulk solution on a log-log plot. The slope with the best linear fit is around 1.85, as shown in Figure 4.3, which proves the two-photon excitation process. The emission counts were integrated from the collected emission peak from 500 nm to 545 nm.

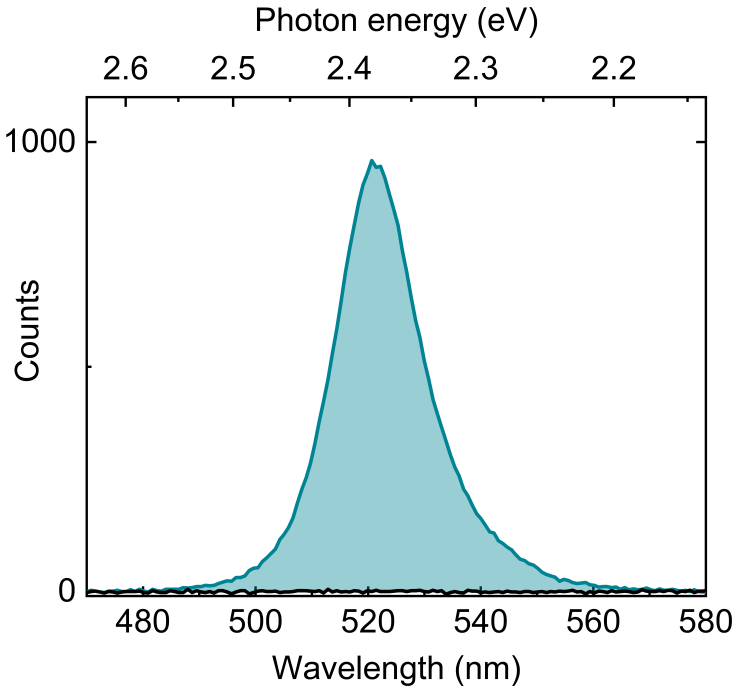

Figure 4.2: The emission spectra from the bulk solution (no DNHs). Black: laser off; Green: laser on.

A step in the transmission of the laser through the DNH was seen with trapping as shown in Figure. 4.4a. This step resulted from the dielectric loading of the DNH by the PQD, which made the aperture optically “bigger", as we introduced in Chapter 2. Several works have confirmed that the single step is the result of an individual nanoparticle being trapped, such as by using fluorescent particles [129] or by noting the dynamics when multiple particles are trapped [80].

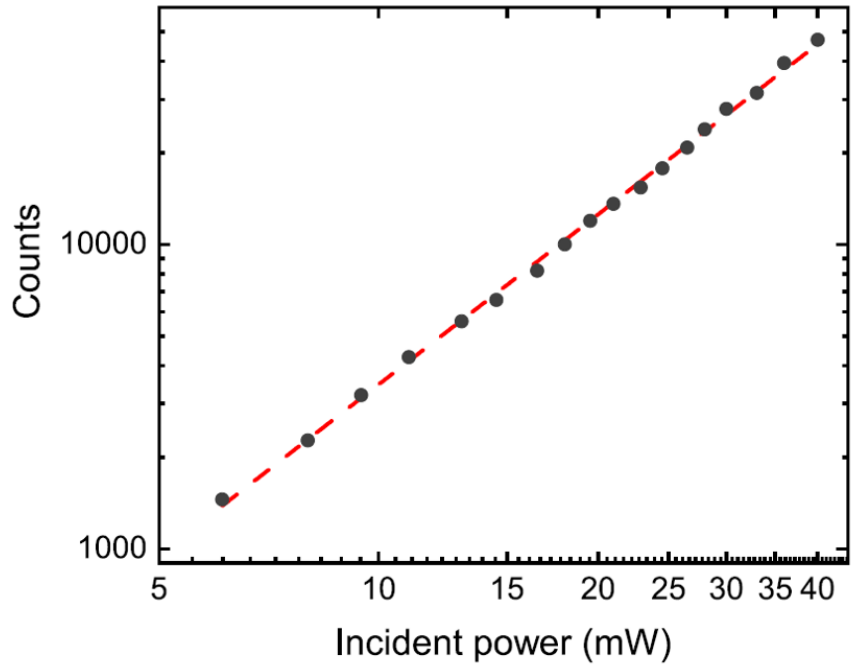

Figure 4.3: The power dependence of the bulk solution (no DNHs) on a log-log plot. The slope is 1.85. The emission counts were integrated from the collected emission peak from 500 nm to 545 nm.

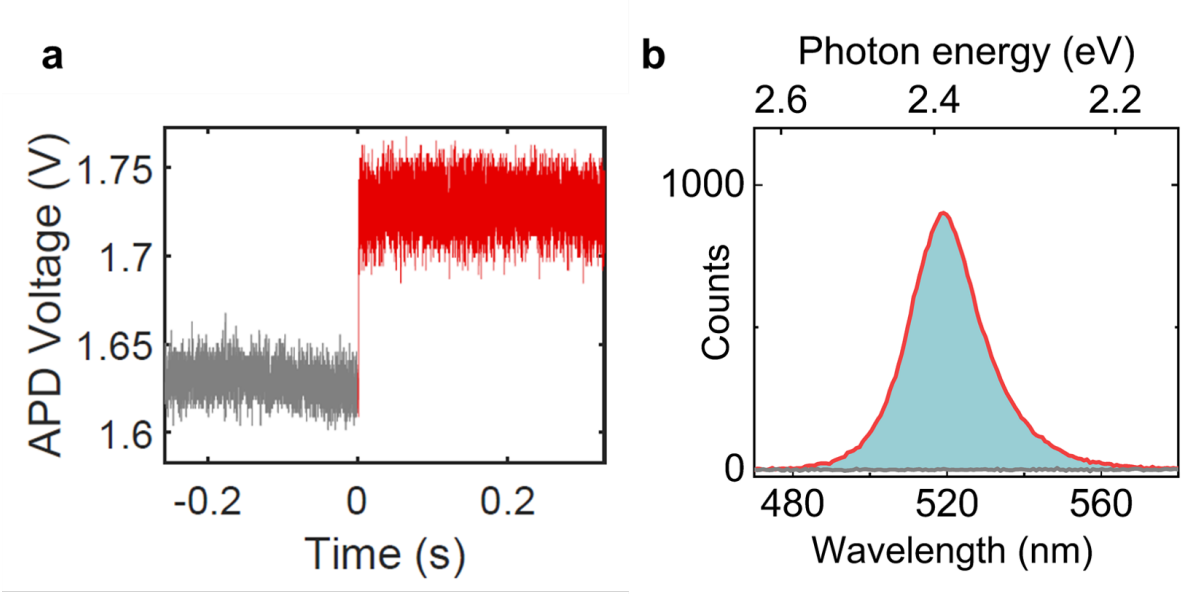

Figure 4.4: (a) The emission spectra from the single PQD by using DNH optical tweezer. (b) Single trapping event from APD collector. Grey: untrapped; Red: trapped.

The spectrum of the single dot is shown in Figure. 4.4b, which was recorded after the trapping occurred. There was no emission observed before trapping. Then, we also measured the power dependence of single PQD by using the optical tweezers. Figure 4.5 shows the power dependence of the single PQD trapping event. The quadratic power dependence is shown on the log-log plot. The emission counts were integrated from the collected emission peak from 500 nm to 545 nm, as well. Figure 4.6 shows that there is little influence on the emission spectra by increasing the input power from 8-40 mW in front of the objective lens.

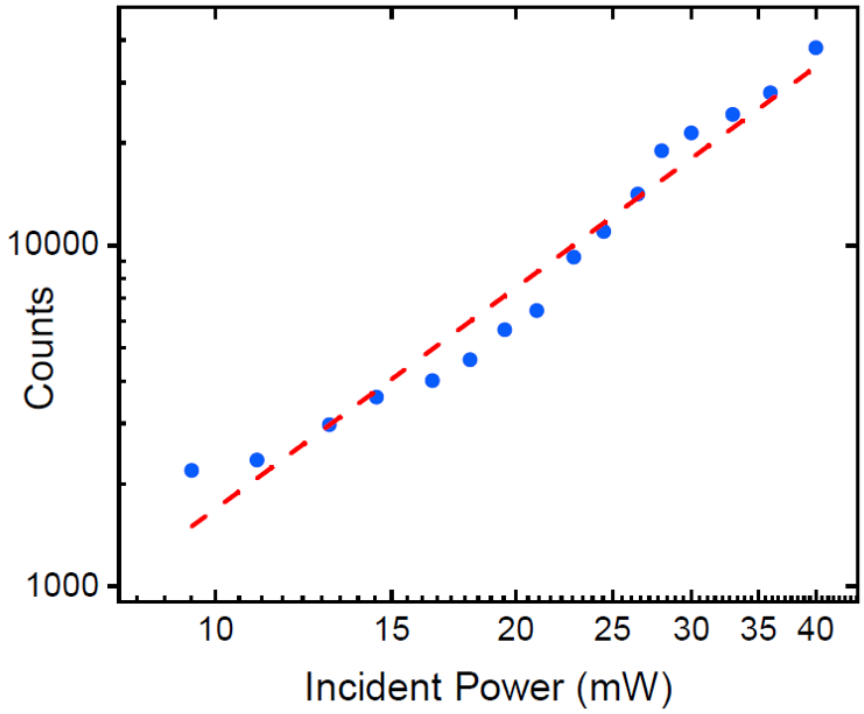

Figure 4.5: The power dependence of the single PQD with DNH aperture on a log-log plot. The slope is 2.15. The emission counts were integrated from the collected emission peak from 500 nm to 545 nm.

4.2.2 Quantitative Analysis by Using the Thermal Motion Characteristics

Here we apply the method that introduced in Chapter 2, to size individual PQDs and correlating PQDs size with the emission spectrum shifts from quantum confinement. In this thesis, we analyze the autocorrelation of the time-series signal, and an expo-

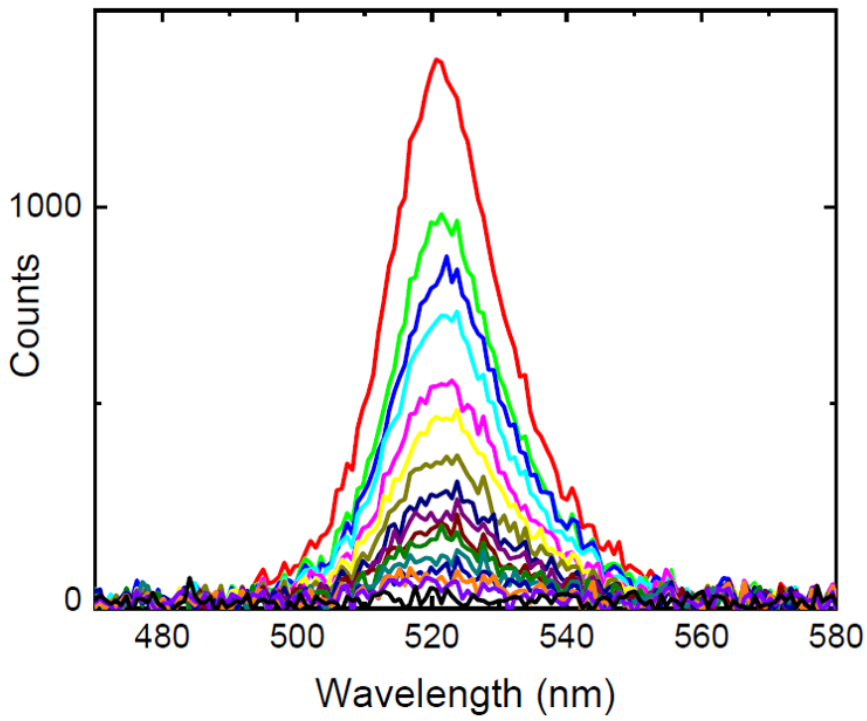

Figure 4.6: The emission spectra under different incident powers.

nential decay time (τ) can be found, which is a measure of the trapping stiffness used in the optical trapping [92, 93]. As demonstrated previously for proteins (but not for PQDs), the autocorrelation time of the thermal motion scales as γ/κ, where γ is the drag coefficient (which scales as the cross-sectional width in the viscous limit) and κ is the optical tweezer stiffness (which scales as the volume of the particle in the dipole limit).

Therefore, for radius r, $\tau \propto r^{-2} \propto \Omega^{-2/3}$ [93, 94], where Ω is the volume.

The standard deviation would have a linear relationship with the mass, which can be estimated by the emission wavelength for PQDs with quantum confinement.

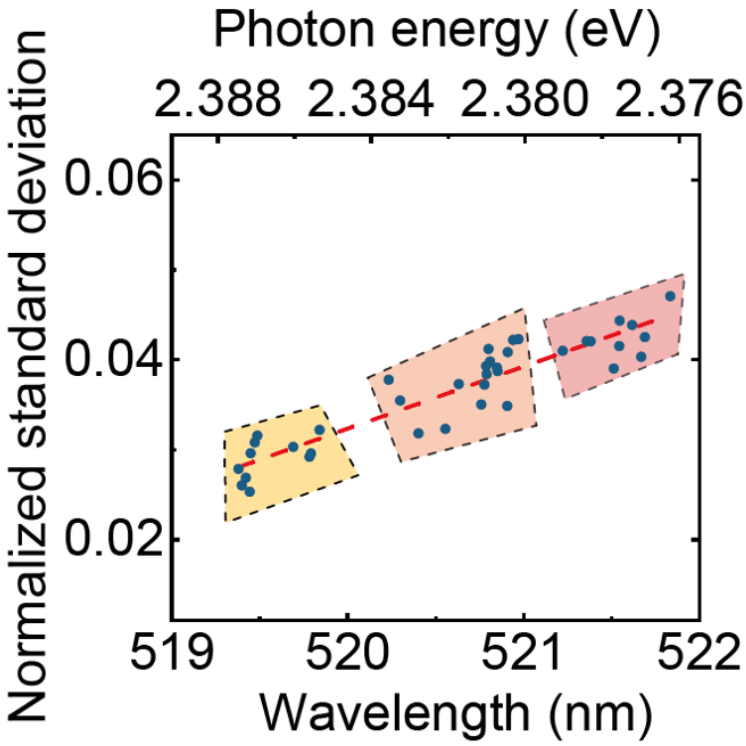

Figure 4.7: Relation between emission wavelength and standard deviation of trapping laser transmission for individual trapped PQDs. Three groups of the sample were measured. This shows that the standard deviation can be used as an independent measure of the particle size, which correlates well with the quantum confinement induced blue-shift.

Figure 4.7 shows the standard deviation of the trapping laser fluctuations correlated with the emission wavelength for individual PQD trapping events. This data was taken from three separate batches and shows a clear separation in the sizes of these batches. However, due to the unavoidable impact from the external environ-

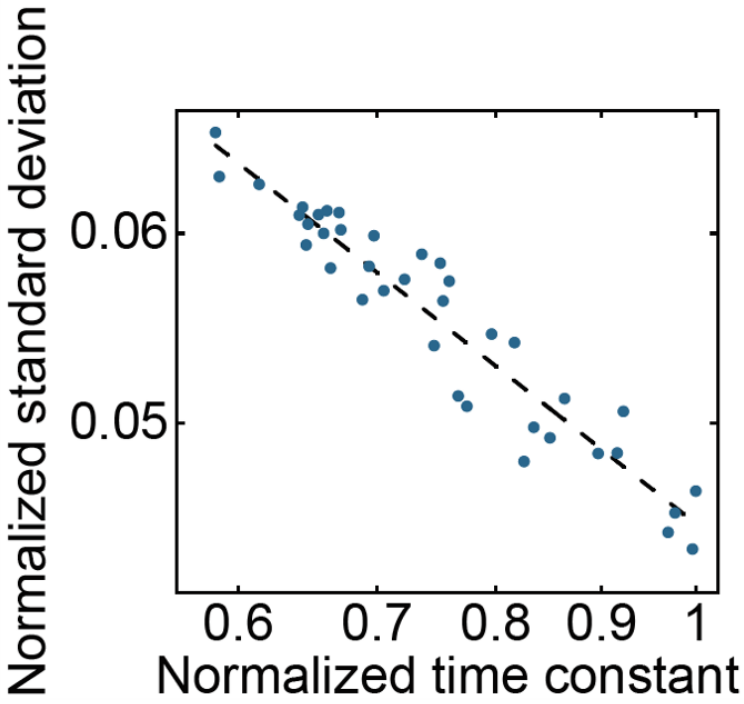

Figure 4.8: Standard deviation against autocorrelation time constant (τ) of the single quantum dots trapping events on log-log plot. The slope for the best linear fit is about -0.68.

ment, the PQDs solution needs to be measured within 12 hours after it has been made.

As described above, it is expected that the standard deviation scales linearly with particle size. For small (first-order) variations in size, it is also expected that the wavelength scales linearly with particle size. Therefore, we observe a linear relationship between the standard deviation and the emission wavelength. We considered the autocorrelation time as a separate measure of particle size, as shown in Figure 4.8. We observed that the relation between the standard deviation and the autocorrelation time had a -0.68 slope on a log-log plot, where a slope of -2/3 is the theoretical prediction [94].

The size-dependence of the emission spectra of individual PQDs can be modeled by solving the Schrödinger equation under the effective mass approximation [130]. While spherical particles with infinite barriers allow analytical calculations [130], here we also use numerical calculations which allow for cubic particles and finite barrier energies [131].

4.2.3 Bandgap and Emission Energy as a function of Single PQD Size

We assessed the quantum confinement using an effective mass Schrödinger equation model using a Matlab-based finite-element approach, as shown in Figure 4.9 and considering the exciton binding under a weak confinement assumption [132]. The simulations used $m_e^* = 0.134m_0$ and $m_h^* = 0.128m_0$ [132], with a bulk bandgap of 2.30 eV for cubic $CsPbBr_3$ [6], $\epsilon_{QD} = 4.8$ [132]. The barrier height was chosen to either be infinite or to match the band offset between $CsPbBr_3$ QDs and oleic acid ligands (3.14 eV for electrons and 0.79 eV for holes) [133]. The dispersion found for this model was less than that seen in the experiment but it did match with previous works [132, 2]. As we can see here, it has a good agreement with the quantum confinement that we introduced in Chapter 2.

4.2.4 Summary

As we presented in this section, we can use an common optical tweezers setup with DNHs apertures for sizing and spectroscopically characterizing individual dots in solution. It is relevant for quantum applications where we seek to obtain multi-

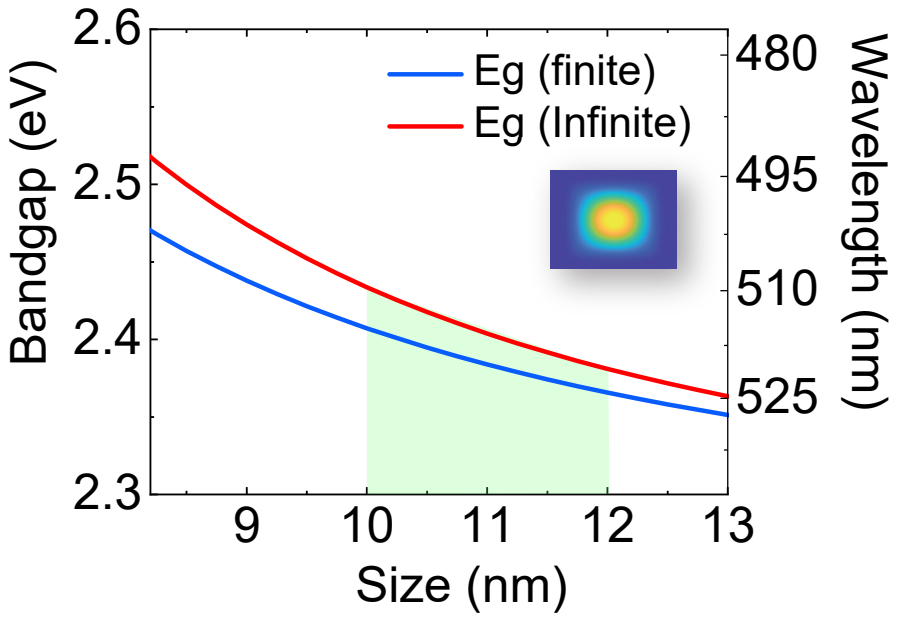

Figure 4.9: Calculations of size effect for 2 separate cases: Cubic well with infinite and finite barriers. Green highlights the approximate size range observed experimentally. Inset shows the wavefunction distribution for the finite case.

ple indistinguishable emitters [38] and develop high-performance perovskite solar cells with uniformly sized of quantum dots. The method can also be used in-situ to optimize solution-based growth without using any external high-resolution devices [134, 22, 21, 26, 25].

4.3 Two Quantum Dot Assembly via Trapping

4.3.1 Forster Coupling Observed by Two PQDs

The trapping setup allowed us to measure and characterize the quantum coupling between two PQDs assembled in real-time and isolated in the trap. We observed two steps corresponding to double PQDs trapped subsequently in the same aperture as shown in Figure4.10a. It has been shown in past works on aperture optical tweezers that the co-trapping of two nanoparticles results in a double step profile [80].

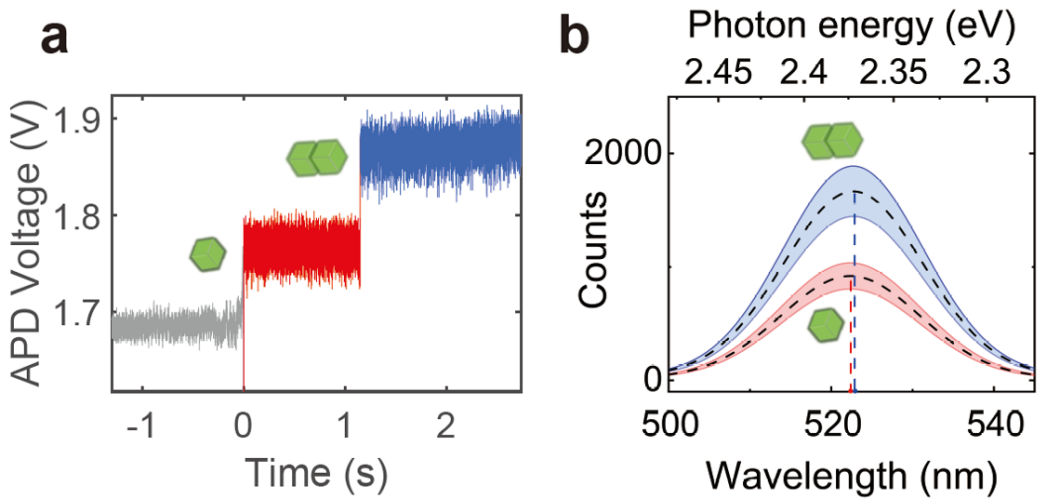

Figure 4.10: (a) Double trapping event collected by APD (first trapping: red; second trapping: blue). (b) Spectra of single dot trapping and double dot trapping are shown in red and blue. The areas filled with blue and red stand for the experiment data (fitted) at each sampling time. Black dotted lines indicate the average of the varying spectra region (quantum blinking).

Figure 4.10b shows the observed distribution of emission for single and double PQD trapping averaged over 30 different DNHs, averaging over at least 6 measurements at each DNH (full data is included in the appendix, Figure A1). Figure. 4.10b, shows that the emission intensity approximately doubled when there are two PQDs. Also, there was a systematic spectral red-shift of the emission. Figure 4.11 quantifies the systematic red-shift in the emission observed for the multiple double-dot trapping events. It is relevant to note that there was always a redshift: if the energy was simply transferred from the smaller dot to the larger one (as is the case for past works on RET [40]), we would expect on average a redshift sometimes and

no shift at other times, depending on whether a smaller or a larger dot was trapped first.

Before discussing the physical mechanism that may be responsible for this redshift, let us describe a simple generic model for the energy shift arising from a generalized coupling potential V. These interactions can be represented by interaction energy that shifts the energy of the individual PQDs. Considering two oscillators with energies E_1 and E_2, as displayed in eq 4.1, the shift from E_1 upon coupling can be calculated as [135, 39]:

$$\begin{bmatrix} E_1 & V \\ V & E_2 \end{bmatrix} \tag{4.1}$$

$$\Delta = \frac{1}{2}\left[(E_2 - E_1) - \sqrt{(E_1 + E_2)^2 - 4(E_1 E_2 - V^2)}\right]. \tag{4.2}$$

The emission spectrum will decrease on the high-energy side because this interaction always produces a lower energy level. The energy only transfers from the smaller PQD to the larger one. Fitting Δ to the observed shift, we find a best fit for $V = 1.1$ meV in eq 4.2, as shown in Figure 4.11. Figure 4.12 a and b shows the photoluminescence energy distributions of trapping single and double dots. The standard deviation of each case is around 4.1 and 3.6 meV.

4.3.2 Simulation for Double QDs

With the barrier widths seen in TEM imaging (similar to the oleic acid ligand length of ∼2 nm) and the barrier heights used above for single dots [133], we do not expect significant wavefunction overlap between two adjacent dots. To confirm this, we used effective mass the Schrödinger model as above (neglecting the Coulomb potential) and confirmed that there was minimal delocalization for separations greater than about 1 nm, as is shown in Figure 4.13.

4.3.3 Optical Binding

By using the Rayleigh theory in Eq. 4.3 for the scattering cross section [136], the polarizability constant (α_p) of the scatterer can be calculated from the scattering cross section:

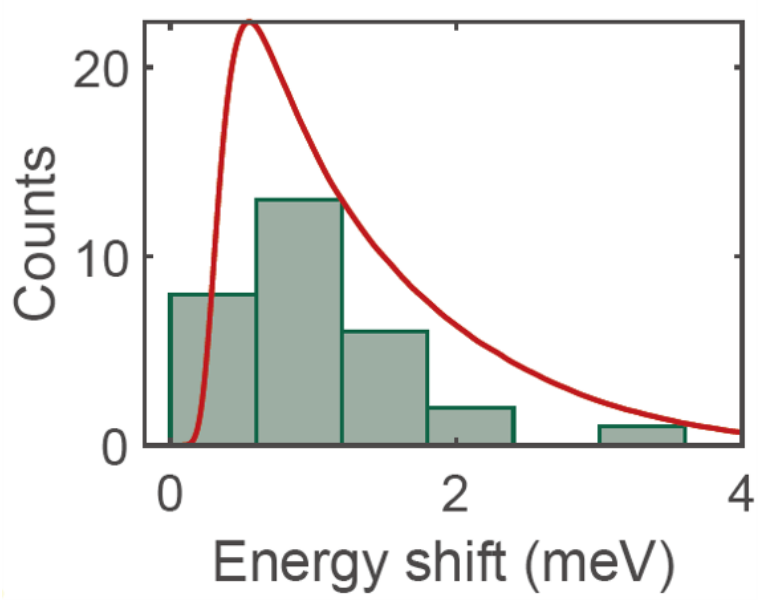

Figure 4.11: Experimental (green bars) and simulated (red curve) energy shift upon coupling. Experimental values were observed among 30 different DNHs, each measured at least 6 times, and the simulation represents the energy shift by Förster interaction between two dots randomly selected from 1000 dots (normal distribution).

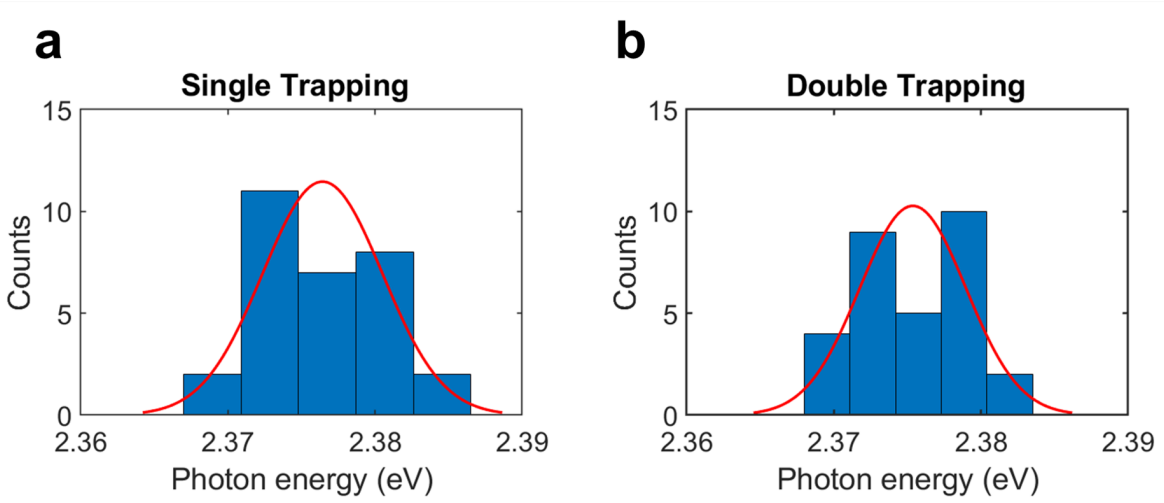

Figure 4.12: The PL energy distribution of trapping (a) single dot and (b) double dots.

$$x_{scat} = \frac{8\pi}{3}\frac{(2\pi)^4}{\lambda^4}\alpha_p^2 \tag{4.3}$$

The trapping potential energy in the dipole limit can be given by[91]:

$$U_{trap} = -\frac{1}{2}\vec{p}\cdot\vec{E} \tag{4.4}$$

where $\vec{p}$ is the dipole moment and $\vec{E}$ is the electric field. The optical potential energy should be greater than the thermal energy to keep trapping the particle.

Here, we use the finite-difference time domain simulation software (Lumerical FDTD ver. 2020 R2.3). The simulations calculated the trapping potential energy of the single and double PQDs (dielectric cubes, $\epsilon = 4.8$). Fig. 4.14 shows the potential energy as a function of the distance between two PQDs. The electric fields with 1 nm - 4 nm are shown in inset figures. This shows that the dots are attracted to one another through the optical field in the dipole limit.

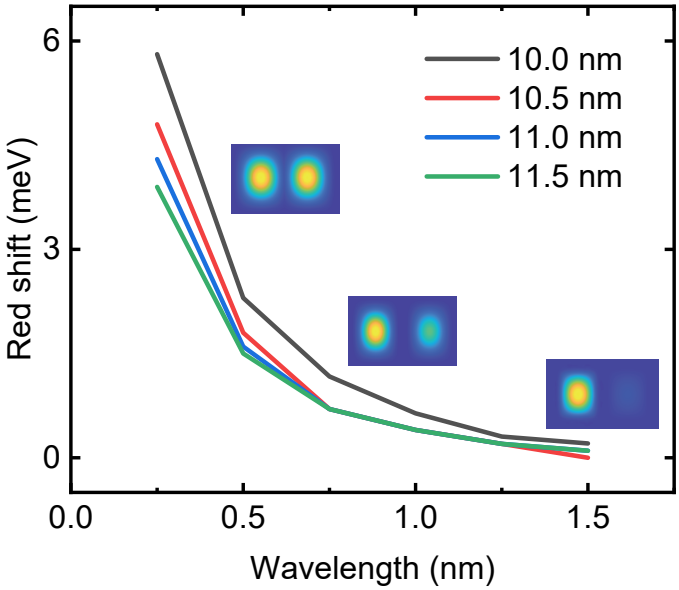

Figure 4.13: Calculation of energy shift against of the distance. Inset shows the wavefunction distribution for the cubic case in different separations.

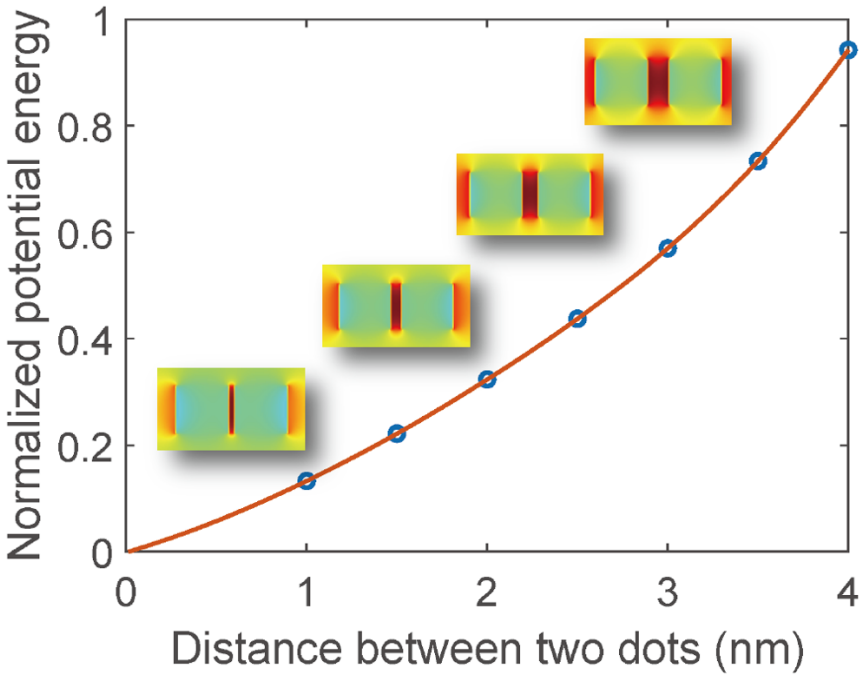

Figure 4.14: FDTD simulation results of the trapping potential energy against the distance between two dots. Inset figures show the visualization of the electric field intensity of the double dots with various distances.

4.4 Coupling Mechanisms between Two Quantum Dots

(This part is mainly contributed by Juanjuan Ren and Stephen Hughes in the published paper [41])

We now discuss a possible physical mechanism underlying the observed systematic spectral red-shift. First, we discuss the expected photon coupling between two PQDs, treated as point dipoles. As shown in the appendix, the *radiative* decay rate from a single dipole emitter is

$$\Gamma_1(\mathbf{r}_1) = \frac{2\mathbf{d}_1 \cdot \mathrm{Im}\{\mathbf{G}(\mathbf{r}_1, \mathbf{r}_1, \omega)\} \cdot \mathbf{d}_1}{\epsilon_0 \hbar}, \tag{4.5}$$

for a dipole moment $\mathbf{d}_1$ (assumed real) at position $\mathbf{r}_1$, and $\mathbf{G}$ is the photon Green function, for any generalized medium. For coupled dipoles (the second one is with real dipole moment $\mathbf{d}_2$ at $\mathbf{r}_2$), the photon exchange has real and imaginary parts, defined through the incoherent rates of photon transfer:

$$\Gamma_{12} = \frac{2\mathbf{d}_1 \cdot \mathrm{Im}\{\mathbf{G}(\mathbf{r}_1, \mathbf{r}_2, \omega)\} \cdot \mathbf{d}_2}{\epsilon_0 \hbar}, \tag{4.6}$$

and a coherent exchange term

$$\Delta_{12} = -\frac{\mathbf{d}_1 \cdot \mathrm{Re}\{\mathbf{G}(\mathbf{r}_1, \mathbf{r}_2, \omega)\} \cdot \mathbf{d}_2}{\epsilon_0 \hbar}. \tag{4.7}$$

The latter gives rise to spectral frequency shifts through photon exchange.

When one considers a homogeneous medium (with $\epsilon_b = n_b^2$ using two dipoles spatially separated by r_{12} (center to center), and in the near-field regime, then the coherent exchange term, with s-polarized dipoles, is

$$\hbar\Delta_{12}^{ss} = \frac{d^2}{4\pi\epsilon_0\epsilon_b r_{12}^3} \approx 93\,\hbar\Gamma_1 = 0.25 \text{ meV}, \tag{4.8}$$

while for p-polarized dipoles,

$$\hbar\Delta_{12}^{pp} = -\frac{d^2}{2\pi\epsilon_0\epsilon_b r_{12}^3} \approx -186\,\hbar\Gamma_1 = -0.50 \text{ meV}. \tag{4.9}$$

We have used $d = 0.72\,\mathrm{e}\cdot\mathrm{nm}$ and $\epsilon_b = 1.5^2$, yielding a nominal radiative decay rate of $\hbar\Gamma_1 \approx 2.69$ μeV (corresponding lifetime of 250 ps); this estimate scales with $\Gamma_{1,2}$ so could easily be larger. Note that these analytical rates identically recover the

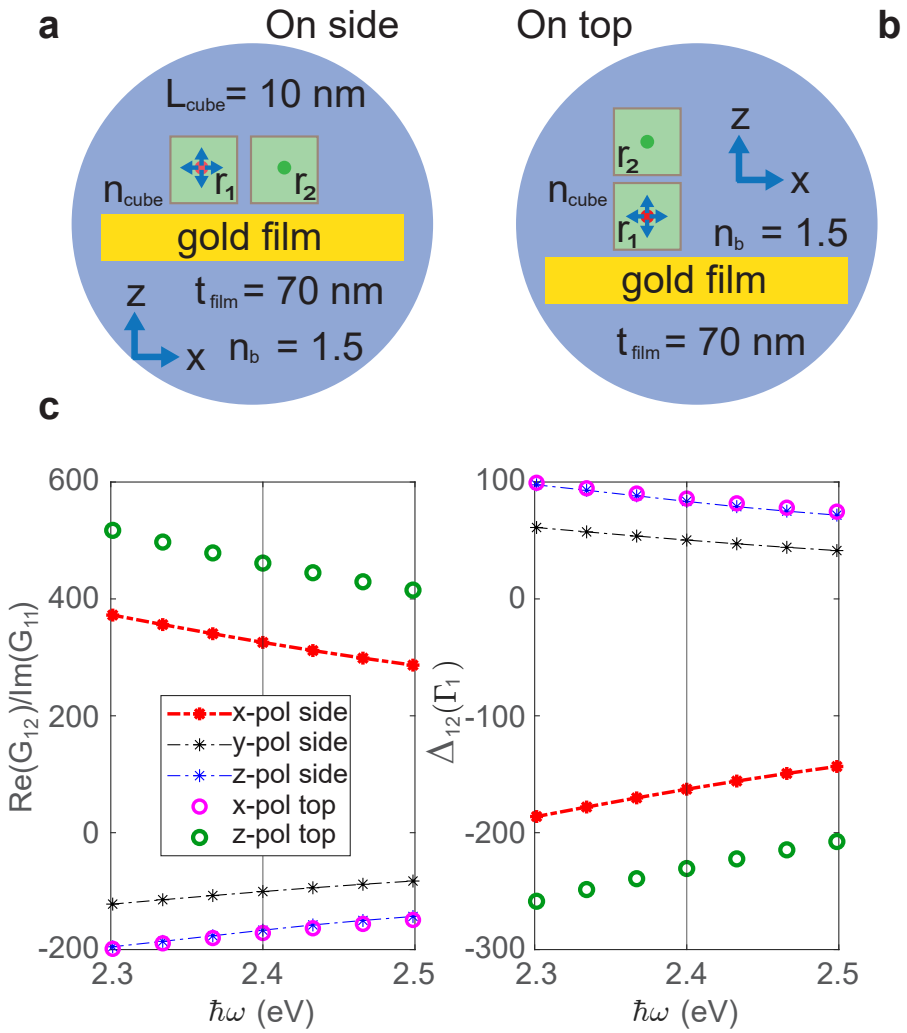

Figure 4.15: Schematic diagram for PQD dimer with (a) side coupling (left) or (b) top coupling (right). PQDs are shown in green in the two figures. (c) Example calculations for the propagators and dipole-dipole shifts computed from COMSOL, which includes the full scattering geometry. We show different dipole polarization, and dipole-dipole coupling for PQD cubes that are horizontally stacked or vertically, and separated by 1-nm. All terms include local field corrections, so are normalized by the result including the single PQD cube.

well-known Förster coupling terms, and can be described semi-classically or quantum mechanically. Below, we will introduce the shorthand notation $\mathbf{G}_{12} = \mathbf{G}(\mathbf{r}_1, \mathbf{r}_2)$ and $\mathbf{G}_{11} = \mathbf{G}(\mathbf{r}_1, \mathbf{r}_1)$. For identical dipole emitters, the resonance will split by $\pm\hbar\Delta_{12} \equiv \pm V_F \propto \mathrm{Re}G_{12}$, into subradiant and superradiant states, where the latter is optically bright. ($V = V_F$ for RET). Based on particle size variation giving a variation in the centre-to-centre separations, as well as expected dipole moment variation (smaller dots have smaller dipole moments [132]), we expect the variation in V_F to be within 50% of the reported value.

In the Appendix section 2, we describe how these radiative decay and exchange rates are influenced by local field corrections and interactions with the metal film, from both an analytical perspective as well as using full numerical simulations in COMSOL. As an example of the latter calculations, here we consider two PQD cubes above a gold film, either horizontally coupled or vertically coupled, as shown in Figure. 4.15a and b. The PQD cubes are separated by 1-nm (gap size), and various dipole polarizations are considered. The corresponding Green function propagators and dipole-dipole coupling rates (in units of the radiative decay rate) are shown in Figure. 4.15c. Overall we predict that maximum photon exchange rates of around $-231\Gamma_1$ are possible, which we estimate to be around 0.62 meV (for z-polarized dipoles).

After initial calculations at a 1 nm gap size, we obtained a more accurate measurement of the gap size from high-resolution TEM as being 1.4 nm. This has a small (10%) impact on the theoretical values (Fig. S12). The typical gap for oleic acid PQDs in TEM imaging is between 1 and 2 nm [122, 2, 38, 127, 137]. The optical force tends to squeeze the particles together and minimize the gap size in solution, and so we expect this is similar to what was observed by HR-TEM.

It is also important to note that the expected exciton Bohr radius is much smaller than the size of the PQDs, which give rise to a giant oscillator strength for an optical transition [132, 138]. This is caused by a correlated exciton wave function that affects both the radiative decay and the dipole-dipole coupling rates. We discuss and estimate this enhancement in the Appendix section 2, which we expect to be about a factor of 5 bigger than PQDs in the strong confinement regime. This is significant, even in the presence of local field reductions.

4.4.1 Other potential sources and mechanisms for coupled-PQD frequency shifts

Next, we briefly discuss some other potential effects that could cause large frequency shifts for coupled PQDs.

For quantum emitters that are very close together, namely, where electronic tunneling is possible, excitons can be transferred, which is typically termed Dexter energy transfer [139]. This process is usually negligible for distances greater than 1 nm. Dexter is a non-radiative process with electron exchange. Although similar to Förster energy transfer, it differs greatly in length scale and the underlying mechanism. Dexter transfer can be singlet-singlet or triplet-triplet, and the three fundamental excitations in lead PQDs are triplets [132]. Dexter energy transfer is a process where the donor and the acceptor exchange their electron. Thus, the exchanged electrons should occupy the orbital of the other pair. The Dexter transfer rate has the form $V_D \propto J \exp(-2r_{12}/L_v)$, where J is the normalized spectral overlap, and L_v is the the sum of van der Waals radius. Dexter transitions couple bright excitons to bright excitons and are spin preserving. Their strength can also be computed from the Coulomb matrix element. However, since Dexter coupling requires an overlap with the electronic wave functions, we believe it is highly unlikely for our coupled QDs.

There are also potential monopole-monopole interactions, which do not depend on any spatial overlap of the electronic wave functions. These are usually neglected in the derivation of Förster coupling between quantum emitters. Actually, monopole-monopole is also the origin of Dexter energy transfer, but in that case, the contribution also requires orbital overlap. In the linear excitation domain (e.g., neglecting biexciton effects), the excitonic monopole-monopole term [140, 141] merely renormalizes the eigenergies, unlike Förster and Dexter terms that represent the exchange of photons or electronic excitations. Furthermore, for a symmetric wavefunction, monopole-monopole shifts should be zero for linear excitation.

There could also be effects beyond a dipole approximation, which can be captured by doing a spatial integration with respect to the inter-PQD exciton wave functions and the photon Green function propagator [142]. We have carried out such a calculation using 6D Monte Carlo integration and found the dipole approximation to be excellent, within 5% for QD cubes that have a gap separation of 1 nm. This calculation used the ground state exciton wave function and we used a similar integration technique to compute C, which enhances the oscillator strength.

Finally, we mention tandem tunneling [143] that can occur through the intermediate state in which the electron and hole are in different PQDs. This process has been shown to have exciton hopping rates that are larger than the Dexter rate Förster for certain PQDs. However, such PQDs are clearly fused together (unlike our optically trapped coupled PQDs), so we also rule out the effect of fused tunneling.

4.5 Summary

4.5.1 In-Situ Size-Spectral Characterization by using DNHs Optical Tweezer

In the present work, we have demonstrated the use of an optical tweezer platform to characterize multiple individual PQDs in solution. In past works, the standard approach for monitoring PQD synthesis has been to follow up PQD growth with characterization via TEM or luminescence studies. Here we show that we can accurately determine the size and the spectral response without the need for TEM. This may allow for fine-tuning or improving growth conditions in-situ. For example, it is possible to envision integrating the present trapping setup with a flow-cell [126] for real-time monitoring and/or modifying of growth conditions [134].

4.5.2 Double Quantum Dots Coupling

In this thesis, we propose that RET is the dominant coupling mechanism between the two PQDs. Other mechanisms might not enough to explain the results we observed during the experiment, like Dexter coupling and quantum hybridization. Because the barrier height is too large and the gap too wide to allow substantial tunneling [144]. RET has been observed in ensembles of dissimilar PQDs [40]; however, that exchange is uni-directional (from the higher energy to the lower energy PQD). Here, since the dots are nominally the same size, the exchange is bidirectional. For quantum applications, RET has been proposed theoretically as a mechanism to achieve quantum computing via colloidal quantum dots [39]. Here we estimate the magnitude of the RET induced shift. The dipole moment is estimated from previously reported values of the emission lifetime. We further note that the PQDs studied here are large relative to the exciton Bohr radius, and are in the intermediate to weak confinement regime. This enhances the strength of the RET interaction by 5 times with respect

to strongly confined dots, which is a particularly relevant finding of this work.

We estimate from a dipole model that the shift is at least two orders of magnitude larger than the radiative lifetime. We have also looked at distributed wavefunctions (beyond the local dipole model), and full COMSOL simulations including the metal surface nearby in aperture, and these only provide small corrections to the value reported above. Since this value is comparable to what we observed in the experiments, RET is a plausible explanation for the observed shift.

Chapter 5

Conclusion and Future Works

5.1 Conclusion

In this thesis, we reviewed the knowledge of PQDs and the theoretical background of optical tweezers (Chapter 2). Then we introduce nanoplasmonics tweezers with the DNH apertures, data analysing method (e.g. autocorrelation function and FDTD simulation) we used in the work (Chapter 2). We also reviewed several types of the coupling relationship between nanoparticles (Chapter 2).

In Chapter 3, we introduced the experiment methods, which include PQD solution synthesis/preparation method, DNH gold sample preparation, fabricating trapping experiment sample with solutions and the details of trapping experiment. A common trapping experiment workflow was summarized in the last section.

In Chapter 4, we demonstrated the ability to characterize the size and coupling between individual and dimer PQDs in solution, and simultaneously observe their emission spectra using our DNH tweezers. This is a powerful tool to explore and quantify sample heterogeneity in size and emission in solution, without requiring expensive and damaging techniques. The approach may be extended to isolate identical dots (both in terms of size and spectral emission), which is a pathway to achieving indistinguishable quantum emitters. We quantified the systematic red-shift for coupled PQDs in solution of 1.1 $\pm$ 0.6 meV and we argue that this is likely the result of resonant energy transfer. We also discuss and rule out several other possible coupling mechanisms including Dexter coupling, electronic tunneling, exciton tunneling for fused dots, and possible monopole-monopole interactions. The magnitude of the RET is usually large when compared with the strongly confined quantum dots that

have been explored in the past, which is intriguing because RET has been proposed as a mechanism to obtain entanglement for quantum information processing applications [39].

5.2 Future Works

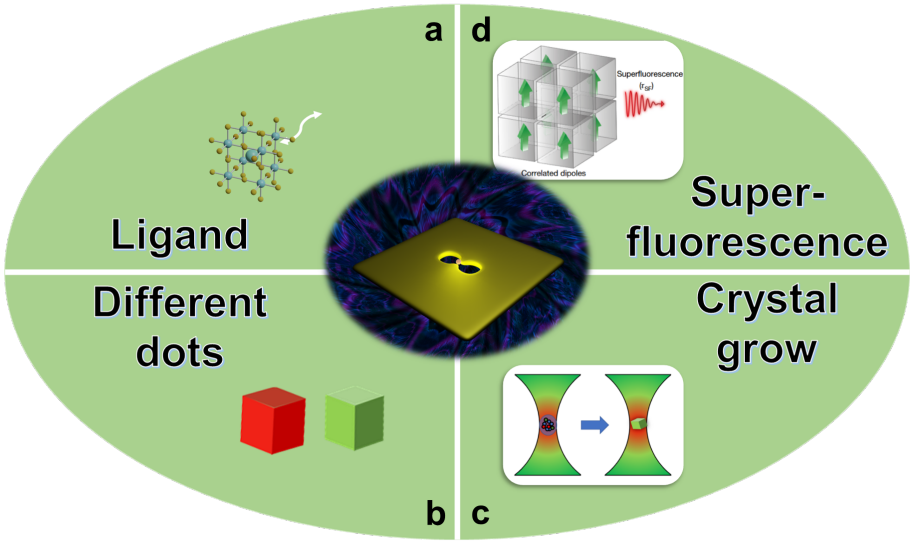

Figure 5.1: Future works that can be implemented by using DNHs optical tweezers: (a) using different ligands with different lengths; (b) capture different two quantum dots (e.g. $CsPbBr_3$ and $CsPbI_3$); (c) monitor crystal growth; (d) observe Dicke superfluorescence by using optical tweezers.

In the future, we aim to consider the impact of temperature on the observed spectral shifts, which will require adding cyrogenic capability to our setup so that the temperature can be lowered after trapping is achieved. To first order, RET does not depend on temperature [145, 146], however, more advanced electron-phonon theories predict a renormalization of V_F as a function of temperature [147, 148]. We present only a simple temperature independent model here, as a first order quantification of the RET effect. We also plan to modify the ligands' length and the dot size to investigate their impact on the RET, since there is a strong size-dependence of this effect, as shown in Figure 5.1a. It may also be possible to modify the setup to allow for cryogenic cooling and observe superfluorescence (Figure 5.1b) after trapping is achieved, and for time-resolved ultra-fast probing of two different trapped dots (Figure 5.1c). Combined, these advances will allow for further exploration of the

coupling between these quantum emitters. The approach may also be extended to monitor and modify growth in real time (Figure 5.1d). DNH optical tweezers offer an interesting platform for studying regimes of coupling for small assemblies of 2 or more PQDs (however larger apertures would be preferred for multiple dots). In this manner, it may be possible explore the full range of interactions from the single dot, coupled dots, several dots, to large cluster superfluorescence ensemble measurements [122]; thereby transitioning from the nanoscopic to mesoscopic regimes.

Bibliography

[1] Hung-Chia Wang, Zhen Bao, Hsin-Yu Tsai, An-Cih Tang, and Ru-Shi Liu. Perovskite quantum dots and their application in light-emitting diodes. *Small*, 14(1):1702433, 2018.

[2] Loredana Protesescu, Sergii Yakunin, Maryna I. Bodnarchuk, Franziska Krieg, Riccarda Caputo, Christopher H. Hendon, Ruo Xi Yang, Aron Walsh, and Maksym V. Kovalenko. Nanocrystals of cesium lead halide perovskites (CsPbX3, x = cl, br, and i): Novel optoelectronic materials showing bright emission with wide color gamut. *Nano Letters*, 15(6):3692–3696, February 2015.

[3] CHR MØller. Crystal structure and photoconductivity of caesium plumbohalides. *Nature*, 182(4647):1436–1436, 1958.

[4] Chun Yong Ngo, Soon Fatt Yoon, Weijun J Fan, and Soo Jin Chua. Effects of size and shape on electronic states of quantum dots. *Physical Review B*, 74(24):245331, 2006.

[5] Fangze Liu, Siraj Sidhik, Mark A. Hoffbauer, Sina Lewis, Amanda J. Neukirch, Vitaly Pavlenko, Hsinhan Tsai, Wanyi Nie, Jacky Even, Sergei Tretiak, Pulickel M. Ajayan, Mercouri G. Kanatzidis, Jared J. Crochet, Nathan A. Moody, Jean-Christophe Blancon, and Aditya D. Mohite. Highly efficient photoelectric effect in halide perovskites for regenerative electron sources. *Nature Communications*, 12(1), January 2021.

[6] Mohammed Ezzeldien, Samah Al-Qaisi, Z. A. Alrowaili, Meshal Alzaid, E. Maskar, A. Es-Smairi, Tuan V. Vu, and D. P. Rai. Electronic and optical properties of bulk and surface of CsPbBr3 inorganic halide perovskite a first principles DFT 1/2 approach. *Scientific Reports*, 11(1), October 2021.

[7] Quanbo Jiang, Prithu Roy, Jean-Benoît Claude, and Jérôme Wenger. Single photon source from a nanoantenna-trapped single quantum dot. *Nano Letters*, 21(16):7030–7036, 2021.

[8] Deying Luo, Rui Su, Wei Zhang, Qihuang Gong, and Rui Zhu. Minimizing non-radiative recombination losses in perovskite solar cells. *Nature Reviews Materials*, 5(1):44–60, 2020.

[9] Weibo Yan, Yunlong Li, Yu Li, Senyun Ye, Zhiwei Liu, Shufeng Wang, Zuqiang Bian, and Chunhui Huang. High-performance hybrid perovskite solar cells with open circuit voltage dependence on hole-transporting materials. *Nano Energy*, 16:428–437, 2015.

[10] Martin A Green, Anita Ho-Baillie, and Henry J Snaith. The emergence of perovskite solar cells. *Nature Photonics*, 8(7):506–514, 2014.

[11] Jens Koch, M Yu Terri, Jay Gambetta, Andrew A Houck, David Isaac Schuster, Johannes Majer, Alexandre Blais, Michel H Devoret, Steven M Girvin, and Robert J Schoelkopf. Charge-insensitive qubit design derived from the cooper pair box. *Physical Review A*, 76(4):042319, 2007.

[12] Hanhee Paik, David I Schuster, Lev S Bishop, Gerhard Kirchmair, Gianluigi Catelani, Adam P Sears, BR Johnson, MJ Reagor, Luigi Frunzio, Leonid I Glazman, et al. Observation of high coherence in josephson junction qubits measured in a three-dimensional circuit qed architecture. *Physical Review Letters*, 107(24):240501, 2011.

[13] Vincent Bouchiat, D Vion, Ph Joyez, D Esteve, and MH Devoret. Quantum coherence with a single cooper pair. *Physica Scripta*, 1998(T76):165, 1998.

[14] Boris B Blinov, Dietrich Leibfried, C Monroe, and David J Wineland. Quantum computing with trapped ion hyperfine qubits. *Quantum Information Processing*, 3(1):45–59, 2004.

[15] David Kielpinski, Chris Monroe, and David J Wineland. Architecture for a large-scale ion-trap quantum computer. *Nature*, 417(6890):709–711, 2002.

[16] David P DiVincenzo. Double quantum dot as a quantum bit. *Science*, 309(5744):2173–2174, 2005.

[17] Daniel Loss and David P DiVincenzo. Quantum computation with quantum dots. *Physical Review A*, 57(1):120, 1998.

[18] Xuedong Hu and S Das Sarma. Hilbert-space structure of a solid-state quantum computer: Two-electron states of a double-quantum-dot artificial molecule. *Physical Review A*, 61(6):062301, 2000.

[19] Mark A Eriksson, Mark Friesen, Susan N Coppersmith, Robert Joynt, Levente J Klein, Keith Slinker, Charles Tahan, PM Mooney, JO Chu, and SJ Koester. Spin-based quantum dot quantum computing in silicon. *Quantum Information Processing*, 3(1):133–146, 2004.

[20] Guido Burkard, Daniel Loss, and David P DiVincenzo. Coupled quantum dots as quantum gates. *Physical Review B*, 59(3):2070, 1999.

[21] Oscar Hsu-Cheng Cheng, Tian Qiao, Matthew Sheldon, and Dong Hee Son. Size-and temperature-dependent photoluminescence spectra of strongly confined cspbbr 3 quantum dots. *Nanoscale*, 12(24):13113–13118, 2020.

[22] Qian Zhao, Abhijit Hazarika, Laura T Schelhas, Jun Liu, E Ashley Gaulding, Guoran Li, Minghui Zhang, Michael F Toney, Peter C Sercel, and Joseph M Luther. Size-dependent lattice structure and confinement properties in cspbi3 perovskite nanocrystals: negative surface energy for stabilization. *ACS Energy Letters*, 5(1):238–247, 2019.

[23] Elizabeth M Tennyson, Bart Roose, Joseph L Garrett, Chen Gong, Jeremy N Munday, Antonio Abate, and Marina S Leite. Cesium-incorporated triple cation perovskites deliver fully reversible and stable nanoscale voltage response. *ACS Nano*, 13(2):1538–1546, 2018.

[24] Weibo Yan, Yu Li, Senyun Ye, Yunlong Li, Haixia Rao, Zhiwei Liu, Shufeng Wang, Zuqiang Bian, and Chunhui Huang. Increasing open circuit voltage by adjusting work function of hole-transporting materials in perovskite solar cells. *Nano Research*, 9(6):1600–1608, 2016.

[25] Alasdair AM Brown, Parth Vashishtha, Thomas JN Hooper, Yan Fong Ng, Gautam V Nutan, Yanan Fang, David Giovanni, Ju Nie Tey, Liudi Jiang, Bahulayan Damodaran, et al. Precise control of cspbbr3 perovskite nanocrystal growth at

room temperature: Size tunability and synthetic insights. *Chemistry of Materials*, 33(7):2387–2397, 2021.

[26] Tiarnan AS Doherty, Andrew J Winchester, Stuart Macpherson, Duncan N Johnstone, Vivek Pareek, Elizabeth M Tennyson, Sofiia Kosar, Felix U Kosasih, Miguel Anaya, Mojtaba Abdi-Jalebi, et al. Performance-limiting nanoscale trap clusters at grain junctions in halide perovskites. *Nature*, 580(7803):360–366, 2020.

[27] Sohini Bhattacharyya, Darsi Rambabu, and Tapas Kumar Maji. Mechanochemical synthesis of a processable halide perovskite quantum dot–mof composite by post-synthetic metalation. *Journal of Materials Chemistry A*, 7(37):21106–21111, 2019.

[28] Seyeong Lim, Gyudong Lee, Sanghun Han, Jigeon Kim, Sunhee Yun, Jongchul Lim, Yong-Jin Pu, Min Jae Ko, Taiho Park, Jongmin Choi, et al. Monodisperse perovskite colloidal quantum dots enable high-efficiency photovoltaics. *ACS Energy Letters*, 6:2229–2237, 2021.

[29] Charles Santori, David Fattal, Jelena Vučković, Glenn S Solomon, and Yoshihisa Yamamoto. Indistinguishable photons from a single-photon device. *nature*, 419(6907):594–597, 2002.

[30] Manuel Gschrey, Alexander Thoma, Peter Schnauber, Mark Seifried, Ronny Schmidt, Benjamin Wohlfeil, Luzy Krüger, J-H Schulze, Tobias Heindel, Sven Burger, et al. Highly indistinguishable photons from deterministic quantum-dot microlenses utilizing three-dimensional in situ electron-beam lithography. *Nature Communications*, 6(1):1–8, 2015.

[31] Yunhua Chen, Sara R Smock, Anne H Flintgruber, Frédéric A Perras, Richard L Brutchey, and Aaron J Rossini. Surface termination of cspbbr3 perovskite quantum dots determined by solid-state nmr spectroscopy. *Journal of the American Chemical Society*, 142(13):6117–6127, 2020.

[32] Moses Kodur, Rishi E Kumar, Yanqi Luo, Deniz N Cakan, Xueying Li, Michael Stuckelberger, and David P Fenning. X-ray microscopy of halide perovskites: Techniques, applications, and prospects. *Advanced Energy Materials*, 10(26):1903170, 2020.

[33] Junsheng Chen, Dongzhou Liu, Mohammed J Al-Marri, Lauri Nuuttila, Heli Lehtivuori, and Kaibo Zheng. Photo-stability of cspbbr 3 perovskite quantum dots for optoelectronic application. *Science China Materials*, 59(9):719–727, 2016.

[34] UF Keyser, J Van der Does, C Dekker, and NH Dekker. Optical tweezers for force measurements on dna in nanopores. *Review of Scientific Instruments*, 77(10):105105, 2006.

[35] Yuanjie Pang and Reuven Gordon. Optical trapping of 12 nm dielectric spheres using double-nanoholes in a gold film. *Nano Letters*, 11(9):3763–3767, 2011.

[36] Jamal M Ehtaiba and Reuven Gordon. Template-stripped nanoaperture tweezer integrated with optical fiber. *Optics Express*, 26(8):9607–9613, 2018.

[37] Ryan M Gelfand, Skylar Wheaton, and Reuven Gordon. Cleaved fiber optic double nanohole optical tweezers for trapping nanoparticles. *Optics Letters*, 39(22):6415–6417, 2014.

[38] Hendrik Utzat, Weiwei Sun, Alexander EK Kaplan, Franziska Krieg, Matthias Ginterseder, Boris Spokoyny, Nathan D Klein, Katherine E Shulenberger, Collin F Perkinson, Maksym V Kovalenko, et al. Coherent single-photon emission from colloidal lead halide perovskite quantum dots. *Science*, 363(6431):1068–1072, 2019.

[39] Dulanjan Harankahage, James Cassidy, Mingrui Yang, Dmitry Porotnikov, Maia Williams, Natalia Kholmicheva, and Mikhail Zamkov. Quantum computing with exciton qubits in colloidal semiconductor nanocrystals. *The Journal of Physical Chemistry C*, 125(40):22195–22203, 2021.

[40] Chris de Weerd, Leyre Gomez, Hong Zhang, Wybren J Buma, Georgian Nedelcu, Maksym V Kovalenko, and Tom Gregorkiewicz. Energy transfer between inorganic perovskite nanocrystals. *The Journal of Physical Chemistry C*, 120(24):13310–13315, 2016.

[41] Hao Zhang, Parinaz Moazzezi, Juanjuan Ren, Brett Henderson, Cristina Cordoba, Vishal Yeddu, Arthur M. Blackburn, Makhsud I. Saidaminov, Irina Paci, Stephen Hughes, and Reuven Gordon. Coupling perovskite quantum dot pairs

in solution using a nanoplasmonic assembly. *Nano Letters*, 22(13):5287–5293, 2022. PMID: 35767329.

[42] Eugene A Katz. Perovskite: name puzzle and german-russian odyssey of discovery. *Helvetica Chimica Acta*, 103(6):e2000061, 2020.

[43] Yanjun Fang, Qingfeng Dong, Yuchuan Shao, Yongbo Yuan, and Jinsong Huang. Highly narrowband perovskite single-crystal photodetectors enabled by surface-charge recombination. *Nature Photonics*, 9(10):679–686, 2015.

[44] Yue Wang, Xiaoming Li, Jizhong Song, Lian Xiao, Haibo Zeng, and Handong Sun. All-inorganic colloidal perovskite quantum dots: a new class of lasing materials with favorable characteristics. *Advanced Materials*, 27(44):7101–7108, 2015.

[45] Sergii Yakunin, Loredana Protesescu, Franziska Krieg, Maryna I Bodnarchuk, Georgian Nedelcu, Markus Humer, Gabriele De Luca, Manfred Fiebig, Wolfgang Heiss, and Maksym V Kovalenko. Low-threshold amplified spontaneous emission and lasing from colloidal nanocrystals of caesium lead halide perovskites. *Nature Communications*, 6(1):1–9, 2015.

[46] Xiaoming Li, Ye Wu, Shengli Zhang, Bo Cai, Yu Gu, Jizhong Song, and Haibo Zeng. Cspbx3 quantum dots for lighting and displays: room-temperature synthesis, photoluminescence superiorities, underlying origins and white light-emitting diodes. *Advanced Functional Materials*, 26(15):2435–2445, 2016.

[47] Shibin Sun, Dan Yuan, Yuan Xu, Aifei Wang, and Zhengtao Deng. Ligand-mediated synthesis of shape-controlled cesium lead halide perovskite nanocrystals via reprecipitation process at room temperature. *ACS Nano*, 10(3):3648–3657, 2016.

[48] Song Wei, Yanchun Yang, Xiaojiao Kang, Lan Wang, Lijian Huang, and Daocheng Pan. Room-temperature and gram-scale synthesis of cspbx 3 (x= cl, br, i) perovskite nanocrystals with 50–85% photoluminescence quantum yields. *Chemical Communications*, 52(45):7265–7268, 2016.

[49] Ioannis Lignos, Stavros Stavrakis, Georgian Nedelcu, Loredana Protesescu, Andrew J deMello, and Maksym V Kovalenko. Synthesis of cesium lead halide per-

ovskite nanocrystals in a droplet-based microfluidic platform: fast parametric space mapping. *Nano Letters*, 16(3):1869–1877, 2016.

[50] Tom C Jellicoe, Johannes M Richter, Hugh FJ Glass, Maxim Tabachnyk, Ryan Brady, Siân E Dutton, Akshay Rao, Richard H Friend, Dan Credgington, Neil C Greenham, et al. Synthesis and optical properties of lead-free cesium tin halide perovskite nanocrystals. *Journal of the American Chemical Society*, 138(9):2941–2944, 2016.

[51] Aifei Wang, Xingxu Yan, Mian Zhang, Shibin Sun, Ming Yang, Wei Shen, Xiaoqing Pan, Peng Wang, and Zhengtao Deng. Controlled synthesis of lead-free and stable perovskite derivative cs2sni6 nanocrystals via a facile hot-injection process. *Chemistry of Materials*, 28(22):8132–8140, 2016.

[52] Xiaoli Zhang, Wanyu Cao, Weigao Wang, Bing Xu, Sheng Liu, Haitao Dai, Shuming Chen, Kai Wang, and Xiao Wei Sun. Efficient light-emitting diodes based on green perovskite nanocrystals with mixed-metal cations. *Nano Energy*, 30:511–516, 2016.

[53] Wenyong Liu, Qianglu Lin, Hongbo Li, Kaifeng Wu, István Robel, Jeffrey M Pietryga, and Victor I Klimov. Mn2+-doped lead halide perovskite nanocrystals with dual-color emission controlled by halide content. *Journal of the American Chemical Society*, 138(45):14954–14961, 2016.

[54] Huiwen Liu, Zhennan Wu, Jieren Shao, Dong Yao, Hang Gao, Yi Liu, Weili Yu, Hao Zhang, and Bai Yang. Cspb x mn1–x cl3 perovskite quantum dots with high mn substitution ratio. *ACS Nano*, 11(2):2239–2247, 2017.

[55] Ward Van der Stam, Jaco J Geuchies, Thomas Altantzis, Karel HW Van Den Bos, Johannes D Meeldijk, Sandra Van Aert, Sara Bals, Daniel Vanmaekelbergh, and Celso de Mello Donega. Highly emissive divalent-ion-doped colloidal cspb1–x m x br3 perovskite nanocrystals through cation exchange. *Journal of the American Chemical Society*, 139(11):4087–4097, 2017.

[56] Raihana Begum, Manas R Parida, Ahmed L Abdelhady, Banavoth Murali, Noktan M Alyami, Ghada H Ahmed, Mohamed Nejib Hedhili, Osman M Bakr, and Omar F Mohammed. Engineering interfacial charge transfer in cspbbr3 perovskite nanocrystals by heterovalent doping. *Journal of the American Chemical Society*, 139(2):731–737, 2017.

[57] Subila K Balakrishnan and Prashant V Kamat. Au–cspbbr3 hybrid architecture: anchoring gold nanoparticles on cubic perovskite nanocrystals. *ACS Energy Letters*, 2(1):88–93, 2017.

[58] Hartmut Haug and Stephan W Koch. *Quantum theory of the optical and electronic properties of semiconductors*. World Scientific Publishing Company, 2009.

[59] Justinas Butkus, Parth Vashishtha, Kai Chen, Joseph K Gallaher, Shyamal KK Prasad, Dani Z Metin, Geoffry Laufersky, Nicola Gaston, Jonathan E Halpert, and Justin M Hodgkiss. The evolution of quantum confinement in cspbbr3 perovskite nanocrystals. *Chemistry of Materials*, 29(8):3644–3652, 2017.

[60] Manuel Cardona and Y Yu Peter. *Fundamentals of semiconductors*, volume 619. Springer, 2005.

[61] Warwick Bowen, Frank Vollmer, and Reuven Gordon. *Single Molecule Sensing Beyond Fluorescence*. Springer, 2022.

[62] Yuanjie Pang and Reuven Gordon. Optical trapping of a single protein. *Nano Letters*, 12(1):402–406, 2012.

[63] Jeffrey R Moffitt, Yann R Chemla, Steven B Smith, and Carlos Bustamante. Recent advances in optical tweezers. *Annu. Rev. Biochem.*, 77:205–228, 2008.

[64] Adam M Kaufman and Kang-Kuen Ni. Quantum science with optical tweezer arrays of ultracold atoms and molecules. *Nature Physics*, 17(12):1324–1333, 2021.

[65] Mathieu L Juan, Maurizio Righini, and Romain Quidant. Plasmon nano-optical tweezers. *Nature Photonics*, 5(6):349–356, 2011.

[66] Arthur Ashkin. Acceleration and trapping of particles by radiation pressure. *Physical Review Letters*, 24(4):156, 1970.

[67] Arthur Ashkin. Trapping of atoms by resonance radiation pressure. *Physical Review Letters*, 40(12):729, 1978.

[68] Arthur Ashkin. History of optical trapping and manipulation of small-neutral particle, atoms, and molecules. *IEEE Journal of Selected Topics in Quantum Electronics*, 6(6):841–856, 2000.

[69] Yasuhiro Harada and Toshimitsu Asakura. Radiation forces on a dielectric sphere in the rayleigh scattering regime. *Optics Communications*, 124(5-6):529–541, 1996.

[70] Arthur Ashkin, James M Dziedzic, John E Bjorkholm, and Steven Chu. Observation of a single-beam gradient force optical trap for dielectric particles. *Optics Letters*, 11(5):288–290, 1986.

[71] Reuven Gordon. Bethe's aperture theory for arrays. *Physical Review A*, 76(5):053806, 2007.

[72] Yuanjie Pang. *Nanophotonics with subwavelength apertures: theories and applications.* PhD thesis, University of Victoria, 2012.

[73] John David Jackson. Classical electrodynamics, 1999.

[74] Mathieu L Juan, Reuven Gordon, Yuanjie Pang, Fatima Eftekhari, and Romain Quidant. Self-induced back-action optical trapping of dielectric nanoparticles. *Nature Physics*, 5(12):915–919, 2009.

[75] Yuanyuan Chen, Abhay Kotnala, Li Yu, Jiasen Zhang, and Reuven Gordon. Wedge and gap plasmonic resonances in double nanoholes. *Optics Express*, 23(23):30227–30236, 2015.

[76] Zohreh Sharifi, Michael Dobinson, Ghazal Hajisalem, Mirali Seyed Shariatdoust, Adriaan L Frencken, Frank CJM van Veggel, and Reuven Gordon. Isolating and enhancing single-photon emitters for 1550 nm quantum light sources using double nanohole optical tweezers. *The Journal of Chemical Physics*, 154(18):184204, 2021.

[77] Liselotte Jauffred, Andrew C Richardson, and Lene B Oddershede. Three-dimensional optical control of individual quantum dots. *Nano Letters*, 8(10):3376–3380, 2008.

[78] Russell A Jensen, I-Chun Huang, Ou Chen, Jennifer T Choy, Thomas S Bischof, Marko Lončar, and Moungi G Bawendi. Optical trapping and two-photon excitation of colloidal quantum dots using bowtie apertures. *ACS Photonics*, 3(3):423–427, 2016.

[79] Wei-Yi Tsai, Jer-Shing Huang, and Chen-Bin Huang. Selective trapping or rotation of isotropic dielectric microparticles by optical near field in a plasmonic archimedes spiral. *Nano Letters*, 14(2):547–552, 2014.

[80] Chang Chen, Mathieu L Juan, Yi Li, Guido Maes, Gustaaf Borghs, Pol Van Dorpe, and Romain Quidant. Enhanced optical trapping and arrangement of nano-objects in a plasmonic nanocavity. *Nano letters*, 12(1):125–132, 2012.

[81] Amr AE Saleh, Sassan Sheikhoelislami, Steven Gastelum, and Jennifer A Dionne. Grating-flanked plasmonic coaxial apertures for efficient fiber optical tweezers. *Optics express*, 24(18):20593–20603, 2016.

[82] Yuquan Zhang, Changjun Min, Xiujie Dou, Xianyou Wang, Hendrik Paul Urbach, Michael G Somekh, and Xiaocong Yuan. Plasmonic tweezers: for nanoscale optical trapping and beyond. *Light: Science & Applications*, 10(1):1–41, 2021.

[83] Yoshito Tanaka, Shogo Kaneda, and Keiji Sasaki. Nanostructured potential of optical trapping using a plasmonic nanoblock pair. *Nano Letters*, 13(5):2146–2150, 2013.

[84] Steven Jones, Daniel Andren, Pawel Karpinski, and Mikael Kall. Photothermal heating of plasmonic nanoantennas: Influence on trapped particle dynamics and colloid distribution. *ACS Photonics*, 5(7):2878–2887, 2018.

[85] Mariko Toshimitsu, Yuriko Matsumura, Tatsuya Shoji, Noboru Kitamura, Mai Takase, Kei Murakoshi, Hiroaki Yamauchi, Syoji Ito, Hiroshi Miyasaka, Atsushi Nobuhiro, et al. Metallic-nanostructure-enhanced optical trapping of flexible polymer chains in aqueous solution as revealed by confocal fluorescence microspectroscopy. *The Journal of Physical Chemistry C*, 116(27):14610–14618, 2012.

[86] Kai Wang, Ethan Schonbrun, Paul Steinvurzel, and Kenneth B Crozier. Trapping and rotating nanoparticles using a plasmonic nano-tweezer with an integrated heat sink. *Nature Communications*, 2(1):1–6, 2011.

[87] Kuan-Yu Chen, An-Ting Lee, Chia-Chun Hung, Jer-Shing Huang, and Ya-Tang Yang. Transport and trapping in two-dimensional nanoscale plasmonic optical lattice. *Nano Letters*, 13(9):4118–4122, 2013.

[88] Yuxin Zheng, Jason Ryan, Paul Hansen, Yao-Te Cheng, Tsung-Ju Lu, and Lambertus Hesselink. Nano-optical conveyor belt, part ii: demonstration of handoff between near-field optical traps. *Nano Letters*, 14(6):2971–2976, 2014.

[89] Seung Ju Yoon, Jungmin Lee, Sangyoon Han, Chang-Kyu Kim, Chi Won Ahn, Myung-Ki Kim, and Yong-Hee Lee. Non-fluorescent nanoscopic monitoring of a single trapped nanoparticle via nonlinear point sources. *Nature Communications*, 9(1):1–8, 2018.

[90] Marios Sergides, Viet Giang Truong, and S Nic Chormaic. Highly tunable plasmonic nanoring arrays for nanoparticle manipulation and detection. *Nanotechnology*, 27(36):365301, 2016.

[91] Reuven Gordon. Future prospects for biomolecular trapping with nanostructured metals. *ACS Photonics*, 9(4):1127–1135, 2022.

[92] Alexander Rohrbach. Stiffness of optical traps: quantitative agreement between experiment and electromagnetic theory. *Physical Review Letters*, 95(16):168102, 2005.

[93] Abhay Kotnala and Reuven Gordon. Quantification of high-efficiency trapping of nanoparticles in a double nanohole optical tweezer. *Nano Letters*, 14(2):853–856, 2014.

[94] Skyler Wheaton and Reuven Gordon. Molecular weight characterization of single globular proteins using optical nanotweezers. *Analyst*, 140(14):4799–4803, 2015.

[95] Noa Hacohen, Candice JX Ip, and Reuven Gordon. Analysis of egg white protein composition with double nanohole optical tweezers. *ACS Omega*, 3(5):5266–5272, 2018.

[96] Cuifeng Ying, Edona Karakaci, Esteban Bermudez-Urena, Alessandro Ianiro, Ceri Foster, Saurabh Awasthi, Anirvan Guha, Louise Bryan, Jonathan List, Sandor Balog, et al. Watching single unmodified enzymes at work. *arXiv preprint arXiv:2107.06407*, 2021.

[97] Wei-Yi Chiang, Tomoki Okuhata, Anwar Usman, Naoto Tamai, and Hiroshi Masuhara. Efficient optical trapping of cdte quantum dots by femtosecond laser pulses. *The Journal of Physical Chemistry B*, 118(49):14010–14016, 2014.

[98] Yasuyuki Tsuboi, Tatsuya Shoji, Noboru Kitamura, Mai Takase, Kei Murakoshi, Yoshihiko Mizumoto, and Hajime Ishihara. Optical trapping of quantum dots based on gap-mode-excitation of localized surface plasmon. *The Journal of Physical Chemistry Letters*, 1(15):2327–2333, 2010.

[99] Pengfei Zhang, Gang Song, and Li Yu. Optical trapping of single quantum dots for cavity quantum electrodynamics. *Photonics Research*, 6(3):182–185, 2018.

[100] Poul M Bendix, Liselotte Jauffred, Kamilla Norregaard, and Lene B Oddershede. Optical trapping of nanoparticles and quantum dots. *IEEE Journal of Selected Topics in Quantum Electronics*, 20(3):15–26, 2013.

[101] Liselotte Jauffred and Lene B Oddershede. Two-photon quantum dot excitation during optical trapping. *Nano Letters*, 10(5):1927–1930, 2010.

[102] Christiane Becker, Sven Burger, Carlo Barth, Phillip Manley, Klaus Ja!!!FIX ME!!!ger, David Eisenhauer, Grit Ko!!!FIX ME!!!ppel, Pavel Chabera, Junsheng Chen, Kaibo Zheng, et al. Nanophotonic-enhanced two-photon-excited photoluminescence of perovskite quantum dots. *ACS Photonics*, 5(11):4668–4676, 2018.

[103] Fangying Juan, Fan Xu, Mei Wang, Mingxu Wang, Guozhi Hou, Jun Xu, Haoming Wei, Yinghua Wang, Yangqing Wu, and Bingqiang Cao. Photoluminescence enhancement of perovskite cspbbr3 quantum dots by plasmonic au nanorods. *Chemical Physics*, 530:110627, 2020.

[104] Peter J Shaw, Christopher G Bailey, Giacomo Piana, Thomas M Mercier, Antonios G Kanaras, Pavlos G Lagoudakis, and Martin DB Charlton. Resonant energy transfer properties of perovskite nanocrystals. In *Quantum Dots, Nanostructures, and Quantum Materials: Growth, Characterization, and Modeling XVII*, volume 11291, page 112910H. International Society for Optics and Photonics, 2020.

[105] Ping-Chin Cheng. The contrast formation in optical microscopy. In *Handbook of biological confocal microscopy*, pages 162–206. Springer, 2006.

[106] Herbert Schneckenburger. Förster resonance energy transfer–what can we learn and how can we use it? *Methods and Applications in Fluorescence*, 8(1):013001, 2019.

[107] Daniel C Harris. *Quantitative Chemical Analysis*. Macmillan, 2010.

[108] Robert M Clegg. Fluorescence resonance energy transfer. *Current Ppinion in Biotechnology*, 6(1):103–110, 1995.

[109] Sanghwa Lee, Jinwoo Lee, and Sungchul Hohng. Single-molecule three-color fret with both negligible spectral overlap and long observation time. *PloS One*, 5(8):e12270, 2010.

[110] Robert M Clegg. Förster resonance energy transfer—fret what is it, why do it, and how it's done. *Laboratory techniques in biochemistry and molecular biology*, 33:1–57, 2009.

[111] C King, B Barbiellini, D Moser, and V Renugopalakrishnan. Exactly soluble model of resonant energy transfer between molecules. *Physical Review B*, 85(12):125106, 2012.

[112] David L Dexter. A theory of sensitized luminescence in solids. *The Journal of Chemical Physics*, 21(5):836–850, 1953.

[113] Andrey L Rogach, Thomas A Klar, John M Lupton, Andries Meijerink, and Jochen Feldmann. Energy transfer with semiconductor nanocrystals. *Journal of Materials Chemistry*, 19(9):1208–1221, 2009.

[114] Somnath Koley, Jiabin Cui, Yossef E Panfil, and Uri Banin. Coupled colloidal quantum dot molecules. *Accounts of Chemical Research*, 54(5):1178–1188, 2021.

[115] Yossef E Panfil, Doaa Shamalia, Jiabin Cui, Somnath Koley, and Uri Banin. Electronic coupling in colloidal quantum dot molecules; the case of cdse/cds core/shell homodimers. *The Journal of Chemical Physics*, 151(22):224501, 2019.

[116] Jiabin Cui, Yossef E Panfil, Somnath Koley, Doaa Shamalia, Nir Waiskopf, Sergei Remennik, Inna Popov, Meirav Oded, and Uri Banin. Colloidal quantum dot molecules manifesting quantum coupling at room temperature. *Nature Communications*, 10(1):1–10, 2019.

[117] Kane Yee. Numerical solution of initial boundary value problems involving maxwell's equations in isotropic media. *IEEE Transactions on Antennas and Propagation*, 14(3):302–307, 1966.

[118] Jean-Pierre Berenger. A perfectly matched layer for the absorption of electromagnetic waves. *Journal of computational physics*, 114(2):185–200, 1994.

[119] Adarsh Lalitha Ravindranath, Mirali Seyed Shariatdoust, Samuel Mathew, and Reuven Gordon. Colloidal lithography double-nanohole optical trapping of nanoparticles and proteins. *Optics Express*, 27(11):16184–16194, 2019.

[120] Fisher Scientific. Harrick plasma high power expanded plasma cleaner 115v, 2022.

[121] Ghazal Hajisalem, Elham Babaei, Michael Dobinson, Shohei Iwamoto, Zohreh Sharifi, Jon Eby, Marie Synakewicz, Laura S Itzhaki, and Reuven Gordon. Accessible high-performance double nanohole tweezers. *Optics Express*, 30(3):3760–3769, 2022.

[122] Gabriele Rainò, Michael A Becker, Maryna I Bodnarchuk, Rainer F Mahrt, Maksym V Kovalenko, and Thilo Stöferle. Superfluorescence from lead halide perovskite quantum dot superlattices. *Nature*, 563(7733):671–675, 2018.

[123] Danny Kim, Samuel G Carter, Alex Greilich, Allan S Bracker, and Daniel Gammon. Ultrafast optical control of entanglement between two quantum-dot spins. *Nature Physics*, 7(3):223–229, 2011.

[124] Guillemin Rodary, Lorenzo Bernardi, Christophe David, Bruno Fain, Aristide Lemaître, and Jean-Christophe Girard. Real space observation of electronic coupling between self-assembled quantum dots. *Nano Letters*, 19(6):3699–3706, 2019.

[125] James Cassidy, Mingrui Yang, Dulanjan Harankahage, Dmitry Porotnikov, Pavel Moroz, Natalia Razgoniaeva, Cole Ellison, Jacob Bettinger, Shafqat Ehsan, John Sanchez, et al. Tuning the dimensionality of excitons in colloidal quantum dot molecules. *Nano Letters*, 21(17):7339–7346, 2021.

[126] Ana Zehtabi-Oskuie, Hao Jiang, Bryce R Cyr, Douglas W Rennehan, Ahmed A Al-Balushi, and Reuven Gordon. Double nanohole optical trapping: dynamics and protein-antibody co-trapping. *Lab on a Chip*, 13(13):2563–2568, 2013.

[127] Xiafang Du, Guan Wu, Jian Cheng, Hui Dang, Kangzhe Ma, Ya-Wen Zhang, Peng-Feng Tan, and Su Chen. High-quality cspbbr 3 perovskite nanocrystals for quantum dot light-emitting diodes. *RSC Advances*, 7(17):10391–10396, 2017.

[128] Amirhossein Alizadehkhaledi, Adriaan L Frencken, Frank CJM van Veggel, and Reuven Gordon. Isolating nanocrystals with an individual erbium emitter: A route to a stable single-photon source at 1550 nm wavelength. *Nano Letters*, 20(2):1018–1022, 2019.

[129] Johann Berthelot, Srdjan S Aćimović, Mathieu L Juan, Mark P Kreuzer, Jan Renger, and Romain Quidant. Three-dimensional manipulation with scanning near-field optical nanotweezers. *Nature Nanotechnology*, 9(4):295–299, 2014.

[130] Louis Brus. Electronic wave functions in semiconductor clusters: experiment and theory. *The Journal of Physical Chemistry*, 90(12):2555–2560, June 1986.

[131] Ruo Xi Yang and Liang Z Tan. Understanding size dependence of phase stability and band gap in cspbi3 perovskite nanocrystals. *The Journal of Chemical Physics*, 152(3):034702, 2020.

[132] Michael A. Becker, Roman Vaxenburg, Georgian Nedelcu, Peter C. Sercel, Andrew Shabaev, Michael J. Mehl, John G. Michopoulos, Samuel G. Lambrakos, Noam Bernstein, John L. Lyons, Thilo Stöferle, Rainer F. Mahrt, Maksym V. Kovalenko, David J. Norris, Gabriele Rainò, and Alexander L. Efros. Bright triplet excitons in caesium lead halide perovskites. *Nature*, 553(7687):189–193, January 2018.

[133] Xiaochun Liu, Haifeng Zhao, Linfeng Wei, Xinjian Ren, Xinyang Zhang, Faming Li, Peng Zeng, and Mingzhen Liu. Ligand-modulated electron transfer rates from cspbbr3 nanocrystals to titanium dioxide. *Nanophotonics*, 10(8):1967–1975, 2020.

[134] Jian Wu, Dao Xiang, and Reuven Gordon. Monitoring gold nanoparticle growth in situ via the acoustic vibrations probed by four-wave mixing. *Analytical Chemistry*, 89(4):2196–2200, 2017.

[135] Brendon W Lovett, John H Reina, Ahsan Nazir, and G Andrew D Briggs. Optical schemes for quantum computation in quantum dot molecules. *Physical Review B*, 68(20):205319, 2003.

[136] Ricardo Amils, Muriel Gargaud, José Cernicharo Quintanilla, Henderson James Cleaves, William M. Irvine, Daniele Pinti, and Michel Viso, editors. *Rayleigh Scattering*, pages 1–3. Springer Berlin Heidelberg, Berlin, Heidelberg, 2014.

[137] Bin Li, He Huang, Guofeng Zhang, Changgang Yang, Wenli Guo, Ruiyun Chen, Chengbing Qin, Yan Gao, Vasudevan P Biju, Andrey L Rogach, et al. Excitons and biexciton dynamics in single cspbbr3 perovskite quantum dots. *The Journal of Physical Chemistry Letters*, 9(24):6934–6940, 2018.

[138] Selvakumar V Nair and Toshihide Takagahara. Theory of exciton pair states and their nonlinear optical properties in semiconductor quantum dots. *Physical Review B*, 55(8):5153, 1997.

[139] Jeffrey T. DuBose and Prashant V. Kamat. Directing energy transfer in halide perovskite–chromophore hybrid assemblies. *Journal of the American Chemical Society*, 143(45):19214–19223, November 2021.

[140] Marten Richter, Kwang Jun Ahn, Andreas Knorr, Andrei Schliwa, Dieter Bimberg, Mohamed El-Amine Madjet, and Thomas Renger. Theory of excitation transfer in coupled nanostructures – from quantum dots to light harvesting complexes. *Physica Status Solidi (b)*, 243(10):2302–2310, August 2006.

[141] Judith F. Specht, Andreas Knorr, and Marten Richter. Two-dimensional spectroscopy: An approach to distinguish Förster and Dexter transfer processes in coupled nanostructures. *Physical Review B*, 91:155313, Apr 2015.

[142] Chelsea Carlson, Andreas Knorr, and Stephen Hughes. Screening of the quantum dot Förster coupling at small distances. *Optics Letters*, 45(13):3357, June 2020.

[143] Konstantin V. Reich and Boris I. Shklovskii. Exciton transfer in array of epitaxially connected nanocrystals. *ACS Nano*, 10(11):10267–10274, November 2016.

[144] Jingjing Xue, Rui Wang, Lan Chen, Selbi Nuryyeva, Tae-Hee Han, Tianyi Huang, Shaun Tan, Jiahui Zhu, Minhuan Wang, Zhao-Kui Wang, et al. A small-molecule "charge driver" enables perovskite quantum dot solar cells with efficiency approaching 13%. *Advanced Materials*, 31(37):1900111, 2019.

[145] David L Andrews, Carles Curutchet, and Gregory D Scholes. Resonance energy transfer: beyond the limits. *Laser & Photonics Reviews*, 5(1):114–123, 2011.

[146] Weina Zhang, Juan Li, Hongxiang Lei, and Baojun Li. Temperature-dependent förster resonance energy transfer from upconversion nanoparticles to quantum dots. *Optics Express*, 28(8):12450–12459, 2020.

[147] Ahsan Nazir, Brendon W Lovett, Sean D Barrett, John H Reina, and G Andrew D Briggs. Anticrossings in förster coupled quantum dots. *Physical Review B*, 71(4):045334, 2005.

[148] Ahsan Nazir. Correlation-dependent coherent to incoherent transitions in resonant energy transfer dynamics. *Physical Review Letters*, 103(14):146404, 2009.

[149] P. Thomas, M. Möller, R. Eichmann, T. Meier, T. Stroucken, and A. Knorr. Microscopic foundation of the Förster excitonic energy transfer process. *Physica Status Solidi B-basic Solid State Physics - PHYS STATUS SOLIDI B-BASIC SO*, 230:25–29, 03 2002.

[150] Th. Förster. Zwischenmolekulare energiewanderung und fluoreszenz. *Annalen der Physik*, 437(1-2):55–75, January 1948.

[151] Gabriele Rainò, Georgian Nedelcu, Loredana Protesescu, Maryna I. Bodnarchuk, Maksym V. Kovalenko, Rainer F. Mahrt, and Thilo Stöferle. Single cesium lead halide perovskite nanocrystals at low temperature: Fast single-photon emission, reduced blinking, and exciton fine structure. *ACS Nano*, 10(2):2485–2490, January 2016.

[152] D.P. Craig and T. Thirunamachandran. Radiation–molecule interactions in chemical physics. In *Advances in Quantum Chemistry Volume 16*, pages 97–160. Elsevier, 1982.

[153] A Thränhardt, C Ell, Galina Khitrova, and HM Gibbs. Relation between dipole moment and radiative lifetime in interface fluctuation quantum dots. *Physical Review B*, 65(3):035327, 2002.

[154] Wenbi Shcherbakov-Wu, Peter C. Sercel, Franziska Krieg, Maksym V. Kovalenko, and William A. Tisdale. Temperature-independent dielectric constant in CsPbBr3 nanocrystals revealed by linear absorption spectroscopy. *The Journal of Physical Chemistry Letters*, 12(33):8088–8095, August 2021.

[155] Agnes Sambale, Stefan Yoshi Buhmann, Dirk-Gunnar Welsch, and Marin-Slodoban Tomaš. Local-field correction to one- and two-atom van der Waals interactions. *Physical Review A*, 75:042109, Apr 2007.

[156] Michael Paulus, Phillipe Gay-Balmaz, and Olivier J. F. Martin. Accurate and efficient computation of the Green's tensor for stratified media. *Physical Review E*, 62:5797–5807, Oct 2000.

[157] P. B. Johnson and R. W. Christy. Optical constants of the noble metals. *Physical Review B*, 6(12):4370–4379, 1972.

Appendix A

Reproducible spectra from different DNHs

Figure A1 shows the repeatability of the results for thirty different DNHs on the same gold sample, with at least 6 trapping events for each DNH. Polynomial fitting is used to find the peak for analysis (concatenation fitting with multiple curves). During the experiment, we observed blinking, which can be seen from the fluctuations in the intensity of the spectra.

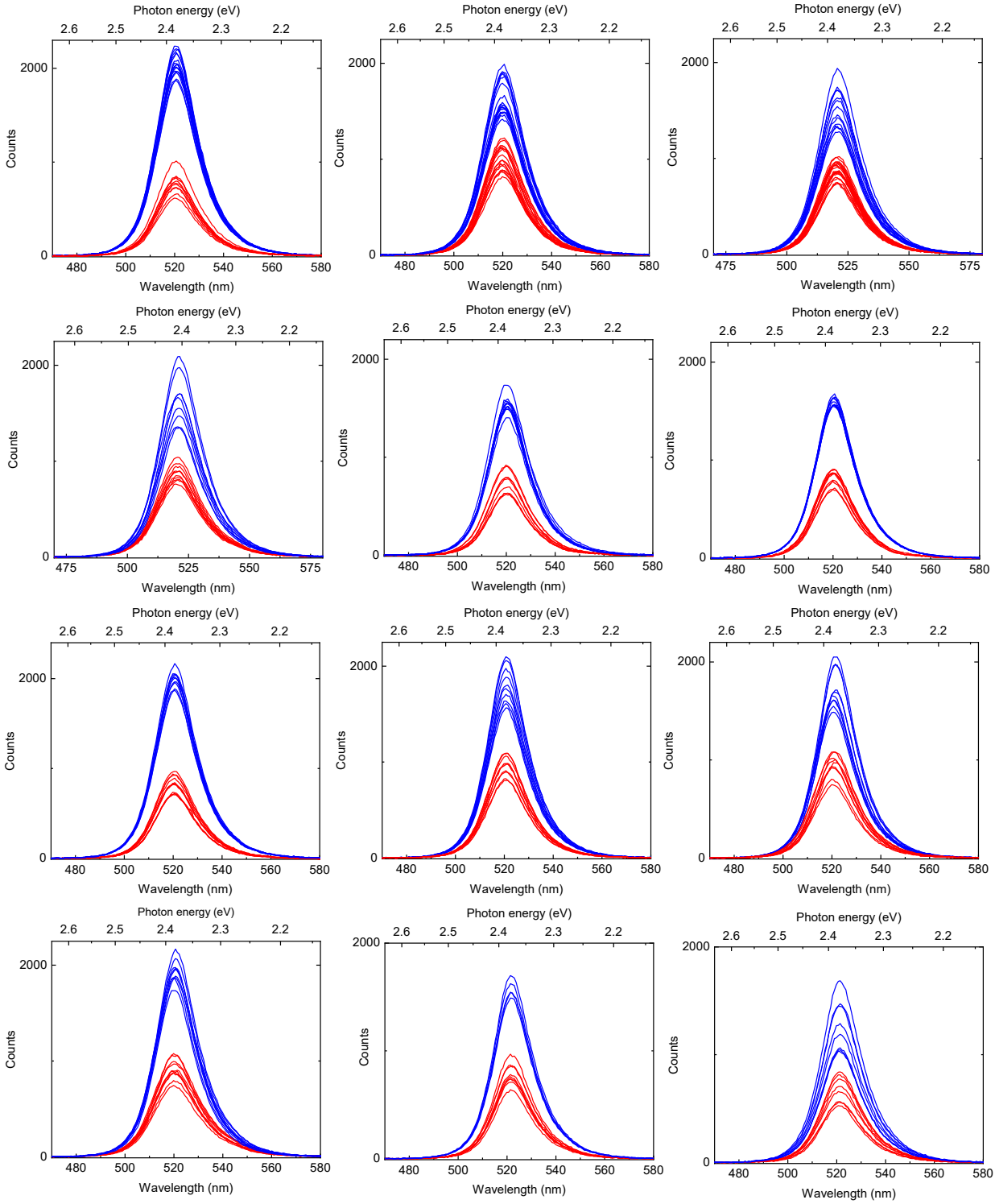
Photon energy (eV)
2.6 2.5 2.4 2.3 2.2
Counts
Wavelength (nm)

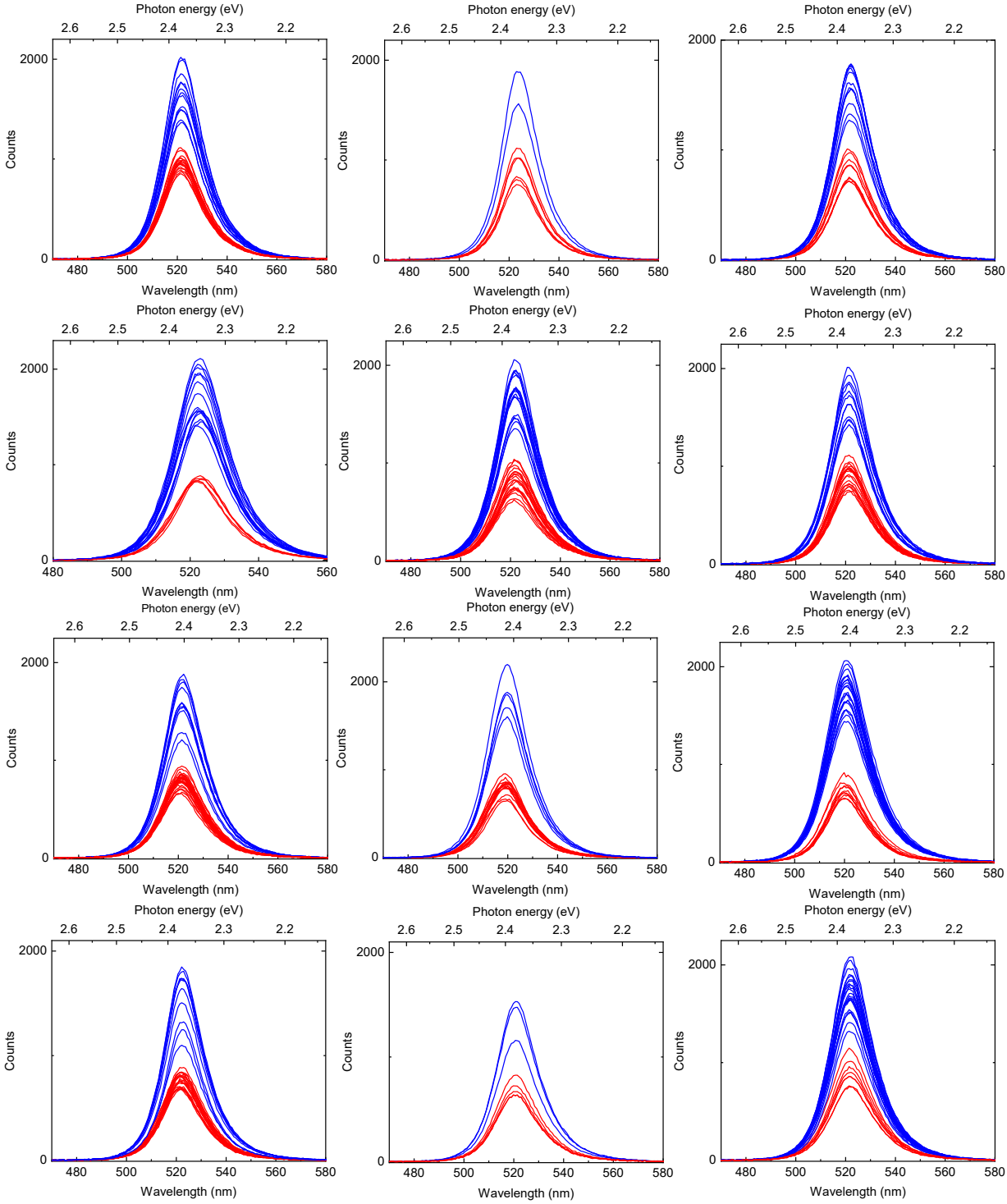
Photon energy (eV)
2.6 2.5 2.4 2.3 2.2
Counts
2000
0
480 500 520 540 560 580
Wavelength (nm)

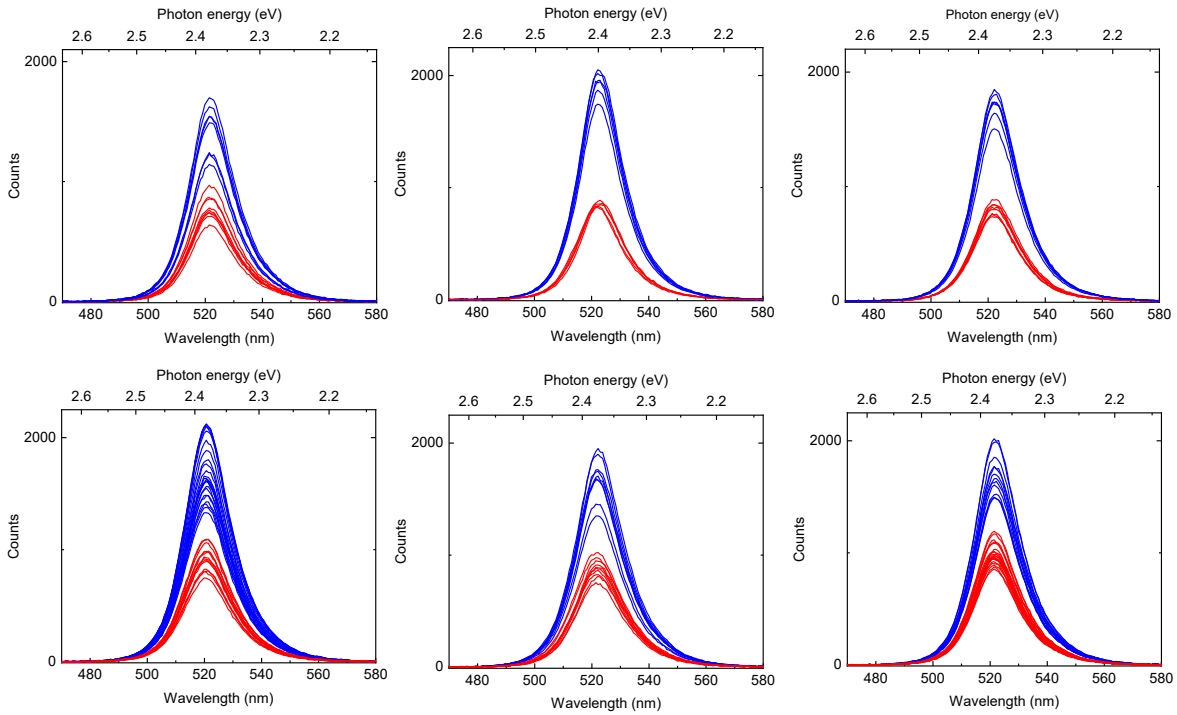

Fig. A1: The single and double trapping spectra for different 30 DNHs. Every DNH was measured at least 6 times for reproducible single - double trapping event, respectively.

Appendix B

Theory and Simulations of Coupled Quantum Dots

Photon exchange from coupled dipoles in a general medium

The radiative decay rate from a single dipole emitter is defined from

$$\Gamma_1(\mathbf{r}_1) = \frac{2\mathbf{d}_1 \cdot \mathrm{Im}\{\mathbf{G}(\mathbf{r}_1, \mathbf{r}_1, \omega)\} \cdot \mathbf{d}_1}{\epsilon_0 \hbar}, \tag{B.1}$$

for an emitter with dipole moment $\mathbf{d}_1$ (assumed real) at position $\mathbf{r}_1$, and $\mathbf{G}$ is the photon Green function. For coupled dipoles (the second one is with real dipole moment $\mathbf{d}_2$ at $\mathbf{r}_2$), the photon exchange mechanism is connected to real and imaginary parts of the Green function, defined from incoherent rates of photon transfer:

$$\Gamma_{12} = \frac{2\mathbf{d}_1 \cdot \mathrm{Im}\{\mathbf{G}(\mathbf{r}_1, \mathbf{r}_2, \omega)\} \cdot \mathbf{d}_2}{\epsilon_0 \hbar}, \tag{B.2}$$

and a coherent exchange term

$$\Delta_{12} = -\frac{\mathbf{d}_1 \cdot \mathrm{Re}\{\mathbf{G}(\mathbf{r}_1, \mathbf{r}_2, \omega)\} \cdot \mathbf{d}_2}{\epsilon_0 \hbar}, \tag{B.3}$$

where the latter has the same origin as Förster coupling [149]. Specifically, when one considers a homogeneous medium, the near-feld electrostatic part identically recovers the Förster coupling term. Below, for ease of notation, we will introduce the shorthand notation $\mathbf{G}_{12} = \mathbf{G}(\mathbf{r}_1, \mathbf{r}_2)$ and $\mathbf{G}_{11} = \mathbf{G}(\mathbf{r}_1, \mathbf{r}_1)$. For identical dipole emitters, the resonance will split by $\pm\hbar\Delta_{12} \equiv \pm V_F$, into subradiant and superradiant states. In a

Markov approximation, these radiative decay rates are usually evaluated on resonance, which also yield agreement with a Fermi's golden rule approach.

The Green function $\mathbf{G}(\mathbf{r}, \mathbf{r}_0, \omega)$, describes light propagation from a source point $\mathbf{r}_0$ to $\mathbf{r}$ and is formally defined via the Helmholtz equation

$$\boldsymbol{\nabla} \times \boldsymbol{\nabla} \times \mathbf{G}(\mathbf{r}, \mathbf{r}_0, \omega) - k_0^2 \epsilon(\mathbf{r}, \omega) \mathbf{G}(\mathbf{r}, \mathbf{r}_0, \omega) = k_0^2 \delta(\mathbf{r} - \mathbf{r}_0), \tag{B.4}$$

together with suitable radiation conditions.

In a background medium with permittivity $\epsilon_b = n_b^2$ (assumed lossless, see Fig. B1 left side), the Green function is known analytically. For two s-polarized dipoles (z-polarized),

$$G_{12}^{ss} = \frac{k_0^2 e^{ik_b r_{12}}}{4\pi r_{12}} \left[1 + \frac{i}{k_b r_{12}} - \frac{1}{(k_b r_{12})^2} \right], \tag{B.5}$$

and for two p-polarized dipoles (x-polarized),

$$G_{12}^{pp} = G_{12}^{ss} + \frac{k_0^2 e^{ik_b r_{12}}}{4\pi r_{12}} \left[-1 - \frac{3i}{k_b r_{12}} + \frac{3}{(k_b r_{12})^2} \right], \tag{B.6}$$

where the dipoles are separated by distance r_{12}, center to center, $k_0 = \omega/c$ and $k_b = n_b \omega/c$. For dipoles that are sufficiently close together (near field regime), one can approximate the above forms with the static contribution only, so that:

$$G_{12}^{ss}|_{\text{near}} = -\frac{1}{4\pi \epsilon_b r_{12}^3}, \tag{B.7}$$

and for two p-polarized dipoles,

$$G_{12}^{pp}|_{\text{near}} = \frac{2}{4\pi \epsilon_b r_{12}^3}. \tag{B.8}$$

These *near field coupling* terms, in combination with Eq. (B.3), identically recover the well known Förster coupling rates [150].

Radiative decay rates and photon exchange rates for lead perovskite quantum dots

Experiments on single PQDs [151] report a single radiative lifetime of 250 ps, corresponding to a spectral linewidth of around 2.7 μeV. These rates are also consistent with those reported in Ref. [132], for $CsPbBr_3$ for QDs around 10-nm cubed. The reason for these significant decay rates, is that such QDs are in the intermediate to

weak quantum confinement regime, as the QD size is larger than the exciton Bohr radius.

For our PQDs, the electron Bohr radius is obtained from $s_e = 4\pi\epsilon_{QD}\epsilon_0\hbar^2/(e^2 m_e) \approx$ 1.9 nm (using $m_e = 0.13m_0$ and $\epsilon_{QD} = 4.8$), which is clearly much smaller than the size of our QDs (10 nm). This large ratio is the origin of the large oscillator strength for the radiative decay [138], a mesoscopic enhancement effect. This in turn enhances the radiative decay rate and also to the dipole-dipole exchange rates.

In Ref. [132], a variational approach was given with the following trial wave functions (electron-hole picture):

$$v(\mathbf{r}_e, \mathbf{r}_h) = Ce^{-b|\mathbf{r}_e - \mathbf{r}_h|}\phi(\mathbf{r}_e)\phi(\mathbf{r}_h), \tag{B.9}$$

where C is determined from

$$\int d\mathbf{r}d\mathbf{r}' v(\mathbf{r}, \mathbf{r}') = 1, \tag{B.10}$$

and

$$\phi(\mathbf{r}) = \left(\frac{2}{L}\right)^{3/2} \cos\left(\frac{\pi x}{a}\right) \cos\left(\frac{\pi y}{a}\right) \cos\left(\frac{\pi z}{a}\right). \tag{B.11}$$

The envelope wavefunction of the exciton $v(\mathbf{r}, \mathbf{r}')$ (from a product of the ground state electron and hole ground wave functions) is required to compute the oscillator strength and exciton dipole moments.

The parameter b has been extracted as a function of QD cube length L, and for $L/a_e \approx 5 - 6$ is $b = 1.75/L$ (see supplementary material of [132]). Carrying out the 6D integration (Eq. (B.10)) with this new wave function, then the oscillator strength increases by C, which we compute to be $C = 3.79$ for $b = 1.6$; $C = 4.25$ for $b = 1.75$; and $C = 4.71$ for $b = 2$. Thus we estimate that the excitonic oscillator strength is about a factor of 4-5 larger than that for a QD in the strong confinement regime. Using wave functions for excitons in the weak confinement regime, increases the oscillator strength even further [132], and scale with $8L^3/\pi^2 a_B^3$, where a_B is the exciton Bohr radius.

The main photoluminescence lines of PQDs consist of three linearly-polarized triplet excitons, which are nondegenerate, one of which is dominant. At elevated temperatures, this will be significantly broadened due to non-radiative processes, such as electron-phonon interactions, but these should not affect the coherent dipole-dipole interactions.

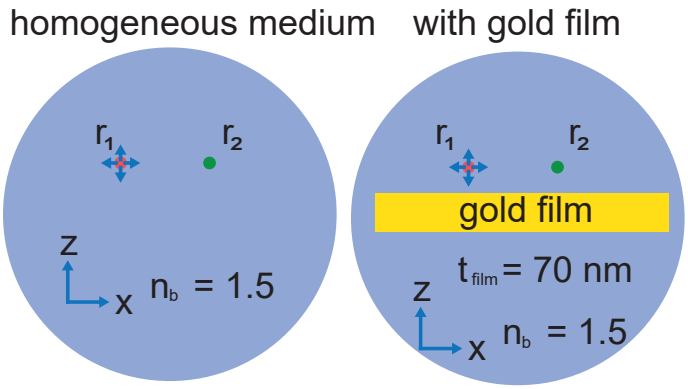

Fig. B1: Schematic of two coupled dipoles in homogeneous medium (left side) and above a gold film (right side). They are 11 nm separated in x direction. With gold film, they are 6 nm away from the film surface in z direction. The dipoles could be set as x-polarized and z-polarized.

As an example, if we consider two coupled dipoles of magnitude $d_1 = d_2 = 0.72$ e $\cdot$ nm (which give the same radiative decay rates mentioned before), as well as $r_{12} = 11$ nm (which includes a 1 nm gap, Fig. B1 left side), $\epsilon_b = 1.5^2$, $\hbar\omega = \hbar\omega_1 = \hbar\omega_2 = 2.4$ eV, then

$$\hbar\Gamma_1 = \hbar\Gamma_2 = \frac{n_b \omega_1^3 d_1^2}{3\pi\epsilon_0 c^3} = 2.69 \ \mu\text{eV}, \tag{B.12}$$

corresponding to a lifetime of around 250 ps. However, these estimates do not account for local field corrections, which are discussed below. They also only consider one linearly polarized dipole, and we know there are three active dipole moments likely contributing to out main emission resonance.

The coherent exchange term, with s-polarized dipoles (z-polarized), is

$$\hbar\Delta_{12}^{ss} = \frac{d^2}{4\pi\epsilon_0\epsilon_b r_{12}^3} \approx 93 \ \hbar\Gamma_1 = 0.25 \text{ meV}, \tag{B.13}$$

while for p-polarized dipoles (x-polarized),

$$\hbar\Delta_{12}^{pp} = -\frac{d^2}{2\pi\epsilon_0\epsilon_b r_{12}^3} \approx -186 \ \hbar\Gamma_1 = -0.50 \text{ meV}. \tag{B.14}$$

As expected, and as mentioned earlier, these are identical in form to the well known Förster coupling rate [152],

$$V_F = \hbar\Delta\omega_F = \frac{d_1 d_2}{4\pi\epsilon_b\epsilon_0 r_{12}^3}(\delta_{ij} - \hat{n}_i\hat{n}_j), \tag{B.15}$$

for two dipoles that are polarized along i and j.

Without considering any effects from the metal film (or DNH topology) or local field corrections, we thus expect a maximum shift, for p-polarized dipoles (x-polarized), of around $-186\hbar\Gamma_1$. This is significant, and estimated to be around 0.5 meV red shift (within a dipole approximation).

Local field corrections

The radiative decay rates and photon-exchange rates are affected by local field effects, since the PQD cubes have a different dielectric constant than the surrounding medium. Specifically one has [153]

$$\Gamma_1^{\text{loc}} = D_1^2\Gamma_1 = \left(\frac{3\epsilon_b}{2\epsilon_b + \epsilon_{QD}}\right)^2 \Gamma_1. \tag{B.16}$$

Values for ϵ_{QD} on PQDs vary in the literature from around 6-7 [154] in bulk (and thin films) to 4.8 for QDs [132]. So we will consider two values, $\epsilon_{QD} = 6.25$ and $\epsilon_{QD} = 4.8$. With $\epsilon_{QD} = 6.25$, then we expect a local field reduction factor of

$$\Gamma_1^{\text{loc}} \approx 0.4\Gamma_1. \tag{B.17}$$

This is only an estimate as it neglects finite size effects, but this is expected to be reasonable for very small PQDs, essentially only including a depolarization factor. If we use $\epsilon_{QD} = 4.8$, then the local field reduction is slightly less, with $D_1^2 = 0.53$.

Since we have estimated $d = d_1 = d_2$ from the experimental radiate decay rates, clearly these are reduced from the actual ones, but it does not matter if we regard d as an *effective dipole moment* including local field corrections, or we can simply increase this value in the presence or local field effects (which would reduce the local all rates). The reason this does not matter, is that for identical QD cubes, the same reduction factor applies also to the dipole-dipole coupling rates [155]. Thus,

$$\frac{\text{Re}G_{12}|_{\text{loc}}}{\text{Im}G_b|_{\text{loc}}} \approx \frac{\text{Re}G_{12}}{\text{Im}G_b}, \tag{B.18}$$

and so we can once again scale our frequency shift in terms on the experimental radiative decay rate. We will show the explicitly below, with full numerical simulations.

Exact photon Green function solutions in the presence of a gold film

To more accurately assess the effects of the gold film, and to include the possibility of plasmon polariton effects and image dipole effects, we now calculate the exact Green functions with a metal film, specifically a 70-nm gold film (Fig. B1 right side). Clearly this is only an estimate for our DNH structure, which may also have some background resonance effects from the nano-hole geometry. Nevertheless, it is useful to assess the expected role of the gold film.

We use a well established multi-layered Green function approach [156]. For gold, we adopt a simple Drude model for the complex dielectric constant

$$\epsilon_{\text{film}} = \epsilon_{\text{gold}} = 1 - \frac{\omega_p^2}{\omega(\omega + i\gamma)}, \tag{B.19}$$

with $\gamma = 1.41 \times 10^{14}$ rads/s and $\omega_p = 1.26 \times 10^{16}$ rads/s. However, we also consider a more realistic model [157].

Fig. B2 shows the computation of the propagator for coupling two dipoles (Drude

model), that are 6 nm from the metal (1-nm height/gap above the interface, Fig. B1 right side), which act to reduce the homogeneous contributions given above. For example, the real part of the s-polarized (z-polarized) propagator ($\mathrm{Re}\{G_{12}^{\mathrm{total}}\}$) changes from -182 (using the analytical Green functions, with a homogeneous medium, in Purcell factor units) to -115 (with a gold film included in the calculations, solid blue curve at $\hbar\omega = 2.4$ eV in left side of Fig. B2). We have also computed the same function in COMSOL and obtained -114 (not shown), a remarkably good agreement. Fig. B3 shows identical simulations, but with a more realistic material model for gold [157]. Clearly, we obtain exactly the same trends, so the Drude model seems reasonable for these simulations.

Full electromagnetic simulations using COMSOL

To corroborate the above analytical studies and arguments, we also compute the photon Green functions numerically, for a general medium including the QD cubes and the metal film. This can also give insight into any extra scattering effects that may occur, such as scattering from the coupled QD cubes, though we expect such effects to play a minor role. We use $\epsilon_b = 2.25$ and $\epsilon_{QD} = n_{\mathrm{cube}}^2 = 6.25$, but the results will scale with different ϵ_{QD}, since we divide the final photon exchange terms by calculated radiative rates that also include local field corrections. We have also checked this explicitly, and the relative differences with $\epsilon_{QD} = 4.8$ compared to 6.25 are only a few percent.

To compute the numerical Green function for a general photonic medium, we use COMSOL, including the PQD cubes (modified background response) and the gold film. With a dipole source excitation, we could easily get $\mathbf{E}^{\mathrm{total}}(\mathbf{r})$ and $\mathbf{E}^{\mathrm{b}}(\mathbf{r})$, which are the electric fields with and without the scatterers in the medium. The scattered field is then obtained from $\mathbf{E}^{\mathrm{scatt}}(\mathbf{r}) = \mathbf{E}^{\mathrm{total}}(\mathbf{r}) - \mathbf{E}^{\mathrm{b}}(\mathbf{r})$. To obtain the numerical scattered Green function, we exploit the following expression for the scattered field from a dipole source at $\mathbf{r}_0$,

$$\mathbf{E}^{\mathrm{scatt}}(\mathbf{r},\omega) = \mathbf{G}^{\mathrm{scatt}}(\mathbf{r},\mathbf{r}_0,\omega)\cdot\frac{\mathbf{d}}{\epsilon_0}, \tag{B.20}$$

where the scattered field $\mathbf{E}^{\mathrm{scatt}}$ has unit of V/m, the Green function $\mathbf{G}^{\mathrm{scatt}}$ has unit of m^{-3}, and the dipole moment $\mathbf{d}$ has unit of $\mathrm{C}\cdot\mathrm{m}$. We can also obtain the total Green

function in the same way,

$$\mathbf{E}^{\text{total}}(\mathbf{r},\omega) = \mathbf{G}^{\text{total}}(\mathbf{r},\mathbf{r}_0,\omega)\cdot\frac{\mathbf{d}}{\epsilon_0}, \tag{B.21}$$

though one should avoid computing $\text{Re}\{\mathbf{G}^{\text{total}}(\mathbf{r}_0,\mathbf{r}_0)\}$, as it is divergent; however, $\mathbf{G}^{\text{scatt}}(\mathbf{r}_0,\mathbf{r}_0)$ (real and imaginary parts) and all other Green function quantities ($\mathbf{r}\neq\mathbf{r}_0$) are well defined.

Within the simulation, the source dipole is placed at $\mathbf{r}_1$ (Fig. B4) and assumed polarized along some i direction (such as the x,y,z). Thus we can write the dipole moment as $\mathbf{d} = d\mathbf{n}_i$, where d is the value of the dipole moment, and $\mathbf{n}_i$ is a uniot vector. Note this dipole moment is not related to d_1 and d_2, but is simply a linear dipole in Maxwell's equations to obtain the numerical Green functions.

First we explore local field corrections, with one PQD and two PQDs (Fig. B4 (a,b)), since additional scattering can be captured that may show up on top of the usual formula shown earlier, namely Eq. (B.16). Fig. B5 shows the COMSOL simulations from the PQD cubes. The single PQD results are shown to match the analytical expressions very well, and the two PQD case shows a departure in the case of x-polarized dipoles (p-polarized). Thus, additional scattering is shown to enhance the projected LDOS (local density of states), or for an x-polarized dipoles; however, its impact is relatively small.

Next, to connect to the photon exchange coupling rates (which will include the usual Förster contribution), we compute the numerically exact propagator (within numerical uncertainties), and corresponding scattering rates (for cube dimer placed side by side above a gold film, Fig. B4 (c)), as shown in Fig. B6. Importantly, these are normalized by the single PQD decay rate, and all simulations include the PQDs; thus local field effects are also included in the normalization, and all scattering effects are included for the calculation of the propagators.

Overall, the trends are seen to be in good agreement with the analytical results shown earlier in Fig. B2. Note that if we remove the PQD cubes from the COMSOL calculations and include only the metal film (Fig. B1 right side), then the agreement with the analytical solution is less than 1%. As mentioned above, the real part of the total Green functions $\text{Re}(G_{12})$ for an z-polarized dipole is -115 (in Purcell units, solid blue curve at $\hbar\omega = 2.4$ eV in left side of Fig. B2) from the analytical Green function results and -114 from COMSOL simulations (not shown). Even with small quantitative differences the overall conclusion is the same. When with full structure,

i.e., PQDs separated by 11-nm (placed side by side), and 1-nm above a gold film (Fig. B4 (c)), the maximum frequency shift expected is around $-163\Gamma_1$, where Γ_1 includes local field corrections. Assuming $\hbar\Gamma_1 \approx 2.69$ μeV, then we predict a spectral shift of -0.44 meV, for p-polarized (x-polarized) dipoles.

Additional calculations for vertically coupled QD cubes on gold film (one cube is placed on the top of the other one) are shown in the main text.

As mentioned in the main text, after initial calculations at a 1 nm gap size, we obtained a more accurate measurement of the gap size from high-resolution TEM as being 1.4 nm. This is expected theoretically to reduce the interaction by around 10%, which we confirmed by simulation of an typical structure (see Fig. B7).

Other potential sources and mechanisms for coupled-PQD frequency shifts

Next, we briefly discuss some other potential effects that could cause large frequency shifts for coupled PQDs.

For quantum emitters that are very close together, namely, where electronic tunneling is possible, excitons can be transferred, which is typically termed Dexter energy transfer [139]. This process is usually negligible for distances greater than 1 nm. Dexter is a non-radiative process with electron exchange. Although similar to Förster energy transfer, if differs greatly in length scale and the underlying mechanism. Dexter transfer can be singlet-singlet or triplet-triplet, and the three fundamental excitations in lead PQDs are triplets [132]. Dexter energy transfer is a process where the donor and the acceptor exchange their electron. Thus, the exchanged electrons should occupy the orbital of the other pair. The Dexter transfer rate has the form $V_D \propto J\exp(-2r_{12}/L_v)$, where J is the normalized spectral overlap, and L_v is the the sum of van der Waals radius. Dexter transitions couple bright excitons to bright excitons and are spin preserving. Their strength can also be computed from the Coulomb matrix element. However, since Dexter coupling requires overlap with the electronic wave functions, we believe it is highly unlikely for our coupled QDs.

There are also potential monopole-monopole interactions, which do not depend on any spatial overlap of the electronic wave functions. These are usually neglected in the derivation of Förster coupling between quantum emitters. Actually, monopole-monopole is also the origin of Dexter energy transfer, but in that case, the contribution also requires oribital overlap. In the linear excitation domain (e.g., neglecting biexciton effects), the excitonic monopole-monopole term [140, 141] merely renormalizes the eigenergies, unlike Förster and Dexter terms which represent exchange

of photons or electronic excitations. Furthermore, for a symmetric wavefunctions, monopole-monopole shifts should be zero for linear excitation.

There could also be effects beyond a dipole approximation, which can be captures by doing a spatial integration with respect to the inter-PQD exciton wave functions and the photon Green function propagator [142]. We have carried out such a calculation using 6D Monte Carlo integration and found the dipole approximation to be excellent, within 5% for QD cubes that have a gap separation of 1 nm. This calculation used the ground state exciton wave function, and we used a similar integration techniques to compute C, which enhances the oscillator strength.

Finally, we mention tandem tunneling [143] that can occur through the intermediate state in which the electron and hole are in different PQDs. This process has been shown to have exciton hopping rates that are larger than the Dexter rate Förster for certain PQDs. However, such PQDs are clearly fused together (unlike our optically trapped coupled PQDs), so we also rule out the effect of fused tunneling.

Additional calculations for vertically and horizontally coupled QD cubes on gold film are shown in the main text.

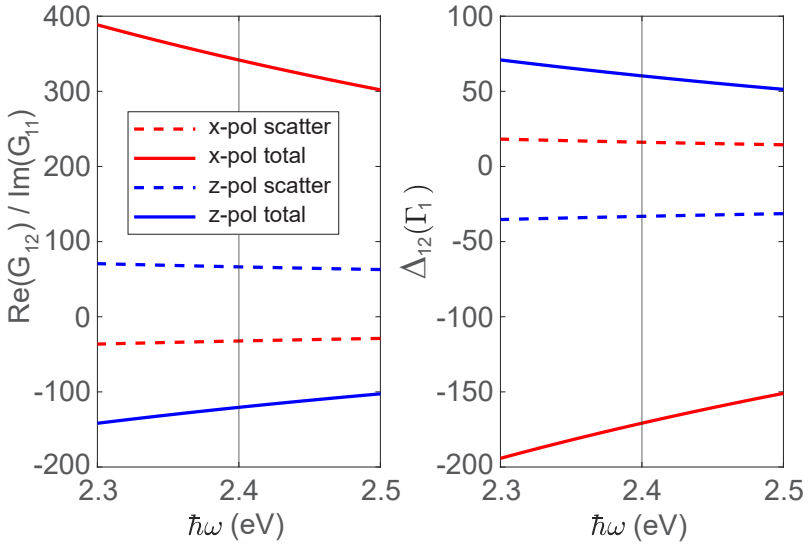

Fig. B2: Green function calculation of the propagators (in Purcell factor units), and corresponding frequency shifts from dipole-dipole coupling. We use two dipoles, 6 nm above a metal film, separated in x by 11 nm (Fig. B1 right side). Note the scattered components from the metal film contribute negatively, and thus reduce the usual Förster coupling. The thin vertical line corresponds to a frequency close to our experiments.

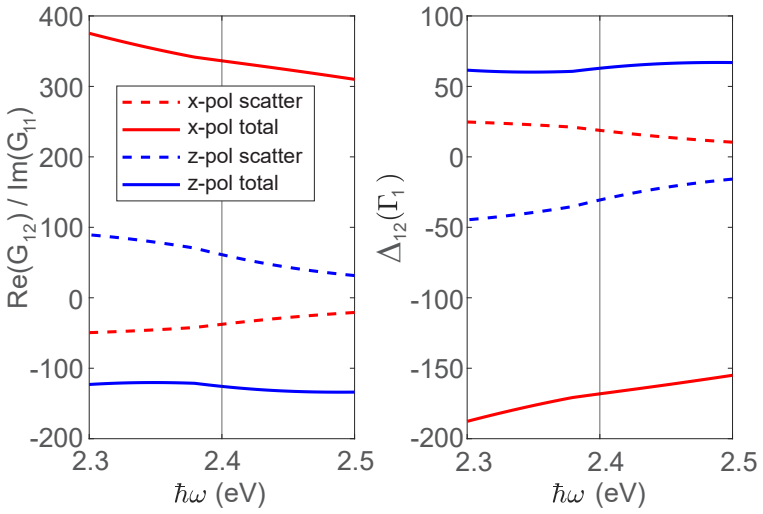

Fig. B3: Same as in Fig. B2, but using Johnson and Christy data for gold [157]. As can be seen, there are little qualitative differences in the frequency of interest.

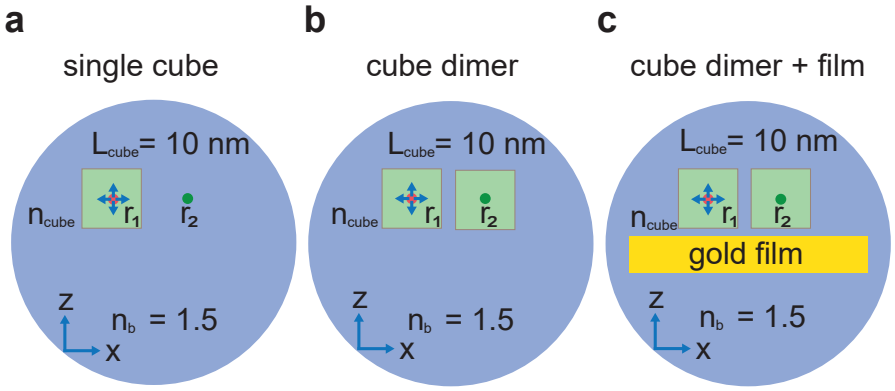

Fig. B4: Schematic diagram for single cube, cube dimer (side by side, here the surface to surface gap is 1 nm) and cube dimer plus the gold film (cube dimer is placed 1 nm above the gold film), used in the numerical COMSOL simulations. The source dipole is placed in the center $\mathbf{r}_1$ of the left cube, where we consider x- or z-polarized.

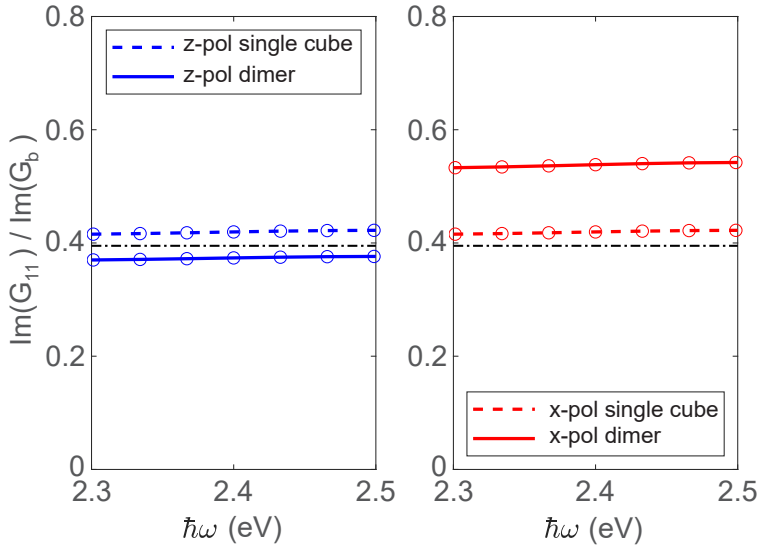

Fig. B5: Projected LDOS in Purcell factor units, showing the effect of local field corrections with a single cube and a cube dimer (Fig. B4 (a,b)). The expected analytical answer is also shown for a single cube (Eq. (B.16), thin chain line). Note the lines and symbols are the same data, but more accurately show the numerically computed data points (symbols).

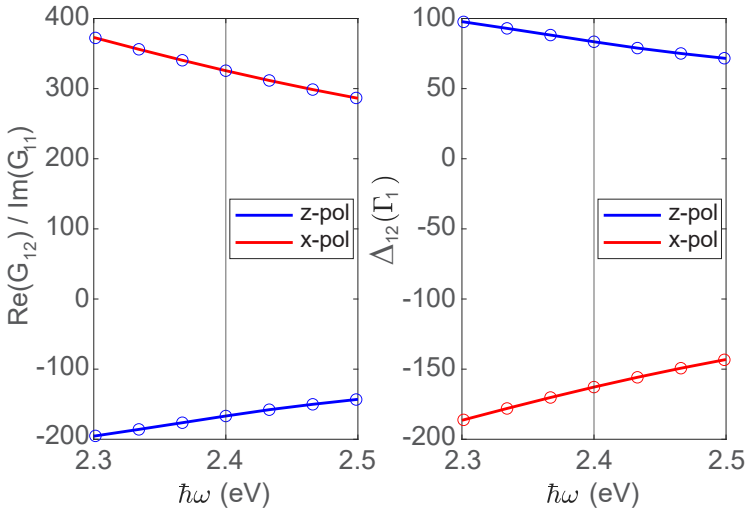

Fig. B6: Propagators and dipole-dipole shifts computed from COMSOL, which includes the full scattering geometry (Fig. B4 (c)). All terms include local field corrections, so are normalized by the result including the single QD cube. The decay rate, Γ_1, is thus the one also including local field corrections for a single QD cube. The vertical line is close to the experimental frequency regime.

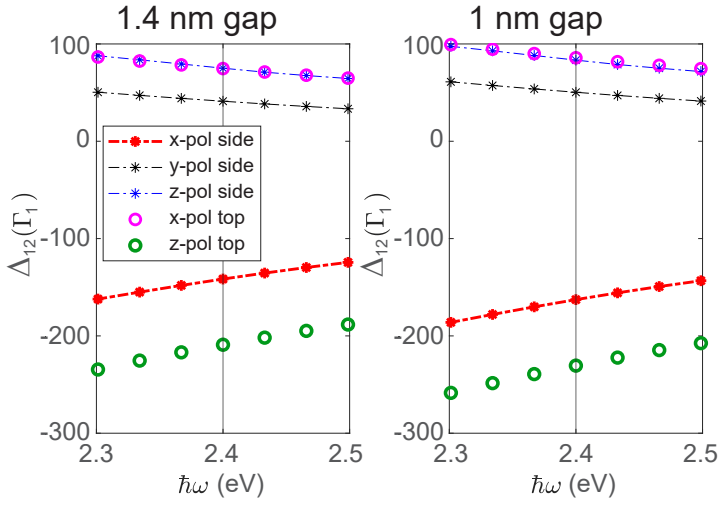

Fig. B7: Dipole-dipole frequency shifts computed in COMSOL, showing the difference between 1 nm (right side, same as Fig.3 c right figure in main text) and 1.4 nm gaps (left side). The larger gap causes a very small reduction, as expected. With 1.4 nm gap, the maximum photon exchange rate is around $-209\hbar\Gamma_1$ for z-polarized dipoles with top coupling, which we estimate to be around -0.56 meV.

Appendix C

Data Analysis

Spectrum data were saved in .csv file, which consists of two columns: wavelength and counts. Trapping data were saved in .txt file, which can be read by MATLAB 2016. MATLAB 2016 and Origin 2021 were used to read and process data and perform analysis.
All the matlab code is available at *github.com/layallan/MATLAB_MASTER.*